Light passing through subwavelength apertures

F.J. Garcia-Vidal,[1] L. Martin-Moreno,[2] T.W. Ebbesen,[3] and L. Kuipers[4]
[1]*Departamento de Física Teórica de la Materia Condensada, Universidad Autónoma de Madrid, E-28049 Madrid, Spain*
[2]*Departamento de Física de la Materia Condensada-ICMA, Universidad de Zaragoza-CSIC, E-50009 Zaragoza, Spain*
[3]*ISIS, Université Louis Pasteur, 8 allée G. Monge, 67000 Strasbourg, France*
[4]*FOM Institute for Atomic and Molecular Physics, Kruislaan 407, 1098 SJ Amsterdam, The Netherlands*

This review provides a perspective on the recent developments on the transmission of light through subwavelength apertures in metal films. The main focus is on the phenomenon of extraordinary optical transmission in periodic hole arrays, discovered ten years ago. It is shown that surface electromagnetic modes play a key role in the emergence of the resonant transmission. These modes are also shown to be at the root of both the enhanced transmission and beaming of light found in single apertures surrounded by periodic corrugations. Additionally, the cases of slit arrays and single apertures are addressed. This review covers both the theoretical and the experimental aspects of the subject. Furthermore, the physical mechanisms operating in the different structures considered are analyzed with a common theoretical framework. Several applications based on the transmission properties of subwavelength apertures are also described.

PACS numbers: 42.79.Gn, 73.20.Mf, 42.25.Bs

Contents

I. INTRODUCTION

A. Historical background

The optical properties of subwavelength apertures in metallic films have been the focus of much research activity around the world since the extraordinary optical transmission (EOT) phenomenon was reported ten years ago (Ebbesen *et al.*, 1998). This phenomenon was discovered serendipitously for arrays of subwavelength apertures in metal films and later extended to single apertures surrounded by periodic corrugations. The initial surprise and interest was generated by the fact that light of wavelength much larger than twice the diameter of the holes were being transmitted with greater than unit efficiency (normalized the area of the hole) while under such conditions light cannot freely propagate through the aperture. Bethe had already shown in the 1940s (Bethe, 1944) that the optical transmission through subwavelength holes should be orders of magnitude smaller even for an infinitely shallow hole. When considering the real depth of the holes, this transmittance is further reduced (Roberts, 1987). Indeed, the holes were milled in optically thick metal films and the electromagnetic (EM) waves could only tunnel through the holes in the transmission process. As tunnelling processes are highly inefficient and exponentially sensitive to the depth of the holes (Degiron *et al.*, 2002; Martin-Moreno *et al.*, 2001), something had to be boosting the transmission over the earlier theoretical predictions. This, it turned out, was the role of the surface plasmon polaritons (SPPs) generated at the metal surface of these periodic structures which provide tremendous field intensities at the apertures. Other resonant modes (e.g. Fabry-Perot modes, localized surface plasmons) can also be involved in the transmission process depending on the size and shape of

the individual apertures. Even isolated subwavelength apertures in optically thick films have a resonance mode just below cutoff which boosts the transmission at the corresponding wavelength.

Periodic arrays start resembling, as the holes become larger and propagative, and the metal becomes very thin relative to the wavelength (e.g. $< 1/10$), metallic mesh filters, which are characterized by a very broad peak at normal incidence near the periodicity. One-dimensional (1D) mesh filters were already in use in the 19th century for microwaves, most notably by J.C. Bose in Calcutta (Emerson, 1997). In the 1950 and 1960s, two-dimensional (2D) metallic grids were studied extensively to obtain bandpass filters in the far infra-red (Renk and Gensel, 1962; Ulrich, 1967). They were treated either as transmission line equivalent circuits (e.g., inductive grids) or analyzed as diffraction gratings (Chen, 1971; Eggiman and Collin, 1962). Transmission properties of the mesh filters were eventually analyzed (Ulrich, 1974) by considering the surface waves at the metal interface, the so-called Zenneck waves (Zenneck, 1907), in line with metal grating theory (Hessel and Oliner, 1965). Transmission resonances for metal gratings and coupled surfaces can be observed even in the absence of holes if the metal film is sufficiently thin and translucent (on the order of the skin depth) (Dragila *et al.*, 1985; Gruhlke *et al.*, 1986).

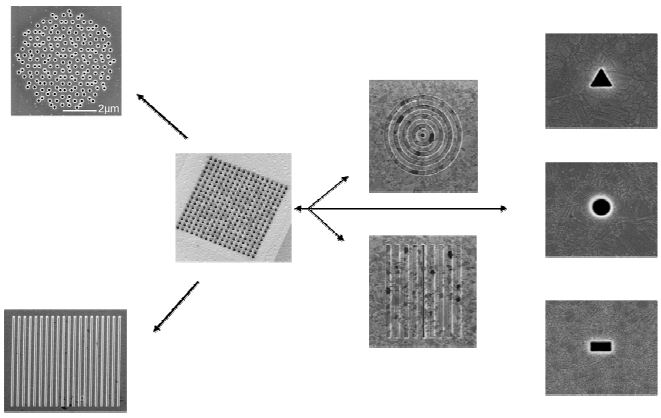

FIG. 1 Various types of aperture structures that are considered in this review paper.

The interest in EOT stems in great part because of the opposite feature: the structures provide high contrast between the opaque metal and the bright subwavelength aperture, be there one or many. This gives rise to relatively narrow transmission peaks. Furthermore, the metal can be sculpted not only on the incident surface to control the coupling of the incident light and its scattering dynamics at the surface but also on the exit surface to modify, for instance, the re-radiation and propagation of light into free space or the launching of SPPs.

Here we review the extensive work on subwavelength aperture optics that the EOT process has stimulated considering both the fundamental aspects as well as applications. On the fundamental side, we review the present understanding of the optical properties of individual apertures (section II), arrays of subwavelength apertures (section III) and apertures surrounded by corrugations (section IV). We compare theoretical analysis and the experimental results, showing that the transmission phenomenon can be quite intricate and involve multiple processes. In section V, we discuss several EOT applications that have been investigated, in particular in the area of spectroscopy and molecular probes as well as stand alone photonic devices. Finally, we consider the extension of these ideas to other types of waves and speculate about the future trends in section VI.

B. Theoretical modelling

Although the equations that govern electromagnetic phenomena in metallo-dielectric structures are well established (Maxwell equations plus the constitutive relations describing material properties), solving them is a very difficult task due to the highly different length scales present in metals. In the optical regime, an important role is simultaneously played by the free-space wavelength, λ ($400-800$nm), the skin depth of the metal (of the order of 30nm), the dimensions of the scatterers placed on the metal (tens to hundreds of nm) and the device dimensions (several microns).

Several methods have been used to compute the transmission of EM fields through apertures, each one presenting their own advantages and disadvantages. In general, no computational tool is best in all circumstances. In what follows we briefly summarize the theoretical approaches that have been used to study of transmission through subwavelength apertures. Later on, we present an approximate method that will be applied throughout this review in order to give a unified view of the operating physical mechanisms in the different structures.

The theoretical study of single apertures in a real metal can be treated by a variety of methods, such as (i) the Multiple Multipole Method (MMP) (Wannemacher, 2001), the (ii) Green's Dyadic Method (GDM) (Colas des Francs *et al.*, 2005; Sepúlveda *et al.*, 2008) and (iii) Finite Difference Time Domain (FDTD) method (Chang *et al.*, 2005; Popov *et al.*, 2005). The first two cases are very computationally demanding (MMP due to the large number of multipoles needed in order to achieve convergence and GDM due to the difficulty in evaluating the Sommerfeld integrals involved). FDTD is faster, but its applicability is sometimes limited by the small grid sizes needed to reproduce the rapid variations of the EM fields at the metal-dielectric interfaces. Additionally, some technical problems due to the finite simulation window must be overcome (for instance, the implementation of plane wave illumination in finite systems is not trivial).

The theoretical analysis of the optical response of arrays of apertures is greatly simplified if the arrays are considered infinite and periodic. Then, with the help of Bloch's theorem, only EM fields within one unit cell need

be computed. This allows for a very accurate calculation of the transmission properties of arrays of apertures using different numerical techniques as: (i) the Rigorous Coupled Wave Method (RCWM) (Li, 1997), based on the modal expansion of the fields, in which the eigenmodes in the perforated metal film are computed after expansion of the dielectric constant in harmonics (Lalanne *et al.*, 2005b; Popov *et al.*, 2000). Actually, a modification of this general method has been recently used to study also single apertures (Lalanne *et al.*, 2005a) (ii) a differential method (Salomon *et al.*, 2001), borrowed from the traditional method for analyzing metallic gratings, has been used to study extremely thin films (metal thickness of the order of 20nm) (iii) Transfer Matrix Method (Bell *et al.*, 1995; Pendry and MacKinnon, 1992), in which the EM fields are discretized in space at a given frequency. This method is very computationally demanding and has only been applied in 1D systems (Porto *et al.*, 1999) and (iv) FDTD method (Baida and Van Labeke, 2003; Chen *et al.*, 2008; Miyamaru and Hangyo, 2005; Müller *et al.*, 2004; Rodrigo *et al.*, 2008). A number of approximate techniques have also been used. One of them is based on the RCWM, but considers only a few harmonics in the expansion for the dielectric constant of the metal (Darmanyan *et al.*, 2004; Dykhne *et al.*, 2003; Kats *et al.*, 2005; Kats and Nikitin, 2004). The advantages of this method is that it can be worked out analytically and that it can treat resonant optical transmission through corrugated *continuous* metal films (Chen *et al.*, 2008; Gruhlke *et al.*, 1986); its disadvantage is that the accurate treatment of holes in a metal film requires a very large number of harmonics.

The computation of properties of arrays of apertures beyond these two limiting cases (isolated apertures and infinite periodic arrays) is much more difficult and the calculation must, in general, be done with approximate methods. Collin and Eggimann (1961) developed a formalism, based on the coupling of the electric and magnetic dipoles that represent the hole in this limit (Bethe, 1944), valid for extremely small circular holes ($\lambda >> 2\pi r$, where r is the radius of the hole). In its original formulation, the method could only treat holes in an impenetrable screen of zero thickness. Recently, the extension to metal films of finite thickness has been presented (De Abajo, 2007; De Abajo *et al.*, 2005). Another method, which can be considered as a extension of the RCWM, considers the hole as a finite portion of a finite waveguide; correspondingly, the EM fields inside the perforated metal are expanded in terms of waveguide modes. This approach is not restricted neither to small holes nor perfect conductors, and is valid when all distances between apertures and the thickness of the metal film are a few times the skin depth of the metal (i.e., when the apertures can not interact across the bulk of the metal).

The theoretical formalism used throughout this review is included into this last category. We present here the basic ingredients and, in order to improve the readability, we leave the detailed derivation for Appendix A. An important asset of this formalism is that the same equations can deal with the physics of very different structures. In a first approximation, the metal is treated as a perfect electrical conductor (PEC), i.e. $\epsilon = -\infty$. The main advantage of this approximation is that the EM modes inside the apertures (slits or holes) coincide with the waveguide modes of the apertures, which are analytically known for some geometries. This PEC model is quasi-exact for metals in the terahertz or microwave ranges of the EM spectrum. Moreover, the finite dielectric constant of metals at optical frequencies can be approximately incorporated into the formalism by using the surface impedance boundary conditions (SIBC) (Landau *et al.*, 1960). Within this approach, the theoretical modelling based on the modal expansion also has semiquantitative value in the optical regime, for good conductors like silver or gold.

Figure 2 renders a schematic picture of a general system under study. A set of apertures or indentations placed on a metallic film of thickness h. In this section we present the general formalism for the 2D geometry comprising a set of holes and/or dimples. The implementation for the 1D case (slits and/or grooves) is straightforward. Depending on each case, this set can be formed by just one isolated aperture (as in section II), an infinite periodic array (section III) or a single aperture flanked by a finite array of indentations (section IV). The system can be divided in three regions. Regions I (reflection) and III (transmission) are dielectric semi-spaces characterized by positive dielectric constants, ϵ_1 and ϵ_3, respectively. Region II represents the perforated metal film with a frequency-dependent dielectric function ϵ_M. We assume that the structure is illuminated by EM plane waves coming from region I.

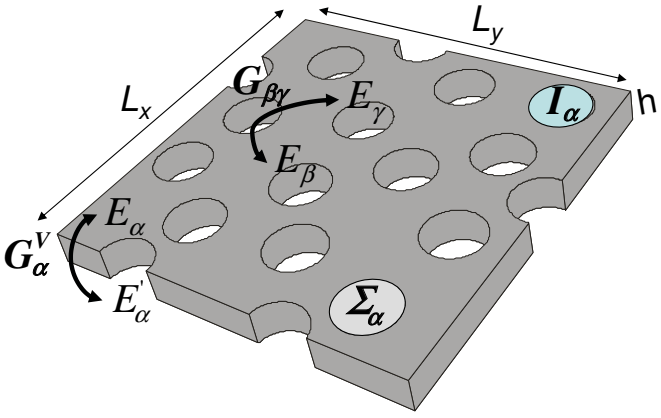

FIG. 2 Schematic representation of a unit cell of lengths L_x and L_y containing a finite set of indentations perforated on a metallic film of thickness h. The different terms appearing in the set of equations (1) are also schematically depicted.

We expand the EM fields on the eigenmodes of each region (EM plane waves in regions I and III and waveguide modes inside the apertures), and match the parallel components of the electric and magnetic fields at the two

interfaces ($z = 0$ and $z = h$). After some algebraic manipulations, we end up with a coupled system of equations for E_α and E'_α, which essentially are the modal amplitudes of the electric field at the input and output sides of the apertures, respectively (α is an index that labels all waveguide modes in all apertures considered in the calculation). The set that $\{E_\alpha, E'_\alpha\}$ must satisfy is:

$$\begin{aligned}(G_{\alpha\alpha} - \Sigma_\alpha)E_\alpha + \sum_{\beta\neq\alpha} G_{\alpha\beta}E_\beta - G^V_\alpha E'_\alpha &= I_\alpha \\ (G'_{\gamma\gamma} - \Sigma_\gamma)E'_\gamma + \sum_{\nu\neq\gamma} G'_{\gamma\nu}E'_\nu - G^V_\gamma E_\gamma &= 0 \end{aligned} \quad (1)$$

This is the basic set of linear equations that will be used throughout this review to describe the transmission properties of different structures containing subwavelength apertures. Details of the derivation, as well as the mathematical expressions for the different magnitudes can be found in Appendix A. In this section we simply give their physical meaning. The independent term, I_α, takes into account the direct initial illumination over object α. Σ_α is related to the bouncing back and forth of the EM-fields inside object α whereas G^V_α accounts for the coupling between the EM fields at the two sides of the aperture. The term $G_{\alpha\beta}$ controls the EM-coupling between objects α and β in region I. This "propagator" takes into account that each point in object β emits EM radiation, which can be "collected" by object α. The propagator $G'_{\gamma\nu}$ differs from $G_{\alpha\beta}$ only in the constituents, i.e., $G'_{\gamma\nu}$ is a function of ϵ_3 whereas $G_{\alpha\beta}$ depends on ϵ_1. Formally the propagator $G_{\alpha\beta}$ can be written as:

$$G_{\alpha\beta} = i\sum_{\vec{k}\sigma} Y_{\vec{k}\sigma} < \alpha|\vec{k}\sigma >< \vec{k}\sigma|\beta > \quad (2)$$

with a similar expression for $G'_{\alpha\beta}$. In Eq.(2), $Y_{\vec{k}\sigma}$ is the admittance of the plane wave: $Y_{\vec{k}s} = k_z/k_\omega$ and $Y_{\vec{k}p} = \epsilon_1 k_\omega/k_z$, for s- and p- polarization, respectively, being $k_\omega = \omega/c = 2\pi/\lambda$ (ω the frequency and c the speed of light) and $|k|^2 + k_z^2 = k_\omega^2$.

As stated above, the finite conductivity of the metal can be incorporated into this modal expansion framework by introducing SIBC instead of perfect metal boundary conditions. Within this approximation, the set of Eqs.(1) is still valid but with magnitudes that now depend on the surface impedance of the metal, $Z_S = 1/\sqrt{\epsilon_M(\omega)}$, where $\epsilon_M(\omega)$ is the frequency-dependent dielectric function of the metal. Expressions for I_α, G^V_α, Σ_α and $G_{\alpha\beta}$ within the SIBC approach can also be found in Appendix A.

Once the self-consistent $\{E_\alpha, E'_\alpha\}$ are found after solving Eqs.(1), the EM fields in all regions can be then calculated, and from them the total transmittance. Therefore, the modal expansion method reduces the calculation of the EM fields everywhere into finding the EM field distribution just at the aperture openings, which is extremely efficient when the openings cover a small fraction of the metal surface. Convergence (as a function of number of waveguide modes needed) is reached very quickly, specially in the subwavelength regime. In fact, in this regime, a very accurate result for the transmittance can be achieved by considering only the fundamental waveguide mode inside each aperture. For the case of a single aperture or an infinite periodic array, this single mode approximation ($\alpha = 0$) allows a quasi-analytical treatment of the set of equations (1) that now transforms into a set of just two linear equations:

$$(G - \Sigma)E - G^V E' = I, \quad (G' - \Sigma)E' - G^V E = 0 \quad (3)$$

where $G \equiv G_{00}$, $G' \equiv G'_{00}$, $\Sigma \equiv \Sigma_0$, $G^V \equiv G^V_0$ and $I \equiv I_0$. The solution of this set of equations is:

$$\begin{aligned} E &= \frac{(G' - \Sigma)I}{(G - \Sigma)(G' - \Sigma) - (G^V)^2} \\ E' &= \frac{G^V I}{(G - \Sigma)(G' - \Sigma) - (G^V)^2} \end{aligned} \quad (4)$$

When surface EM modes are present in the structure, it is useful to consider a multiple scattering technique. Within this framework, the scattering coefficients of a stratified media can be obtained in terms of the scattering coefficients related to isolated interfaces. In all cases analyzed in this review, the structures are formed by three layers (reflection and transmission regions plus the perforated metal). Therefore, three different scattering problems involving two semi-infinite media must be solved (see Figure 3).

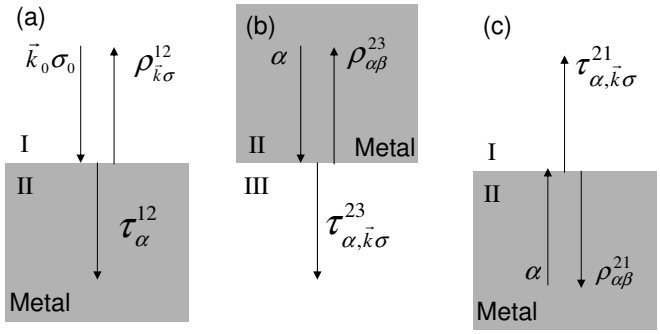

FIG. 3 Schematic definition of the different scattering coefficients for the EM fields at isolated interfaces dividing two semi-infinite media. (a) A plane wave impinging from medium I into medium II. (b) Incidence from a waveguide mode α in medium II into medium III. (c) As in (b) but now the waveguide mode α is back-scattered in medium II or transmitted to medium I.

In Figure 3(a), the incident plane wave coming from reflection region (medium I), characterized by $\vec{k}_0\sigma_0$ and unit amplitude, impinges at medium II (perforated metal). The incoming field is reflected back into the different diffraction modes in medium I with amplitude $\rho^{12}_{\vec{k}\sigma}$

and transmitted into object α of medium II with amplitude τ_α^{12}. The second two-media scattering problem is schematically depicted in Figure 3(b): a waveguide mode α coming from medium II impinges at the interface with medium III. It is reflected back at the interface into waveguide mode β with amplitude $\rho_{\alpha\beta}^{23}$ and transmitted into the different plane waves of medium III, $\vec{k}\sigma$, with amplitude $\tau_{\alpha,\vec{k}\sigma}^{23}$. The third scattering process is similar to the previous one changing medium III by medium I (see panel (c) of Fig. 3). Detailed expressions for the two-media scattering coefficients can be also found in Appendix A.

The total transmission process can be seen as an infinite sum of scattering processes involving the two interfaces plus light propagation inside medium II. The infinite series is geometric and can be summed up yielding for transmission coefficient, $t_{\vec{k}\sigma}$:

$$t_{\vec{k}\sigma} = \sum_{\alpha,\beta,\gamma} \tau_\alpha^{12} e_\alpha [\delta_{\alpha\beta} - \rho_{\alpha\gamma}^{21} e_\gamma \rho_{\gamma\beta}^{23} e_\beta]^{-1} \tau_{\beta,\vec{k}\sigma}^{23} \qquad (5)$$

where $e_\alpha \equiv \exp(iq_{z\alpha}h)$, $q_{z\alpha}$ being the propagation constant associated with mode α.

II. TRANSMISSION THROUGH SINGLE APERTURES

A. 1D aperture: single slit

We start our study of the transmission properties of subwavelength apertures by analyzing the simplest case: a single 1D slit perforated on a metal film of thickness h illuminated by a plane wave (see Fig. 4). We assume that the incident wavector has a null component in the y-direction. The width of the slit is a and the film thickness is h. Since this structure presents translational symmetry along the direction parallel to the slit, the analysis can be restricted to the perpendicular plane where both light polarizations (s and p) are decoupled. For p-polarized light, the magnetic field is parallel to the slit (y-direction) and the electric field has non-zero x and z components. For s-polarized light, the E-field is pointing to the y-direction and H-field lies in the $x-z$ plane.

The transmission properties of a single slit perforated on a thick metal film was theoretically study within the electrical engineering community during the 70's and 80's of the last century (Auckland and Harrington, 1978; Harrington and Auckland, 1980; Hongo, 1971; Kashyap and Hamid, 1971; Lehman, 1970; Neerhoff and Mur, 1973). These authors predicted the appearance of transmission resonances for incident p-polarized radiation, by using different theoretical approaches (Fourier transforms, matrix techniques or the method of moments). The interest on this type of 1D structures was renewed after theoretical studies found that EOT phenomenon also emerges in 1D periodic arrays of slits (Porto *et al.*, 1999; Schroter and Heitmann, 1998). Takakura (2001) revisited the existence of transmission resonances in single, isolated slits

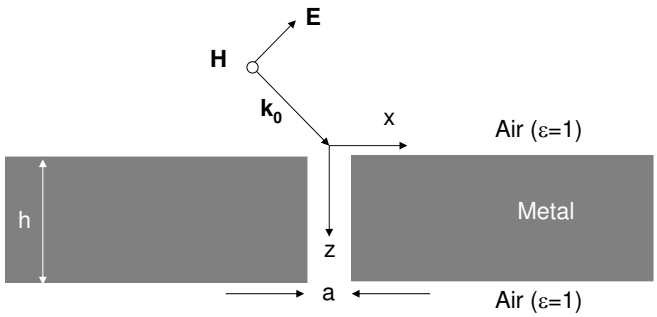

FIG. 4 Schematic picture of a single slit of width a perforated on a metal film of thickness h illuminated by a p-polarized radiation. For the case of s-polarized incident radiation, vectors **E** and **H** are interchanged.

for p-polarized illumination, finding analytical expressions for the total transmittance. One year later, Yang and Sambles (2002) verified experimentally the existence of transmission resonances in the microwave regime.

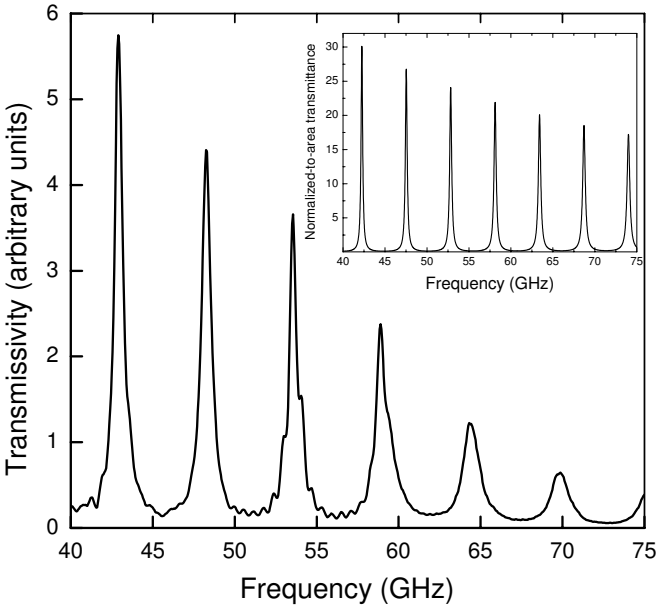

FIG. 5 Transmission (in arbitrary units) as a function of frequency (in GHz) for a single slit of width 75μm perforated on a metal film of thickness 28.2mm, as reported by Yang and Sambles (2002). Inset: calculated normalized-to-area transmittance for p-polarized light through a single slit with the same geometrical parameters of the main panel.

In what follows we present the theoretical foundation of these transmission resonances by using the general formalism described in section I.B. We first analyze the case of p-polarized light. In this case, the objects α in Eqs.(1) are the TM waveguide modes inside the slit (the TE modes can be neglected because they do not couple to the incident p-polarized radiation). Note also that now the only non-zero component of the E-field bivector is the x-component. The mathematical expression for E_x associated with mode α is:

$$< x|\alpha >= \sqrt{\frac{C_\alpha}{a}} \cos[\frac{\alpha\pi}{a}(x+a/2)]\theta(a/2-|x|) \qquad (6)$$

where α is an integer ≥ 0 and the normalization constant, C_α, is 1 for $\alpha = 0$ and $C_\alpha = 2$ otherwise. The propagation constant associated with mode α is $q_{z\alpha} = \sqrt{k_\omega^2 - \pi^2\alpha^2/a^2}$. Strictly speaking, mode $\alpha = 0$ is a TEM mode (both the electric and magnetic fields are transversal) that does not present cutoff.

As we are dealing with a non-periodic structure, the coupling term between TM waveguide modes in Eqs.(1), $G_{\alpha\beta}$, has to be evaluated as an integral over vacuum plane waves, $G_{\alpha\beta} =< \alpha|\hat{G}|\beta >$, where the operator $\hat{G}$ in real space is the one described in Appendix A [see Equation (A18)]. For instance,

$$G_{00} = \frac{i\pi}{a\lambda} \int_{-a/2}^{a/2} dx \int_{-a/2}^{a/2} dx' H_0^{(1)}(k_\omega(x-x')) \qquad (7)$$

where $H_0^{(1)}$ is the zero-order Hankel function of the first kind.

In the inset of Figure 5 we render the normalized-to-area transmittance (transmittance normalized to the amount of light that is impinging directly at the slit opening) versus wavelength for a single slit of width $a = 75\mu$m, perforated onto a metallic film of thickness $h = 28.2mm$, as obtained by Bravo-Abad *et al.* (2004b). As in the experiment, a series of transmission peaks dominate the spectrum and the peak height decreases as the resonant frequency is increased. In order to gain physical insight, we consider the extreme subwavelength regime, $a << \lambda$, in which a very good approximation to the final transmittance spectrum can be achieved by considering only the TEM waveguide mode ($\alpha = 0$) inside the slit. Within this approximation, we must solve Eqs.(3) where, for this particular case: $G = G' = G_{00}$, $\Sigma = \cot(k_\omega h)$, $G^V = 1/\sin(k_\omega h)$, and $I = 2i$ for a normal incident plane wave whose energy flux integrated over the slit opening is 1. In this way, $T = \mathrm{Re}[G^V E^* E']$, directly gives the normalized-to-area transmittance.

The spectral locations of the transmission peaks are associated with the resonant condition of the denominator for E and E' in Eqs.(4), $|G-\Sigma| = |G^V|$. After some straightforward algebra, this condition can be re-written as:

$$\tan k_\omega h = \frac{2ReG}{|G|^2 - 1}. \qquad (8)$$

In the limit of extremely narrow slits ($G \to 0$), this last equation predicts the appearance of transmission peaks close to the Fabry-Perot condition, $\sin k_\omega h = 0$. This shows that cavity resonances inside the single slit are responsible for the emergence of transmission peaks for p-polarized light. The analytical expression for the normalized-to-area transmittance at resonance, T_{res}, can be obtained using the resonant condition, $|G-\Sigma| = |G^V|$, in the equation for T. We obtain $T_{res} = |I|^2/[4Im(G)]$. A very accurate estimation for T_{res} can then be obtained by taking the limit $a << \lambda$ in the expressions for $Im(G)$ as given in Eq.(7), leading to $T_{res}^{slit} = \frac{\lambda}{\pi a}$. This analytical result predicts a linear increase of T_{res} with the resonant wavelength, as observed in Figure 5. This analytical expression for T_{res} was firstly derived by Harrington and Auckland (1980) by using a circuit model and is strictly valid within the PEC approximation. However, Suckling *et al.* (2004) demonstrated that, even at microwave frequencies, the transmission enhancement is limited by the finite conductivity of the metal. In an ideal PEC, the modal size of the fundamental mode inside the slit is always equal to the slit's width, which can be made arbitrarily small. But, in a real metal, the modal size is limited to roughly two times the skin depth of the metal, thus limiting the total transmittance through the slit.

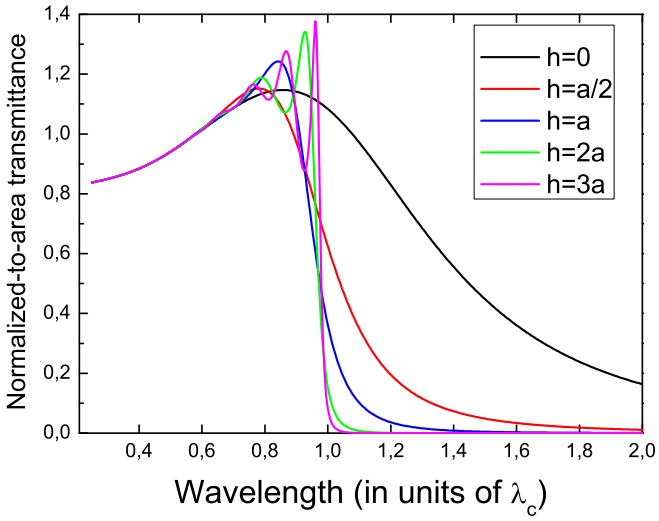

FIG. 6 Normalized-to-area transmittance versus wavelength (in units of the cutoff wavelength of the fundamental TE mode, $\lambda_C = 2a$) through a single slit of width a perforated on a PEC film of different thicknesses, h, ranging from $h = 0$ to $h = 3a$. The normal incident plane wave is s-polarized.

A similar theoretical analysis can be done when the single slit is illuminated by s-polarized light. Now, only the TE modes inside the slit need to be considered. The mathematical expression for the y-component of the E-field associated with mode α is:

$$< x|\alpha >= \sqrt{\frac{2}{a}} \sin[\frac{\alpha\pi}{a}(x+a/2)]\theta(a/2-|x|) \qquad (9)$$

with $\alpha \geq 1$. The propagation constant of mode α is $q_{z\alpha} = \sqrt{k_\omega^2 - \pi^2\alpha^2/a^2}$. Therefore, conversely to TM modes, these TE waveguide modes present cutoff. The electromagnetic coupling between TE modes is governed by $G_{\alpha\beta}$ terms that, due to the different boundary conditions, are different to those of the p-polarized case.

The expression in real space of the s-polarization Green's function is:

$$< x|\hat{G}|x' >= G(x,x') = \frac{i}{2\pi}\int_{-\infty}^{\infty} dk \frac{\sqrt{k_\omega^2 - k^2}}{k_\omega} e^{ik(x-x')} \quad (10)$$

In Figure 6 we render the normalized-to-area transmittance spectra for slits with the same width a but different thicknesses, ranging from $h = 0$ to $h = 3a$. Note that, in contrast to the p-polarized case, the transmission process is dominated by the existence of a cutoff wavelength for TE modes, $\lambda_C = 2a$. For $\lambda > \lambda_C$ and thick enough films, the transmission is strongly attenuated due to evanescent character of the EM fields inside the slit. Fabry-Perot resonances similar to those found for p-polarized light appear in the spectrum for $\lambda < \lambda_C$.

B. 2D single apertures

1. Circular holes

Although the curiosity and technological interest on the phenomenon of transmission of light through small holes in a opaque screen started centuries ago, the first accurate treatment of the electromagnetic coupling through small holes was presented by Bethe (1944) in the idealized case of a zero-thickness perfect conductor film. In his calculation, the screen and the aperture were replaced by two emitting electric and magnetic dipoles. Bethe derived a very simple expression for the normalized-to-area transmittance in the extreme subwavelength limit ($k_\omega r \ll 1$):

$$T_{Be} = \frac{64(k_\omega r)^4}{27\pi^2} \quad (11)$$

where r is the radius of the hole. This equation implies that T_B scales as $(r/\lambda)^4$ and a rapid drop of the optical transmission as λ is increased is expected. Six years later, Bouwkamp (1950) found that the transmittance could be written as a series in $k_\omega r$, in which the expression obtained by Bethe was just the first term. Bouwkamp derived the following expression for the normalized-to-area transmittance, T_{Bo}:

$$T_{Bo} = T_{Be}\{1+\frac{22}{25}(k_\omega r)^2+\frac{7312}{18375}(k_\omega r)^4+O(k_\omega r)^6\} \quad (12)$$

Notice that this series seems to diverge if $\lambda \leq 2\pi r$. Therefore, the expressions given by Bethe and Bouwkamp have limited value for the EOT phenomenon, in which the resonant wavelength is typically $2-3$ times the diameter of the holes. Furthermore, T_{Be} and T_{Bo} were obtained for a opaque screen with negligible thickness. The transmission efficiency is further exponentially attenuated for metallic films of finite thickness for wavelengths longer than the cutoff wavelength of the hole, $\lambda_C = 3.4r$. This hypothesis was quantitatively verified by Roberts (1987), who presented the first full calculation of the transmission properties of a single circular hole perforated on a PEC film of finite thickness. Figure 7 shows the normalized-to-area transmittance spectra obtained with the modal expansion formalism described in section I.B, which is equivalent to the one used by Roberts in her seminal paper. As seen in the figure, Bethe and Bouwkamp expressions [Eqs.(11) and (12)] are reasonable approximations in the extreme sub-wavelength limit ($k_\omega r << 1$) for $h = 0$ but overestimate the total transmission for $h \neq 0$ in all ranges of $k_\omega r$.

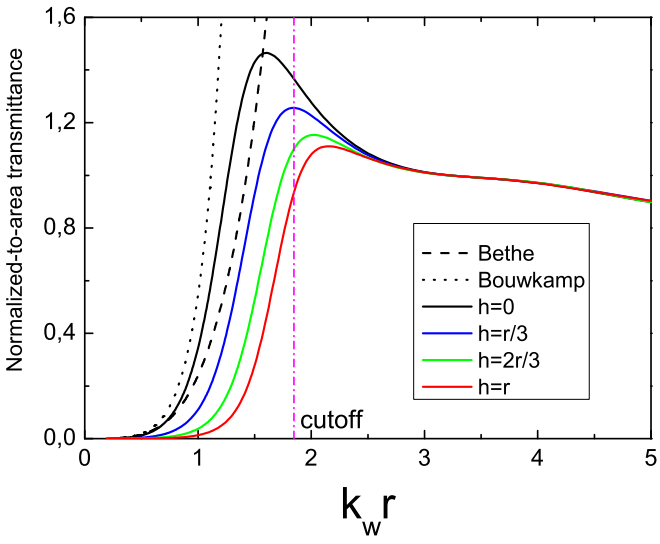

FIG. 7 Normalized-to-area transmittance for a normal incident plane wave versus $k_\omega r$ for a circular hole of radius r perforated on PEC films with several values of their thicknesses, h. Dashed and dotted lines show the predictions of Eq.(11) and Eq.(12), respectively. The cutoff wavelength of the hole waveguide, $k_\omega r = 1.85$ is also depicted in the figure.

The invention of the scanning near-field optical microscope (SNOM) in the eighties of last century (Lewis *et al.*, 1984; Pohl *et al.*, 1984) and the discovery of EOT phenomenon (Ebbesen *et al.*, 1998) stimulated new experimental and theoretical studies on both the total intensity and the spatial distribution of the light transmitted through a small circular hole. The first accurate numerical calculation of the transmittance through a circular hole perforated in a real metal at optical frequencies was reported by Wannemacher (2001). By using the MMP numerical method, this author was able to predict the appearance of transmission resonances in very thin silver films ($50-150$nm). Wannemacher (2001) ascribed this resonant enhancement of the transmission to a general SPP excitation.

The EM fields emerging from single circular subwavelength apertures have been experimentally mapped with single molecule detection (Betzig and Chichester, 1993; van Hulst *et al.*, 2000; Moerland *et al.*, 2004; Sick *et al.*, 2001; Veerman *et al.*, 1999). Through their dipole na-

ture, the single molecules act as subwavelength detectors of the vector EM fields behind the aperture, which is in this case the aperture of a near-field microscope probe. The molecular fluorescence of the molecule yields direct insight into the local EM fields: the fluorescence intensity I_{fl} of the molecule is related as $I_{fl} \propto \vec{\mu}.\vec{E}$, with $\vec{\mu}.\vec{E}$ the vector dot product of the local electrical field $\vec{E}$ and the transition dipole of the molecule $\vec{\mu}$. As a result, the fluorescence is not only a measure of the magnitude of the electric field, but it is sensitive to its direction with respect to the dipole (van Hulst *et al.*, 2000; Moerland *et al.*, 2004; Sick *et al.*, 2001; Veerman *et al.*, 1999). As a result, the full vectorial field emerging from the aperture can be accessed.

Regarding the issue on the spatial distribution of the light emerging from a single subwavelength circular hole, angular measurements at the exit of the holes (Degiron *et al.*, 2004; Obermuller and Karrai, 1995) have revealed that the angular distribution is far from being uniform, i.e., light diffracts less than expected for a subwavelength hole perforated in a PEC film. This non-uniform angular diffraction makes the measurement of the total transmittance through the single hole a delicate task. This type of measurements was presented by Degiron *et al.* (2004), for circular holes with radius $r = 135$nm milled in suspended silver films of various thicknesses, ranging from $h = 200$nm to $h = 800$nm. The total transmission spectra obtained are rendered in Figure 8, showing the presence of a transmission resonance, with an intensity that decreases rapidly with increasing h. Due to the finite dielectric function of silver at this wavelength range, the cutoff wavelength of the hole waveguide is larger than the PEC prediction, 460nm. Detailed calculations showed that in this case the cutoff wavelength is enlarged to 600nm (Moreno, 2008). Therefore, the observed transmission peak appears at a wavelength larger than the cutoff so the physical origin of this resonance can not be ascribed to the general kind of cutoff resonances that will be discussed later on when analyzing the transmission properties of rectangular holes. Based on measurements of the spatial and spectral characteristics of the light emission induced by a high energy electron beam, Degiron *et al.* (2004) concluded that this resonance stems from the excitation of a localized surface plasmon at the edges of the hole. In a different experimental study, Prikulis *et al.* (2004) showed that both scattering and extinction spectra of optically thin gold films perforated by subwavelength circular holes exhibit an optical resonance in the visible range. These authors also assigned the resonance to a dipolar localized surface plasmon at the hole circumference.

Subsequent theoretical investigations (Chang *et al.*, 2005; Popov *et al.*, 2005) corroborated the localized nature of those transmission resonances. In particular, Popov *et al.* (2005) concluded that there are two main contributions to the transmitted EM field: localized surface plasmon excitation produced by the ridges of the hole, which is almost normal to the E-field vector of the incident field, and a much weaker radiation from the electric dipole formed by the charge accumulated at the same points. FDTD calculations (Chang *et al.*, 2005) indicated that the spectral position of the transmission maximum red shifts with increasing hole diameter and blue shifts with increasing film thickness.

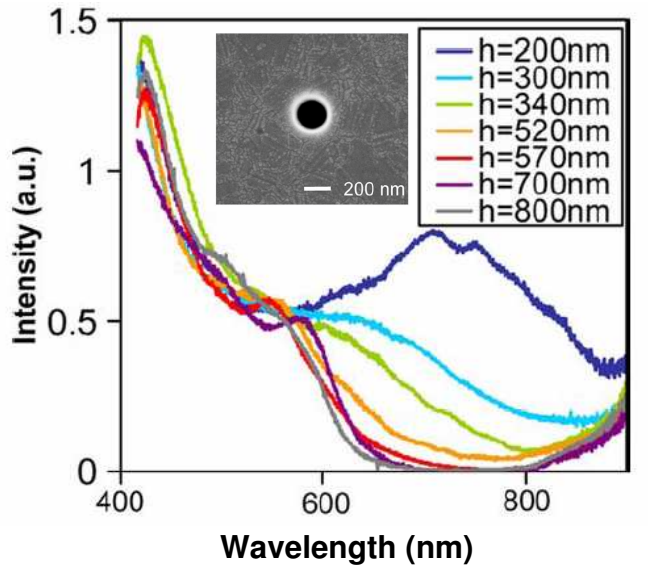

FIG. 8 Inset: SEM micrograph image of a single circular hole of radius $r = 135nm$ perforated on a suspended silver film. Main panel: transmittance spectra for normal incident radiation for a range of film thicknesses, h. Each curve is an average of spectra obtained for several isolated holes of the same size. Figure taken from (Degiron *et al.*, 2004).

Another theoretical works (Catrysse *et al.*, 2005; Webb and Li, 2006) have investigated the existence of propagating waveguide modes for arbitrarily small diameters of a cylindrical hole. In these two references, it was demonstrated that the cutoff wavelength of the hole waveguide (perforated on a metal characterized by Drude dielectric function) does not approach zero when the hole radius tends to zero (as it occurs in a PEC), but to a constant value, $\sqrt{2}\lambda_p$, λ_p being the wavelength of the bulk plasmon.

Very recently, using terahertz-light excitation, Adam *et al.* (2008) were able to measure the time- and frequency dependent E-field in the vicinity of subwavelength circular holes (perforated in a 200nm-thick gold film deposited on a GaP substrate), with sub-wavelength spatial and sub-cycle temporal resolution. As expected from the calculations of Bouwkamp (1950) for a circular hole perforated on a PEC film, the E-field is highly concentrated near the edges of the hole. Interestingly, they also report the emergence of a transmission resonance that is spectrally located close to the cutoff frequency of the lowest order mode, the TE_{11} mode, calculated as if the hole were filled with a material whose refractive-index coincides with that of the substrate. Further theoretical investigations are needed in order to reveal the physics

behind this resonance and its relation with the cutoff transmission resonances appearing for rectangular and annular holes, as described in section II.B.2.

Apart from their transmission properties, circular holes have been also studied as nanometric generators of SPPs (Baudrion *et al.*, 2008; Chang *et al.*, 2005; Sonnichsen *et al.*, 2000; Yin *et al.*, 2004). The holes act as point-like sources of SPPs and the coupling efficiency can be as large as 20% (Baudrion *et al.*, 2008) by a proper design of the geometrical parameters.

2. Rectangular holes

To the best of our knowledge, the only experimental study of the optical transmission properties of a single rectangular hole perforated on a metal film was carried out by Degiron *et al.* (2004). These experiments demonstrated that the transmission properties of a single rectangular hole are very sensitive to the polarization of the incident light. Figure 9 shows the evolution of the transmission spectrum of a rectangular aperture (short side: $a_x = 210$nm, long side: $a_y = 310$nm) in a 700nm thick silver film for various incident linear polarizations. When the angle is 0^0, the E-field is pointing along the long side of the rectangular hole, whereas for 90^0, the direction of the E-field coincides with that of the short side of the rectangle. Two distinct peaks can be observed by simply changing the polarization of the incident field. As the angle varies from 0^0 to 90^0, one switches from a mode at around 450nm to another one at 750nm.

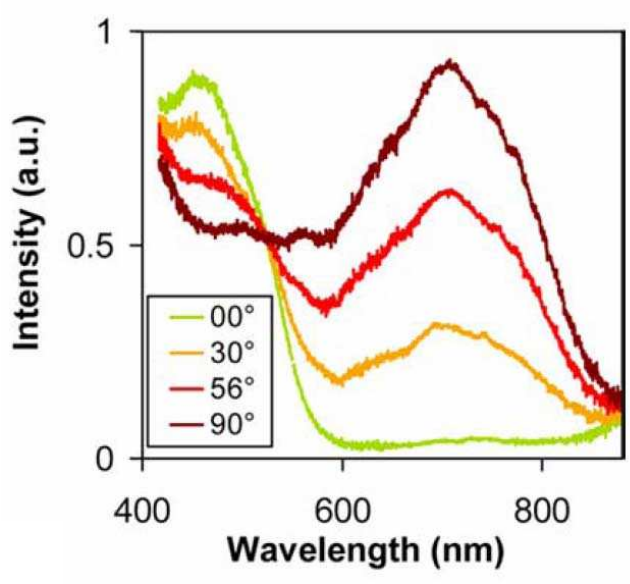

FIG. 9 Transmission spectra of an isolated rectangular aperture for various linear polarizations. The thickness of the free-standing silver film is $h = 700$nm and the sides of the rectangle are: $a_x = 210$nm and $a_y = 310$nm. Figure taken from (Degiron *et al.*, 2004).

Degiron *et al.* (2004) also analyzed the dependence of the transmission resonances with the aspect ratio of the rectangular hole. The experiments showed that the peak height increases and its spectral location shifts to larger wavelengths as the ratio between the two sides of the rectangle, a_y/a_x, is enlarged (see Figure 10). In all these spectra, normal incident light is linearly polarized and is pointing along the short side of the rectangular hole (x-direction).

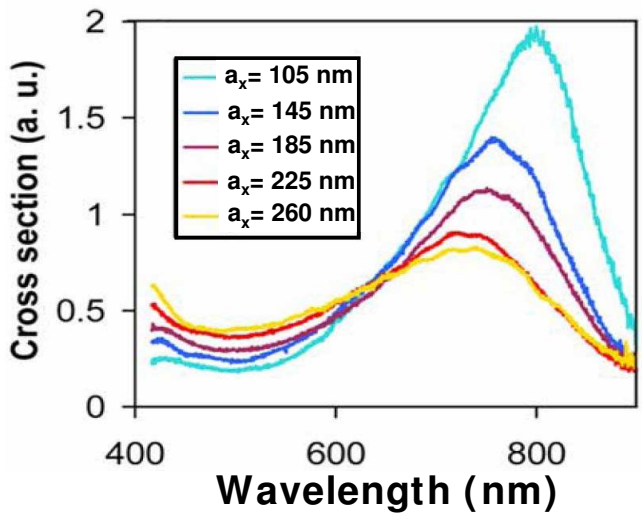

FIG. 10 Transmission spectra of isolated rectangular apertures with fixed $h = 300$nm and $a_y = 270$nm with various a_x ($105\text{nm} < a_x < 260\text{nm}$), perforated in silver films. All the structures are illuminated by a normal incident plane wave whose E-field points along the short side of the rectangle. Figure taken from (Degiron *et al.*, 2004).

In order to underpin the physical origin of these transmission resonances, we theoretically analyze the properties of a single rectangular hole of sides a_x and a_y perforated on a metallic film of thickness h (see inset of Fig. 11) by using the modal expansion formalism as described in section I.B. In the first part of this analysis the metal is treated as a PEC (Garcia-Vidal *et al.*, 2005b). Then, the effect of a finite dielectric constant on the resonant transmission properties of a single rectangular hole will be addressed (Garcia-Vidal *et al.*, 2006a). We focus on the case of p-polarized incident radiation, with the in-plane E-field component pointing to the x-direction (short side of the rectangle).

Figure 11 depicts the calculated normalized-to-area transmission spectra for rectangular holes in which the aspect ratio (a_y/a_x) is varied between 1.0 (square hole) and 10. For the calculation of these spectra we assume that the dielectric constants in all regions (reflection, transmission and inside the holes) is $\epsilon = 1$. The thickness of the PEC film is fixed in all cases at $h = a_y/3$. As we will show below, this is not an important parameter regarding the emergence of transmission resonances. As the ratio a_y/a_x is increased, a transmission peak develops close to the cutoff wavelength ($\lambda_C = 2a_y$), with increas-

ing maximum transmittance and decreasing linewidth. In all cases, above cutoff the transmittance decreases strongly with wavelength, due to both the evanescent decay of the EM fields inside the hole and to the poor coupling of the incident wave with the waveguide modes in this limit.

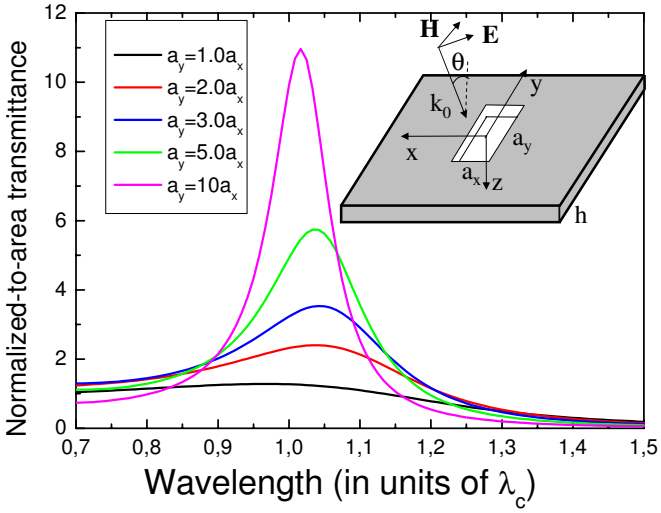

FIG. 11 Inset: schematic picture of a single rectangular hole of sides a_x and a_y perforated on a metallic film of thickness h. The structure is illuminated by a p-polarized plane. Main panel: normalized-to-area transmittance versus wavelength (in units of the cutoff wavelength, $\lambda_C = 2a_y$) for a normal incident p-polarized plane wave impinging on single rectangular holes, for different ratios a_y/a_x. Metal thickness is fixed at $h = a_y/3$. Figure taken from (Garcia-Vidal *et al.*, 2005b).

As in the case of a single slit, a very good approximation to the final result can be achieved by considering only the first TE waveguide inside the hole, $|TE>$ in the Dirac notation. Its normalized in-plane E-field components are:

$$< \vec{r}\,|TE >= \sqrt{2/(a_x a_y)}\,\sin[\frac{\pi}{a_y}(y+1/2)](1,0)^T \qquad (13)$$

Within the single mode approximation, the set of Eqs.(3) also applies for this case. The magnitudes appearing in those two equations are now: $\Sigma = Y_{TE}/\tan(q_z h)$ and $G^V = Y_{TE}/\sin(q_z h)$ where the propagation constant of the TE mode, is given by $q_z = \sqrt{k_\omega^2 - (\pi/a_y)^2}$. Its associated admittance is $Y_{TE} = q_z/k_\omega$. Normalizing the incident p-polarized plane wave such that the incoming energy flux over the hole area is unity, we obtain for the illumination term:

$$I = \frac{4i\sqrt{2}}{\pi}\frac{\mathrm{sinc}[k_\omega a_x \sin\theta/2]}{\sqrt{\cos\theta}} \qquad (14)$$

where θ is the angle of incidence and function $\mathrm{sinc}(x) \equiv \sin/x$. The expression for the self-illumination of the fundamental TE mode via vacuum modes, G, for the case of a rectangular hole is:

$$G = \frac{ia_x a_y}{8\pi^2 k_\omega}\int_{-\infty}^{+\infty}\int_{-\infty}^{+\infty} dk_x\, dk_y\, \frac{k_\omega^2 - k_y^2}{\sqrt{k_\omega^2 - k^2}}\,\mathrm{sinc}^2(\frac{k_x a_x}{2}) \times [\mathrm{sinc}(\frac{k_y a_y + \pi}{2}) + \mathrm{sinc}(\frac{k_y a_y - \pi}{2})]^2 \qquad (15)$$

where $k^2 = k_x^2 + k_y^2$.

For the case of a rectangular hole, the resonant condition $|G - \Sigma| = |G^V|$ reads:

$$\tan(q_z h) = \frac{2Y_{\mathrm{TE}}\mathrm{Re}(G)}{|G|^2 - Y_{\mathrm{TE}}^2}. \qquad (16)$$

This equation marks the spectral position of Fabry-Perot resonances. Due to the coupling to free-space modes, these resonances are shifted from those predicted from the approximate expression $\tan(q_z h) = 0$, which would arise if the optical path inside the hole were only taken into account. Equation (16) is satisfied at cutoff, when $q_z = Y_{TE} = 0$. Therefore, the physical origin of the transmission resonances appearing for rectangular holes at $\lambda \approx \lambda_C$ stems from the excitation of Fabry-Perot resonances in which the propagation constant is zero.

Notice that the only dependence of the transmittance on the angle of incidence stems from the illumination term, I. Then, the location of the resonant peaks observed in Figure 11 does not depend on θ. Moreover, in the extreme subwavelength limit, the term sinc in I [see Eq.(14)] approaches 1 yielding to a simple $1/\cos\theta$ dependence for the peak heights in the normalized-to-area transmittance spectra.

An accurate analytical approximation for the transmittance at resonance, T_{res}, can be obtained by making use of the general expression previously derived, $T_{\mathrm{res}} = |I|^2/[4\mathrm{Im}G]$. In the extreme subwavelength regime, we obtain from Eq.(15), $\mathrm{Im}(G) \approx 32 a_x a_y/(3\pi\lambda^2)$, leading to:

$$T_{\mathrm{res}} \approx \frac{3}{4\pi}\frac{\lambda_{\mathrm{res}}^2}{a_x a_y}. \qquad (17)$$

This expression predicts that, for the transmission peak located near the cutoff wavelength, $T_{\mathrm{res}} \approx (3/\pi)a_y/a_x$, explaining the numerical results shown in Fig. 11, in which an almost linear increase of the peak height versus ratio a_y/a_x is observed.

Additionally, even for a fixed aspect ratio a_y/a_x, Eq. (17) gives us a clue for further enhancing the transmission: namely, by filling the hole with a material with dielectric constant $\epsilon > 1$, as this increases the cutoff wavelength. Now, the propagation constant of the fundamental TE mode is $q_z = \sqrt{\epsilon k_\omega^2 - (\pi/a_y)^2}$ and its cutoff wavelength is $\lambda_C = 2\sqrt{\epsilon}a_y$. According to Eq.(17), this should lead to a linear increase of T_{res} with ϵ. Note that

this increase of the transmission when the hole by filled with material with $\epsilon > 1$ also occurs for the case of circular or square holes (De Abajo, 2002). Remarkably, in rectangular holes, this mechanism acts almost independently to the "geometric" enhancement appearing at large aspect ratios, so $T_{\rm res}$ is proportional to both a_y/a_x and ϵ.

Associated with this resonant phenomenon, there is an enhancement of the EM fields. A direct evaluation of $|E|^2 = |E'|^2$ at the resonant condition yields:

$$|E|^2_{\rm res} = |E'|^2_{\rm res} = \frac{|I|^2}{4[{\rm Im}(G)]^2}, \qquad (18)$$

leading to an enhancement of the intensity of the E-field at the hole (with respect to the incident one) that scales with $\lambda_{\rm res}$ as $\lambda^4_{\rm res}/(a_y a_x)^2$, much larger than the enhancement in the transmittance. This implies that, in the process of resonant transmission, light is highly concentrated on the entrance and exit sides of the hole and only a small fraction of this light is finally transmitted. Still, as we have seen, the transmitted light is larger than the one directly impinging in the hole.

Experimental verification of the existence of cutoff transmission resonances in rectangular holes was recently reported by Lee *et al.* (2007), in the THz regime of the EM spectrum. These authors considered sets of rectangular holes where all holes had the same dimensions and orientation, but were randomly positioned. The measured transmission spectra confirmed the existence of resonances associated with the cutoff. In Figure 12, three representative transmission spectra are displayed, that show the predicted increase in the transmittance as the aspect ratio of the rectangular hole is increased.

It is clear that the transmission resonances appearing for a rectangular hole perforated on a PEC film have strong similarities with those found experimentally by Degiron *et al.* (2004) in the optical regime. In particular, the experimentally observed increase in the transmittance at resonance with increasing aspect ratio suggests that their physical origin also stems from the excitation of Fabry-Perot cavity resonances of zero-propagation constant. This hypothesis was theoretically verified by Garcia-Vidal *et al.* (2006a). By combining a modal expansion formalism in which SIBC were applied along with FDTD numerical simulations, these authors found the close correspondence between the spectral location of the transmission peak with the cutoff wavelength of the hole waveguide perforated on a real metal. This cutoff wavelength is red-shifted with respect to its PEC-value, due to the penetration of the EM-fields inside the metal at optical frequencies (Gordon and Brolo, 2005).

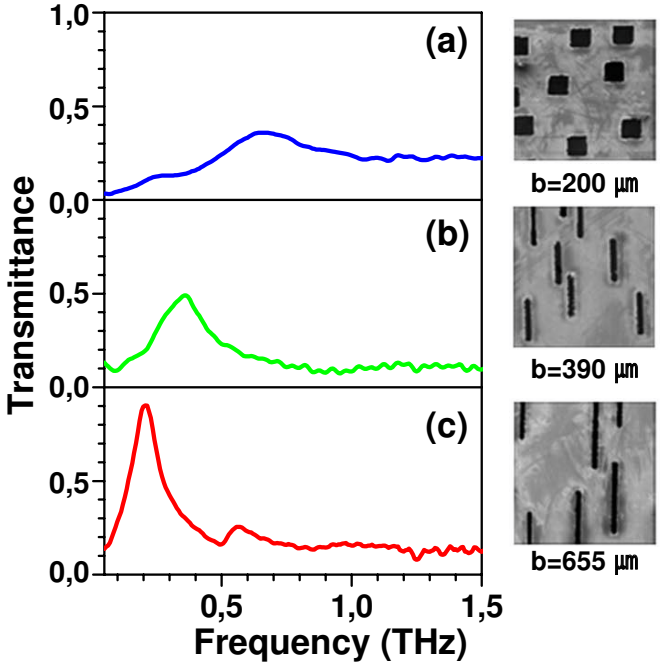

FIG. 12 Normalized transmission amplitudes, at normal incidence, of random arrays of holes with dimensions: (a) Square holes with $a_x = a_y = 200\mu m$. (b) Rectangular holes with $a_x = 70\mu m$ and $a_y = 390\mu m$. (c) Rectangular holes with $a_x = 70\mu m$ and $a_y = 655\mu m$. In the three cases the metal thickness is fixed at $h = 17\mu m$. Insets are SEM images of the 2D random arrays. Figure taken from (Lee *et al.*, 2007).

III. TRANSMISSION THROUGH ARRAYS OF APERTURES

A. 1D periodic arrays of slits

1. General results

Before the discovery of the EOT phenomenon in periodic arrays of subwavelength holes (Ebbesen *et al.*, 1998), there had only been a few theoretical and experimental works on the resonant transmission features of the so-called transmission gratings, i.e., periodic arrays of 1D slits perforated on metallic films (see Fig. 13). An interesting experimental and theoretical study was carried out by Lochbihler (1994) in gold wire gratings illuminated by *p*-polarized radiation. This author reported the emergence of very narrow transmission dips in the zero-th diffraction order. Lochbihler modelled the scattering process using a modal formalism, and was able to relate the spectral location of the transmittance dip with the dispersion relation of the SPPs supported by the gold surface.

After 1998, many theoretical works have been devoted to analyzing the emergence of EOT phenomenon in 1D transmission gratings for *p*-polarized light. Notice that no transmission resonances are expected to appear for *s*-polarized radiation. Schroter and Heitmann (1998) presented the first numerical study, based on the Chan-

denzon method in combination with the point matching method. They studied the case of p-polarized light finding that, as in the case of the experiments in the 2D structures, the transmission spectrum presented peaks, whose spectral locations indicated that SPPs were involved in the resonant transmission behavior.

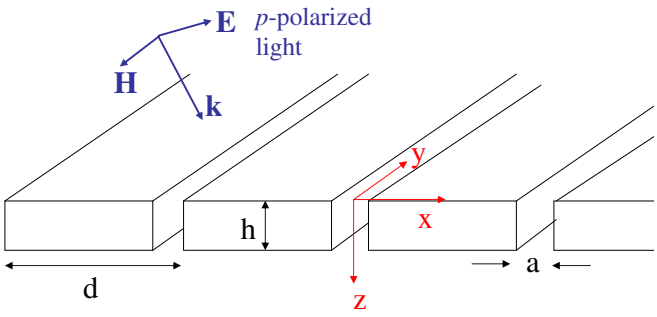

FIG. 13 Schematic picture of a periodic array of slits (period d, width of the slits, a) perforated on a metallic film of thickness h. The structure is illuminated by p-polarized radiation, with the E-field lying in the $x-z$ plane.

In a posterior development, Porto *et al.* (1999) demonstrated that there are two possible ways of transferring p-polarized light efficiently from the upper surface to the lower one: by the excitation of coupled SPPs on both surfaces of the grating (very similar to the 2D case) or by the coupling of the incident plane wave with cavity resonances located inside the slits (similar to those found in the single slit case described in section II.A). The existence of these two channels for enhancing the transmittance through a periodic array of subwavelength slits has been corroborated by many posterior theoretical studies (Astilean *et al.*, 2000; Collin *et al.*, 2001, 2002; Garcia-Vidal and Martin-Moreno, 2002; Hooper and Sambles, 2003; Lalanne *et al.*, 2000; Lee and Park, 2005; Liu and Tsai, 2002; Marquier *et al.*, 2005). Different names have been used to call them: horizontal and vertical resonances, surface and cavity resonances, etc... The two resonant mechanisms are mixed in a way that depends strongly of the geometrical parameters of the structure (Collin *et al.*, 2001, 2002; Marquier *et al.*, 2005). This is due to the existence of a propagating mode inside the slit for p-polarized light (the TEM mode previously discussed in section II.A). A criticism to this point of view regarding the origin of the transmission resonances has been supported by different authors (Cao and Lalanne, 2002; Crouse and Keshavareddy, 2005; Xie *et al.*, 2005). Based on the existence of a transmission minimum appearing at the spectral location of the SPP in a flat, un-corrugated metal surface, these authors have claimed that the excitation of SPPs is detrimental for the transmission. We will show later on in section III.A.2 that the dispersion relation of the SPPs changes when the metal film is perforated with a 1D array of slits and, indeed, the transmission peaks emerge at the spectral locations of the SPPs for the corrugated surface. A different perspective has been put forward by Treacy (Treacy, 1999, 2002) who argues that the transmission anomalies can be better explained in terms of a dynamical diffraction theory, in which SPPs are an intrinsic component of the diffracted EM fields.

Up to now, there have been far fewer experimental studies on the transmission properties of 1D arrays of slits than of 2D arrays of holes. In the microwave regime, Sambles and co-workers (Hibbins *et al.*, 2001; Went *et al.*, 2000) reported the appearance of selective transmission at resonant wavelengths associated with the excitation of cavity resonances. Barbara and colleagues (Barbara *et al.*, 2002) presented the first study in the optical regime with a gold coated silica gratings and they were able to interpret their results by invoking the excitation of both SPPs and slit-cavity resonances. In a posterior development, two different experimental groups (Steele *et al.*, 2003; Sun *et al.*, 2003) reported the emergence of transmission resonances associated with the excitation of SPPs in very thin metallo-dielectric gratings. The transmission properties of THz radiation pulses were studied in very thick transmission gratings containing subwavelength slits (Xing *et al.*, 2006)

More recently, Pang *et al.* (2007) have measured the dispersion relation of the transmission resonances appearing in 1D arrays of subwavelength slits, both in the visible and near infrared ranges of the EM spectrum. The inset of Figure 14 renders a SEM image of a slit array perforated in a gold film of thickness $h = 400$nm deposited on a glass substrate. The period of the array is $d = 750$nm and the width of the slits is 100nm.

The experimental transmission spectra rendered in Fig. 14 corroborate the theoretical predictions regarding the existence of two different channels that enhance the transmission through a 1D periodic array of slits. Panel (a) shows a zero-order transmission spectra for two different thicknesses $h = 400$nm and $h = 450$nm. Due to the presence of a substrate, the resonant features associated with the SPPs of the metal-substrate interface appear at $\lambda \approx d\sqrt{\epsilon_{glass}} = 1125$nm. On the other hand, the spectral location of the slit cavity resonance is expected to appear at a wavelength larger than $2h = 800 - 900$nm. The two main transmission peaks emerging in the spectrum result from the strong interplay between these two types of resonances (Collin *et al.*, 2001, 2002; Marquier *et al.*, 2005). This interaction is better visualized in panel (b) where a dispersion diagram of the transmission peaks as a function of parallel momentum is presented. The SPP mode of the glass-metal interface (SM-1) overlaps with the cavity resonance at ca. 1.1eV (marked by a dashed line, FP), provoking the opening of a gap of ca. 280 meV. Full lines display the dispersion relation of the different SPP modes of the flat interfaces.

Similar transmission resonances to those described above have also been observed in transmission gratings perforated on doped semiconductors at THz frequencies (Gomez-Rivas *et al.*, 2005; Parthasarathy *et al.*, 2007) and on SiC films at NIR wavelengths (Marquier *et al.*, 2004). In this last case, it has been demonstrated how

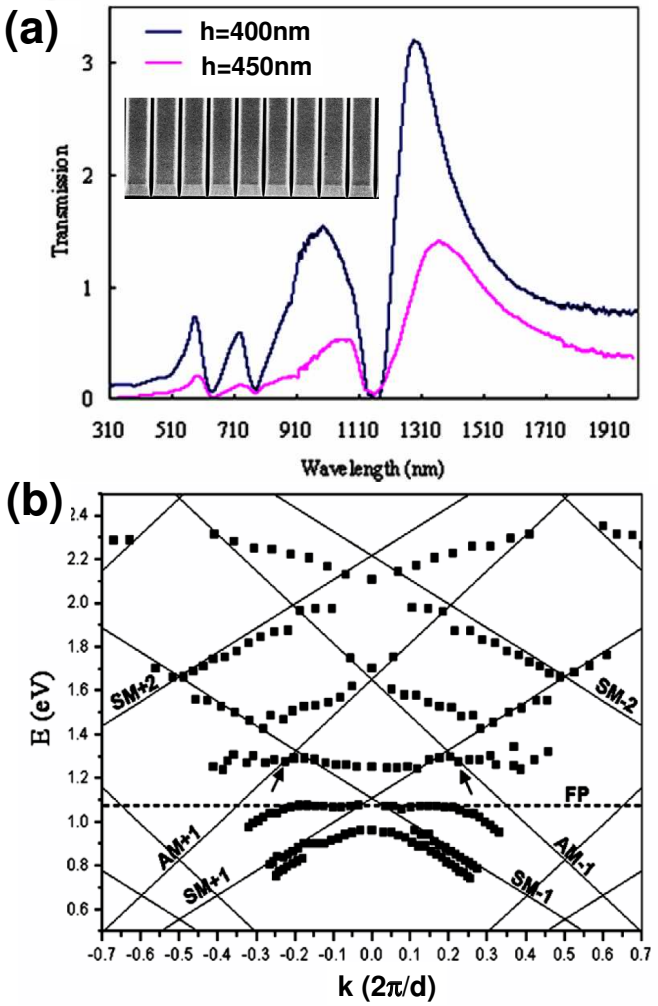

FIG. 14 (a) Inset: SEM image of one of the 1D arrays analyzed in these experiments. Main panel: zero-order transmittance of a 1D slit array illuminated by a normal incident p-polarized plane wave. The period of the array is $d = 750$nm, the width $a = 100$nm and two different thicknesses are analyzed, $h = 400$nm and $h = 450$nm. (b) Dispersion diagram [spectral locations of the transmission peaks versus energy (in eV) and parallel momentum (in units of $2\pi/d$)] for the sample analyzed in panel (a) with $h = 400$nm. Figure taken from (Pang *et al.*, 2007).

surface phonon polaritons play the same key role as SPPs do in the metallic case. Finally, some interesting transmission properties emerging in compound gratings (formed by slit arrays in which the unit cell is composed by more than one slit) have been recently reported (Fong and Hui, 2006; Hibbins *et al.*, 2006; Skigin and Depine, 2005, 2006). By adding slits to the period, new phase resonances appear as sharp dips within the transmission maxima associated with the excitation of Fabry-Perot modes (Hibbins *et al.*, 2006; Skigin and Depine, 2005).

2. Theoretical modelling

In what follows we describe the theoretical foundation of the transmission resonances appearing in a periodic array of 1D slits illuminated by p-polarized light by using the modal expansion formalism described in section I.B. We first consider the case of a perforated PEC film (in which no SPPs can be excited and there is no absorption). In the second part of this study, we shall show how this PEC picture is slightly modified when a real metal in the optical regime (and its associated SPPs) is considered.

As in previous cases, the system of equations (1) is also valid for describing the transmission properties of the structure depicted in Figure 13. Now objects α are just Bloch combinations of TM waveguide modes inside the slits. As we are dealing with a periodic array, $G_{\alpha\beta}$ can be written as a discrete sum over p-polarized diffracted modes:

$$G_{\alpha\beta} = i \sum_{\vec{k}} \frac{k_\omega}{k_z} < \alpha|\vec{k}p >< \vec{k}p|\beta > \qquad (19)$$

where $\vec{k} = \vec{k}_0 + \vec{k}_R$, $\vec{k}_R$ being a reciprocal lattice vector ($\vec{k}_R = 2\pi n/d$). In Figure 15 we show the transmittance spectra for a 1D array of slits of period d, width $a = 0.2d$ and different values of h (ranging from $h = 0.2d$ to $h = 0.8d$). Note that as the PEC approximation is considered, d can be used as a unit length of the structure. The system is illuminated by a normal incident p-polarized plane wave and the modal expansion of the EM fields inside the slits contains 10 TM modes (full lines). A series of transmission peaks (reaching 100% transmission) dominate the spectrum. Two types of transmission resonances can be distinguished: very narrow transmission peaks appearing at a wavelength close to d and wider peaks emerging at larger wavelengths. These are the two types of transmission resonances previously discussed. An interesting point is that the transmission peak emerging close to d also appear in a perforated PEC film which, in principle, does not support SPPs. As we shall show later, the physical origin of this resonant feature stems from the excitation of geometrically-induced surface EM modes that mimic the behavior of SPPs in perforated PEC structures.

A quasi-analytical treatment of this problem can be carried out (Garcia-Vidal and Martin-Moreno, 2002) by realizing that considering only the TEM mode ($\alpha = 0$) inside the slits already leads to very accurate results for the transmittance (see dotted lines in Fig.15). Within the single mode approximation, the zero-order transmission coefficient can be obtained from the multiple scattering expression described in section I.B; see Eq.(5):

$$t_0 = \frac{\tau^{12} e^{ik_\omega h} \tau^{23}}{1 - e^{2ik_\omega h}\rho^2} \qquad (20)$$

where $t_0 \equiv t_{\vec{0}p}$, $\tau^{12} \equiv \tau_0^{12}$, $\rho \equiv \rho_{00}^{23} = \rho_{00}^{21}$ and $\tau^{23} \equiv \tau_{0,\vec{0}p}^{23}$.

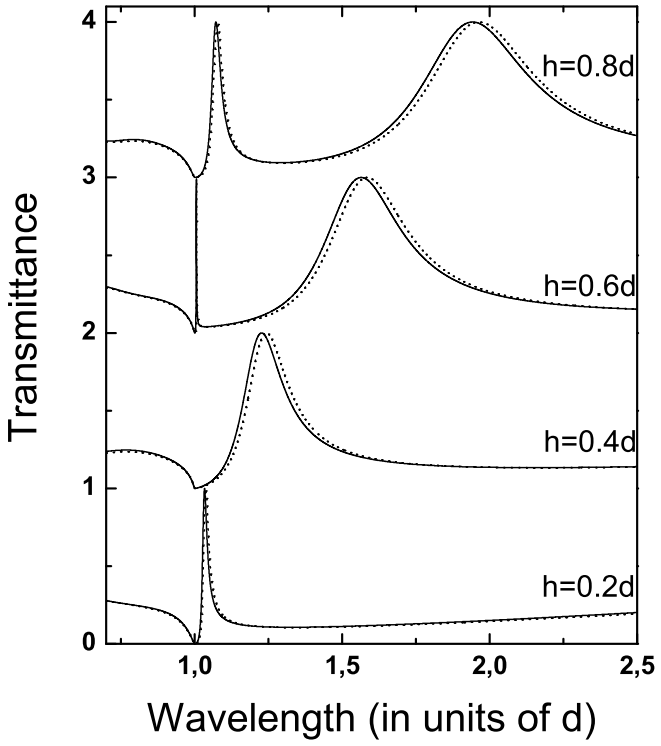

FIG. 15 Total transmittance (normalized to the unit cell of the array) of a normal incident p-polarized plane wave versus wavelength (in units of d) for periodic arrays of slits of fixed width, $a = 0.2d$, and several thicknesses, $h = 0.2d, 0.4d, 0.6d$ and $0.8d$. Full lines show the calculations in which 10 TM waveguide modes are considered whereas dotted lines render the results when only the TEM mode ($\alpha = 0$) is included.

All these scattering magnitudes can be related to $G \equiv G_{00}$:

$$\rho = -\frac{G-i}{G+i}, \tau^{12} = \frac{I_0}{G+i}, \tau^{23} = \frac{2i < \vec{k}_0 p|0>}{G+i} \qquad (21)$$

where the overlap integral, $< 0|\vec{k}p >= \sqrt{\frac{a}{d}}\mathrm{sinc}(k_x a/2)$. The complex two-media reflection coefficient, ρ, is characterized by its modulus (R) and phase, θ. Then, we can define a total phase, $\phi = 2\theta + 2k_\omega h$, sum of the scattering (associated with ρ) and geometrical (determined by the optical path) phases. As a function of this total phase, the zero-order transmission coefficient in Eq.(20) can be expressed as:

$$t_0 = \frac{\tau^{12} e^{ik_\omega h} \tau^{23}}{1 - R^2 e^{i\phi}} \qquad (22)$$

Equation (22) resembles the formula governing the transmission properties of a Fabry-Perot interferometer. In contrast to the canonical case in which the phase of the EM fields inside the cavity is determined by the optical path ($2k_\omega h$), a periodic array of 1D slits presents an additional ingredient for the phase accumulated in a round trip inside the slit, the one associated with the phase of ρ. Figure 16 analyzes the behavior of R and θ for three different values of a/d. Both the modulus and the phase of ρ present singular behavior at wavelengths d, $d/2$, $d/3$,...This is due to the fact that G diverges at the condition $k_z = 0$ [see Eq.(19)] that, for normal incidence, coincides with $\lambda = d/n$, with n integer. At those particular wavelengths, Eq.(21) predicts $\tau^{12} = \tau^{23} = 0$ and $\rho = -1$, provoking the appearance of zeroes in the transmittance, as shown in Fig.15. An interesting point is that there is a phase jump between 0 and π in ρ when λ crosses those singular conditions [see Fig.16].

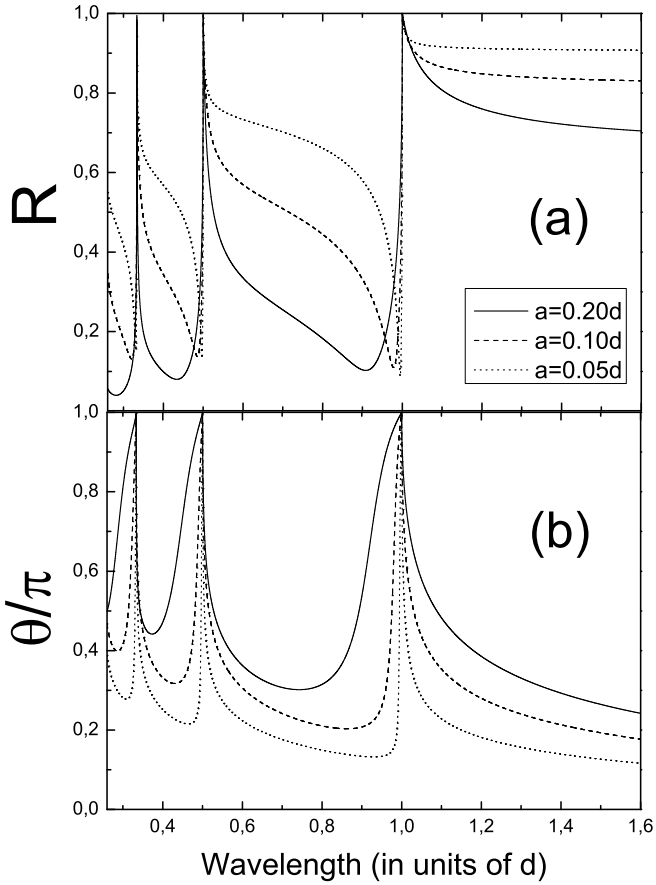

FIG. 16 Dependence of ρ versus wavelength for three different values of the ratio between the width of the slits and period of the array, a/d. Panel (a) shows the modulus of ρ (R) and panel (b) renders its phase (θ), in units of π.

Given that for narrow slits $R \approx 1$, it is found that whenever ϕ is an integer times 2π, there would be a transmission peak associated with a resonant condition for the denominator in Eq.(22). For thin PEC films, the total phase is dominated by the scattering phase; correspondingly, the spectral location of the transmission resonance appears at a wavelength slightly larger than d (see the case $h = 0.2d$ in Fig.15). When h is increased, the situation is more complex and the geometrical phase ($2k_\omega h$) can also lead to the appearance of transmission peaks emerging at $\lambda \gg d$. The physical origin of these trans-

mission resonances stems from the excitation of cavity resonances, similar to the ones emerging in single slits as discussed in section II.A.

However, there is a fundamental question regarding the origin of the transmission peak at λ close to d. Notice that, up to this point, we have discussed the situation within the PEC approximation and, hence, there are no SPPs involved. However, in a PEC film, when the metal is perforated with a periodic array of indentations, surface EM modes can built-up (Munk, 2000). Let us now describe the link between the transmission resonances previously reported and the existence of surface EM modes in the structure.

The surface EM modes relevant to the transmission process must be leaky modes (otherwise they could not be excited by an incident plane wave). However, in a first approximation, we can look for the existence of truly-bound surface EM modes by working with a parallel momentum k_x longer than k_ω and ignoring diffraction effects (which are incorporated in a second step). The dispersion relation (frequency versus k_x) of the p-polarized EM modes supported by the structure can be calculated using Eq.(3). Within these conditions, G in Eq.(3) is a real magnitude, $G = \frac{a}{d}\frac{k_\omega}{\sqrt{k_x^2-k_\omega^2}}$. In this limit, the denominator of Eqs.(4) can be exactly zero at the condition $G - \Sigma = \pm G^V$, leading to the following dispersion relation for the EM modes supported by the structure:

$$\frac{\sqrt{k_x^2 - k_\omega^2}}{k_\omega} = \frac{a}{d}\frac{\sin k_\omega h}{\cos k_\omega h \pm 1} \qquad (23)$$

where the sign (+) must be taken when $\sin k_\omega h > 0$ and sign (−) when $\sin k_\omega h < 0$. This equation gives the dispersion relation of the bound EM modes supported by the structure within the effective medium limit ($\lambda \gg d, a$).

Figure 17 illustrates the close link between the spectral locations of these EM modes and the peaks in the transmittance spectrum, as a function of k_x. In panel (a) we analyze the case $h = 0.2d$. Here, the dispersion relation (white line) runs close to the light line ($\omega = ck_x$). The important point to realize is that if $\lambda < 2d$ and diffraction effects are taken into account, these EM modes become leaky and can be excited by an impinging propagating plane wave. In the left part of panel (a), the transmittance versus wavenumber and k_x within the light cone is rendered. It is clear that the location of the transmission peak at $\lambda \approx d$ at normal incidence can be obtained by folding the dispersion relation inside the light cone. Therefore, we conclude that the physical origin of the transmission peak located at $\lambda \approx d$ is related to the excitation of an EM guided mode. Due to the fact that the two surfaces of the PEC film are always connected via a propagating wave (the TEM mode), the thickness of the film is a key factor. Correspondingly, this EM mode is not a true surface mode but a guided mode; it is a mode bound to the film, guided inside the metal and decaying away from it. It resembles more a guided mode in a dielectric slab. In fact, it has been demonstrated that a 1D array of subwavelength slits can be considered as a metamaterial and can be rigorously mapped into a high refractive index dielectric slab (Shen *et al.*, 2005). We shall see later that the case of a 2D hole array is different: the geometrically-induced EM modes are truly surface EM modes, due to the existence of a cutoff wavelength in 2D apertures (see section III.B.2). The close correspondence between dispersion relation of the EM modes and transmission peaks also occur for thicker films (see Fig.17(b), $h = 1.0d$). For large enough h, the dispersion relation presents flat parts, associated with the Fabry-Perot condition $\cos k_\omega h = \pm 1$, which dominate the transmission spectrum.

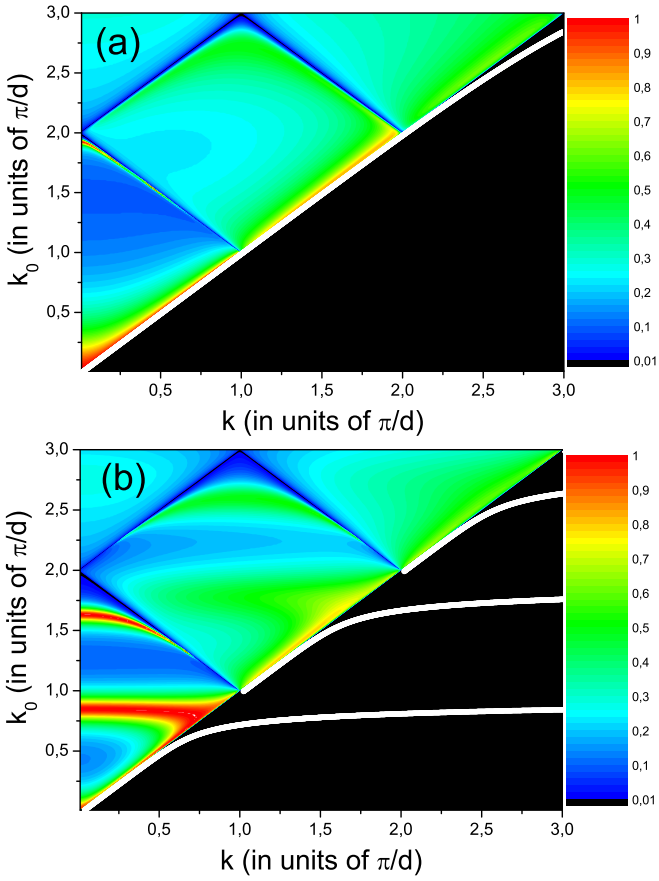

FIG. 17 Left panels: Transmittance spectra as a function of both wavenumber and wavevector for p-polarized light impinging at two different arrays of slits. Right panels: dispersion relation for the EM guided modes as obtained from Eq.(23). Upper panel (a): $a = h = 0.2d$. Lower panel (b): $a = 0.2d$ and $h = 1.0d$.

What occurs to these transmission resonances when the metal is not a PEC? As explained before, within the modal expansion formalism, the dielectric function of the metal can be approximately considered by using the surface impedance boundary conditions (SIBC) when matching the EM fields at the two horizontal interfaces of the structure. In this way, the system of Eqs.(1) still holds but now the different magnitudes depend on the

surface impedance of the metal, Z_S. Detailed expressions for Σ_α, I_α and G_α^V can be found in appendix A. The most important change resides in the propagator $G_{\alpha\beta}$, which for a 1D array of slits reads:

$$G_{\alpha\beta} = i \sum_{\vec{k}} \frac{Y_{\vec{k}p}}{1 + Z_S Y_{\vec{k}p}} < \alpha | \vec{k}p >< \vec{k}p | \beta > \qquad (24)$$

Due to that, now the minimum of the transmittance would not emerge at $\lambda = d$, as in the case of a PEC film, but at a slightly larger wavelength. This can be easily understood by realizing that the divergence of G now appears at the condition $1 + Z_S Y_{\vec{k}\sigma} = 0$. This last condition is just the condition for the existence of SPP on a flat metal surface within the SIBC approach. Therefore, in a real metal, the spectral locations of the transmission minima are related to the SPP condition for a flat (with no indentations) metal film. The peak appearing at a wavelength slightly larger than d is then associated with the excitation of a guided EM mode whose dispersion relation has both dielectric (linked to a finite ϵ) and geometry contributions (due to the presence of the slits). The important point to realize is that the linewidth of these transmission resonances are much smaller than the Fabry-Perot ones and, therefore, are much more sensitive to the presence of absorption in a metal at optical frequencies. More details on the dependence of the transmission peaks with the absorption in the metal were discussed by Garcia-Vidal and Martin-Moreno (2002).

As described above, the two types of transmission resonances previously discussed also appear in a real metal at optical frequencies. Several theoretical analysis (Catrysse *et al.*, 2006; Collin *et al.*, 2001, 2002; Marquier *et al.*, 2005) have demonstrated that transmission and absorption peaks coincide, and can be then attributed to resonances of the structure. As in the case of a PEC film, these resonances can be viewed as the result of a strong hybridization between cavity modes (Fabry-Perot) and SPPs. Moreover, Marquier *et al.* (2005) characterized this hybridization between cavity modes and SPPs in the transmission resonances. Fig. 18 presents their results for a free-standing silver film with $d = 500$nm, $a = 50$nm and $h = 400$nm. Panel (a) shows the transmission versus both frequency and parallel momentum. The similarities between this plot and the ones obtained for a perforated PEC film (see Fig.17) are remarkable. Panel (b) renders the branch B-C of the dispersion relation of the mode responsible for enhanced transmission is rendered, whereas panel (c) shows the surface-cavity ratio (SC) as a function of parallel momentum. This SC ratio is calculated by comparing the EM energies associated with the cavity and SPP components of the guided mode. This is quantitatively done by integrating the EM energy within the slit (cavity component) and on both interfaces (SPP component), respectively. As shown in Fig.18, for $k_x = 0$, the character of the mode is mainly cavity-like (75% for the geometrical parameters considered in this study). As the parallel momentum is increased, the character is evolving to SPP-like.

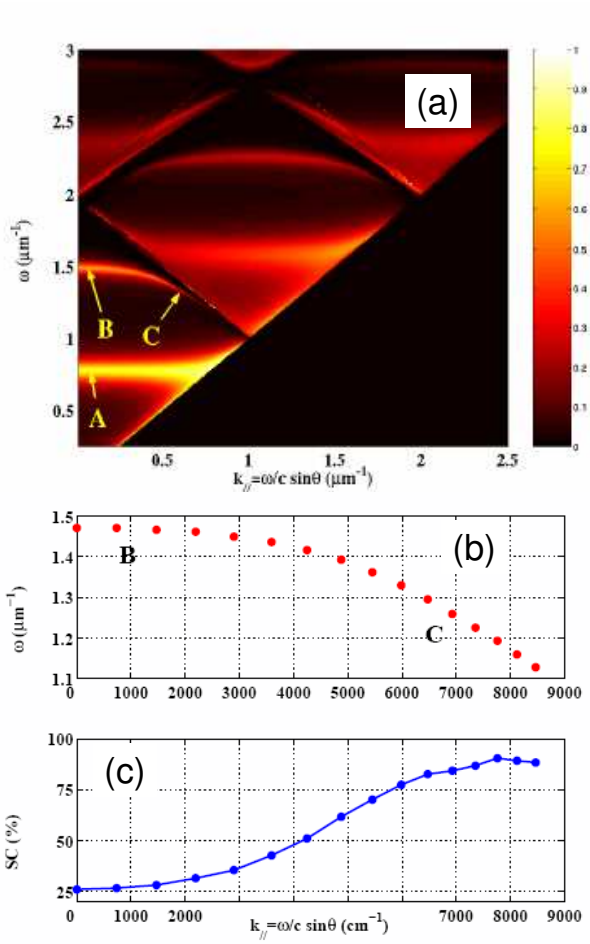

FIG. 18 (a) Transmission efficiency as a function of ω and k_x. Period of the grating, $d = 500$nm, width of the slits, $a = 50$nm and thickness $h = 400$nm. (b) Branch B-C of the dispersion relation and (c) surface-cavity ratio (SC) for the transmission branch displayed in (b). Figure taken from (Marquier *et al.*, 2005).

B. 2D periodic arrays of holes

1. General results

The first observation of EOT phenomenon through subwavelength hole arrays was made on 200 nm thick gold and silver films perforated with a square lattice of circular subwavelength holes (Ebbesen *et al.*, 1998). Figure 19 presents a SEM image of a typical 2D hole array exhibiting EOT. In this first experiment, transmissions twice as high as the open air fraction were observed. This observation was all the more surprising as conventional theory for light transmission through subwavelength apertures (Bethe, 1944; Bouwkamp, 1950) predicts a transmission normalized to the hole area that is sub-

stantially less than 1 (see section II.B.1). A typical EOT transmission spectrum is characterized by a sequence of maxima and minima (see Figure 20).

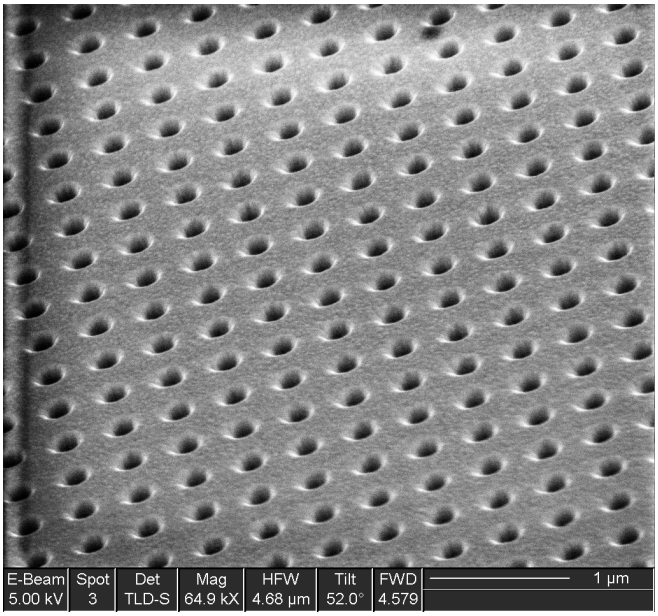

FIG. 19 SEM image of a 2D hole array of circular holes (diameter 150nm) milled in a 260nm thick Au film that is deposited on a glass substrate. The hole arrays count 30×30 holes and the period of the square array is 460nm. Image courtesy of Eric Laux.

In order to place EOT in a historical perspective, it must be noted that 2D hole arrays had been extensively studied before 1998, mainly due to their applications as selective filters. For this, the high-pass filtering properties are provided by the evanescent decay of the EM fields inside the holes for wavelengths larger than the cutoff wavelength, and the poor coupling of radiative EM modes to subwavelength holes. The low-pass filtering arises from the redistribution of energy caused by the periodic array when a new diffraction order becomes propagating, therefore carrying away energy at angles different from the incident one. More precisely, hole arrays were known to act as band-pass filters for $d < \lambda < \lambda_C$, where λ_C is the hole cutoff wavelength and d the lattice parameter. This property has been studied in several frequency regimes, such as microwave (Keilmann, 1981), far infrared (Mitsuishi *et al.*, 1963), mid infrared (Ulrich, 1967) and infrared (Rhoads *et al.*, 1982). However, the EOT phenomenon presented two main differences with previous works. First, experiments were performed in the optical regime, where there are EM modes bound to the metal surface (SPPs), which could play an important role in the transmission process. Second, the geometrical parameters defining the structure were such that $\lambda_C < d < \lambda$, i.e., the holes were at cutoff where EOT peaks occurred. This is not a minor point as, combined with the mentioned weak coupling of subwavelength holes to radiation modes, it is responsible for the appearance of well defined narrow resonant peaks. The EOT parameter range could, certainly, have been considered before 1998. However, after extensive literature searches, these authors have been unable to find any study on hole arrays in the regime $\lambda_C < d < \lambda$ prior to 1998. Perhaps the EOT parameter range was not explored before because nothing remarkable was expected for wavelengths beyond cutoff.

The observation of the EOT phenomenon sparked a huge amount of research trying to unveil the underlying mechanisms. The first report (Ebbesen *et al.*, 1998) already suggested a crucial role of SPPs and presented dependencies on: hole size, lattice spacing, metal film thickness and angular dispersion. Later, several other important parameters and observations were made: type of metal, the role of symmetry in the dielectric-metal-dielectric layer stack, the finite-size effects of the lattice and the role of hole shape.

The first key observation was the clear spectral dependence on lattice period of the minima and maxima for transmission. The position of the minima exhibit a linear dependence of the lattice period. In the first experimental report, the position of the minimum was ascribed to the spectral location of the so-called Wood-Rayleigh's anomaly. At this condition, a diffraction order is exactly parallel to the plane of the metal film. On the other hand, transmission maxima exhibit almost the same scaling behavior with lattice period as the minima. Ghaemi *et al.* (1998) suggested that maximum transmission occurs for those optical frequencies for which the wavevector of a SPP is equal to a vector of the reciprocal lattice associated to the geometry of the array. More generally speaking, transmission maxima could be obtained when the following condition is fulfilled:

$$\vec{k}_{sp} = \vec{k}_{in} + \vec{k}_R, \tag{25}$$

where $\vec{k}_{sp}$ and $\vec{k}_{in}$ are the wavevectors of the SPP and the incident plane wave, respectively; $\vec{k}_R = n\vec{b}_1 + m\vec{b}_2$ is a wavevector of the reciprocal lattice (expressed as a linear combination of the primitive vectors, $\vec{b}_1$ and $\vec{b}_2$). There are SPP modes bond to both metal-dielectric interfaces. Hence, two sets of transmission maxima occur, one for each interface, when the dielectrics on either side of the metal film are different. The dispersion relation for a SPP on a flat metal-dielectric interface is given by

$$k_{sp} = \frac{\omega}{c}\sqrt{\frac{\epsilon_M \epsilon_d}{\epsilon_M + \epsilon_d}}, \tag{26}$$

where ϵ_M and ϵ_d are the electric permittivities of the metal and dielectric, respectively.

This implies that the spectral location of the Wood-Rayleigh's anomaly is very similar to the condition for SPP excitation on a flat metal-dielectric interface of a good metal: notice that for $|\epsilon_m| \gg \epsilon_d$, $k_{sp} \approx k_{ph}$, where k_{ph} is the photon wavevector in the dielectric. As seen in Figure 20, the assignment of the maxima to SPP excitation and of the minima to Wood-Rayleigh's anomalies

as done in the first studies of EOT in 2D hole arrays was sound but not completely accurate.

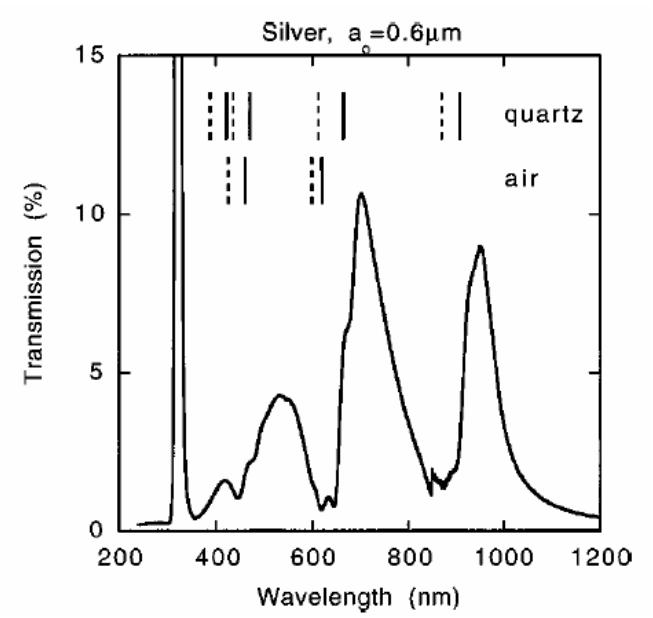

FIG. 20 Zero-order transmission of subwavelength hole array in a Ag film on a quartz substrate for normal incidence; the lattice period is 600nm, the film thickness is 200nm and the diameter of the circular holes is 150nm. The markers indicate positions for the maxima and minima expected for SPP modes on either the silver-quartz or the silver-air interface (solid markers) and the Wood-Rayleigh's anomalies associated with the same interfaces (dashed markers). Figure taken from (Ghaemi *et al.*, 1998).

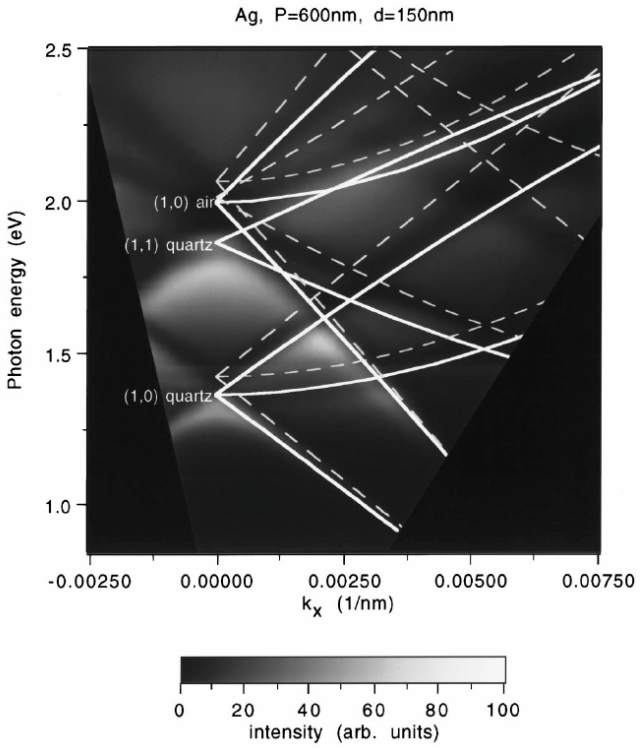

FIG. 21 Measured and predicted dispersion of the extraordinary transmission through a subwavelength hole array. The transmitted intensity is given by a grey scale. The loci of the maxima (drawn lines) and the minima ascribed to the Wood-Rayleigh's anomaly (dashed lines) are superimposed on the measured data. Figure taken from (Ghaemi *et al.*, 1998).

The resonance condition directly implies a relation between the angle of incidence and/or the angle of the transmitted light and the position of the minima and maxima. Figure 21 depicts the transmission through an array as a function of the angle of incidence (Ghaemi *et al.*, 1998). In the experiment, the tilt angle of the sample was varied with respect to the optical axis. Simple goniometry suffices to convert tilt angle and wavelength to an in-plane wavevector. It is clear that both minima and maxima exhibit dispersion. The dashed and drawn lines indicate a reasonable agreement between measurements and the expected values based on the above-mentioned assignment scheme.

This was the physical picture provided by the group that discovered EOT phenomenon in their first two papers published in 1998. Here we summarize the subsequent developments in the search for a better understanding of the EOT phenomenon. After that, we shall present a more detailed view based on the modal expansion method that we are using throughout this review. The first theoretical calculations were performed with the RCWM method (Popov *et al.*, 2000). This group concluded that the EM fields within a hole drilled in a metal film decay much more slowly when the holes are forming a 2D array than what could be expected from estimations based on the hole size. In keeping with the first experimental results, the calculated EOT features closely matched to re-mapping of SPP bands within the light cone. However, the existence of EOT in holey PEC films (Martin-Moreno *et al.*, 2001) showed that the presence of waveguide modes with "modified" propagation constants is not essential for observing EOT. In this last reference, EOT features were explained in terms of the admittances (inverse of impedances) of waveguide modes and an effective admittance of the semi-infinite media close to the surface. When the effective admittance diverges, the incident field does not see the holes and, correspondingly, the transmittance vanishes. At frequencies close to this divergence, the effective admittance changes very rapidly and, eventually, it is equal to the admittance of the waveguide modes. This signals the existence of a surface EM mode. The surface EM modes at both sides of the film are coupled through evanescent fields inside the hole, and the resulting coupled resonant modes give rise to transmission maxima. As these surface EM modes appear in metals, they were termed SPPs of the corrugated surface. This may have led to some confusion, given that, as we shall see later, these surface modes can appear even when the un-corrugated structure does not support SPPs.

Therefore, it is clear that there is a close link between each minimum and maximum of transmittance. As mentioned, transmittance minima are related to divergencies of the effective admittance, which arise due to constructive re-illumination of a hole by all the other holes in the array (Bravo-Abad *et al.*, 2004a; De Abajo, 2007; De Abajo *et al.*, 2005; Genet *et al.*, 2005). Actually, the effective admittance only diverges in a lossless metal, but reaches very high values for the case of good metals as gold or silver. With this caveat in mind, for reasons of economy of language, we shall keep loosely referring to these high values as divergencies. The spectral position of these divergencies has created considerable confusion in the field. This is so because if the metal is treated as a PEC (which can not support SPPs) the divergence of the effective admittance occurs at the wavelengths for which the diffraction orders become tangent to the surface (the so-called Wood-Raleigh's wavelengths). Yet, if the real dielectric constant of the metal is taken into account, the divergencies occur at the wavelengths at which the SPPs *of the flat metal interface* are supported, as it has been discussed in section III.A.2. The original analysis based on the modal expansion stated that the relevant surface EM modes were those of the *corrugated* metal surfaces (Martin-Moreno *et al.*, 2001). This latter view was posteriorly confirmed by rigorous calculations (Lalanne *et al.*, 2005b), which also found a close correspondence between transmission maxima and the excitation of coupled surface EM modes of the holey slab.

This resonant process is optimal when, for a given angle of incidence, the surface EM modes of both surfaces occur at the same frequency, which makes the symmetric environment the most favorable for EOT (Krishnan *et al.*, 2001). In Figure 22(a), we render experimental transmission spectra (Krishnan *et al.*, 2001) that give support to the previous conclusion that the transmittance at resonance is optimal for symmetric situations. An additional property associated to the excitation of these coupled surface EM modes is that the corresponding EM fields are greatly enhanced at the surface (Salomon *et al.*, 2001), as we shall discuss in section III.B.5. The lower three panels of Fig.22 present calculations illustrating the large increase of E-field intensities at the metal-dielectric interfaces that accompany EOT resonances.

The view that EOT in 2D hole arrays is due to coupled surface EM modes has been criticized by Lezec and Thio (2004). The criticism was based on the presence of transmission features in holey *dielectrics*, on the re-examination of EOT enhancements in metals and on the interpretation of these results in terms of what was termed Composite Diffraction Evanescent Wave (CDEW) model. Here we shall focus on the experimental part of Lezec and Thio (2004), as the CDEW model has been shown (Garcia-Vidal *et al.*, 2006b; Lalanne and Hogonin, 2006) to be incorrect (it mishandles polarization and neglects important contributions of the diffracted field). Lezec and Thio correctly pointed out

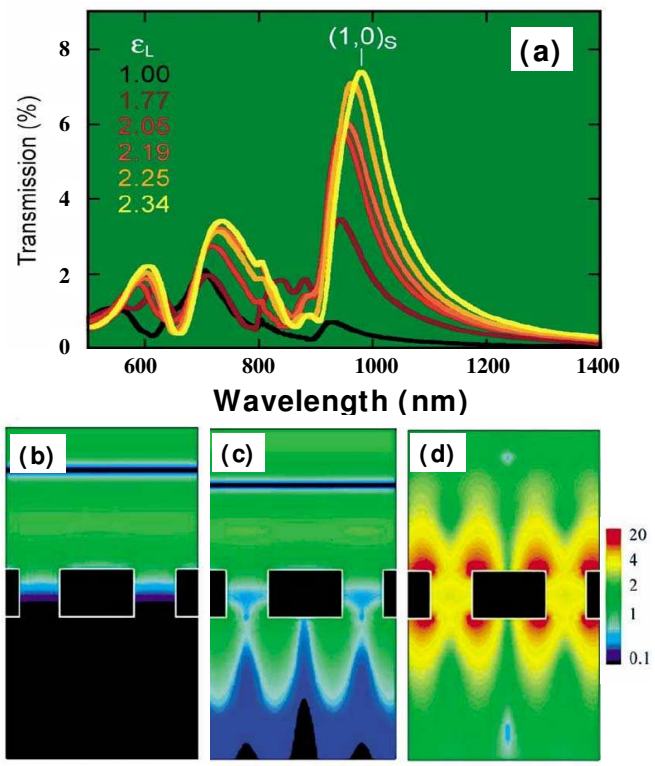

FIG. 22 (a) Experimental zero-order transmittance of a gold film on a quartz substrate ($\epsilon_s = 2.31$) as a function of the dielectric constant of the superstrate, ϵ_L. The film thickness is 250nm, the hole diameter is 200nm and the period of the square array is 600nm. (b), (c) and (d) present calculated cross-sectional views of the electric field amplitudes with various states of resonance: (b) off-resonance in the asymmetric situation (transmission 0.005%), (c) on-resonance in the asymmetric situation (transmission 0.5%) and (d) on-resonance in the symmetric situation (transmission 20%). In the three cases, light is impinging from the top and the E-field amplitude is normalized to the amplitude of the incident plane wave using a logarithmic color scale. Figure taken from (Krishnan *et al.*, 2001).

that the enhancement of the optical transmission per hole in arrays is better obtained from the comparison with the transmission through isolated holes. Their experiments, performed in arrays of 9×9 holes, obtained maximum per-hole transmission enhancement of about 7. This value was about ten times larger than in hole arrays drilled in absorbing dielectrics (like W or amorphous Si). As these media do not present tightly bound EM surface modes, the cited authors concluded that surface EM modes are not responsible for the optical enhancements. However, posterior detailed studies have shown that the difference between holey metal and dielectrics is much greater [see for instance (Przybilla *et al.*, 2006a)] and that the per-hole transmission enhancement in holey metals is virtually unlimited for larger arrays (see (Przybilla *et al.*, 2008) and section III.B.6 of this review paper). Surface EM modes also account for another dif-

ference in the optical transmission through hole arrays in absorbing dielectrics and metals: the peak visibility (defined as the difference between the peak maximum and peak minimum divided by their sum) in holey absorbing dielectrics is much smaller than in holey metals.

A possible origin of the criticism on the relevance of coupled surface EM modes on EOT be the previously cited incorrect association of the relevant surface EM modes to those of an *un-corrugated* surface. For instance, the appearance of EOT when the metal is considered as a PEC has also lead to some doubts on the relevance of coupled surface EM modes. However, as explained before, *periodically corrugated* PEC surfaces do support surface EM modes which, in a perforated film, assist the transmission process (Pendry *et al.*, 2004). The link between EOT in real metals and in perfect conductors was more evident after finding that the structured PEC surface could be approximately represented by effective permeabilities which spoof those of a Drude-like metal (Garcia-Vidal *et al.*, 2005a; Pendry *et al.*, 2004). The emergence of these surface modes in holey slabs is a complex phenomena, as it involves the multiple scattering of the EM fields, between both surfaces and between holes at the same surface. The coupling between holes is thorough combinations of diffraction modes (weighted by the density of states of these modes at the surface) and presents different regimes as a function of both the interhole distance and type of metal considered. At small distances (smaller than a wavelength), the coupling is similar to what it would be in a PEC. At larger distances, coupling through SPP take over (López-Tejeira *et al.*, 2005; Sondergaard and Bozhevolnyi, 2004). Very recently, the details of the formation of transmission EM resonances in periodic arrays from the microscopic expressions of the interhole coupling has been successfully addressed (Liu and Lalanne, 2008). Additionally, the cited microscopic calculation sheds light on the relevance on EOT of the different channels (radiative fields, evanescent fields, SPPs...) that transfer EM fields between holes, both for PEC and real metals at optical frequencies.

To summarize, the physics of EOT in 2D hole arrays is that of two surface EM modes weakly coupled between themselves and weakly coupled to a continuum. This idea is useful to direct the search of EOT to other ranges of the EM spectrum, to other types of materials presenting surface EM modes (like polar semiconductors with surface phonon polaritons) and even to other types of waves. It is also useful because it allows for a phenomenological description of the (sometimes very asymmetric) lines shapes of transmission resonances in terms of the Fano model (Fano, 1961). Here we reproduce the argument [borrowed from the theory of reflection gratings (Neviere, 1980)] given by Enoch *et al.* (2002) and Sarrazin *et al.* (2003). The scattering matrix is dominated by divergencies (simple poles) that occur when the incident field excites a resonance in the system, in this case a surface EM mode. These resonances are leaky, as they couple to radiative modes. This means that the poles appear at complex frequencies or, alternatively, at complex wavelengths. Let us focus first in the case in which one of these poles (characterized by a complex wavelength λ_{pole}) dominates a given region of the spectrum. Now imagine that we consider systems with smaller and smaller holes. Obviously, when the holes are not present, the diffraction coupling to the surface EM mode would vanish and the resonance in the scattering matrix must disappear. Analytical continuity implies that there must be a *zero* in the scattering matrix (characterized by a complex wavelength, λ_{zero}) which, in the limit of vanishing hole size coincides with the spectral position of the pole. Therefore, close to resonance, the transmittance must be of the form

$$T(\lambda) = T_{bg}\,\frac{|\lambda-\lambda_{zero}|^2}{|\lambda-\lambda_{pole}|^2} \tag{27}$$

where T_{bg} represents the background (non-resonant) contribution.

An alternative derivation (Genet *et al.*, 2003) closely followed the original one by Fano (Fano, 1961). The final expression coincides with Eq.(27), but it is written in a form that further clarifies the physical meaning of the different quantities involved:

$$T(\lambda) = T_{bg}\,\frac{(\epsilon+q)^2}{(1+\epsilon)^2} \tag{28}$$

with

$$\epsilon = \frac{\omega-(\omega_{SM}+\Delta)}{\Gamma/2} \quad q=\frac{2\delta}{\Gamma} \tag{29}$$

where ω_{SM} is the frequency of the unperturbed surface EM mode involved in the process, δ is the ratio between the transition amplitudes of the incident wave into the resonant state and the direct (background) channel, and Δ and Γ are the frequency width and the frequency shift of the resonant state due to coupling to the continuum, respectively.

A generalization to the case in which several surface modes contribute appreciably to the transmission in a given spectral window was given by Chang *et al.* (2005):

$$T(\lambda)-T_{bg} = T_a\,\frac{(1+\sum_r q_r/\epsilon_r)^2}{(1+\sum_r \epsilon_r^{-1})^2} \tag{30}$$

where T_a is a parameter reflecting the strength of the resonant process and q_r and ϵ_r are trivial extensions of the expressions for q and ϵ given above, for the r-th surface mode this time.

The resonant nature of the EOT phenomenon has been also confirmed by different experimental studies. By comparing results of the transmitted, reflected and absorbed power associated with the EOT process in 2D hole arrays perforated in suspended Ag films, Barnes *et al.* (2004) were able to conclude that SPP modes act to enhance the EM fields at the metal surface, thus providing a way to increase the transmittance through the subwavelength holes.

Notice that, despite of the apparent geometrical simplicity of an infinite periodic array of apertures in a metal film, the system is still characterized by a large number of geometrical and material parameters. This in turn, leads to the existence of different transmission regimes and the possible coexistence of several mechanisms. In keeping with previous sections, the discussion will be first focused on a simplified model in which the metal film is treated as a PEC. This simplified model shows the main physics and provides a framework for understanding the results obtained within more accurate numerical frameworks. Results obtained within this approximation are applicable to different frequency regimes, by simply scaling all lengths defining the problem by a common factor. The deviations from these results in the optical regime (caused by a finite dielectric function in the metal) will be discussed later on. Calculations will be performed by using the theoretical formalism presented in section I.B. The case of square holes will be considered because all quantities in the formalism have simple analytical expressions for this geometry. Figure 23 shows a schematic picture of the structure under study: a periodic square array of period d of square holes of side a perforated on a free-standing metal film of thickness h.

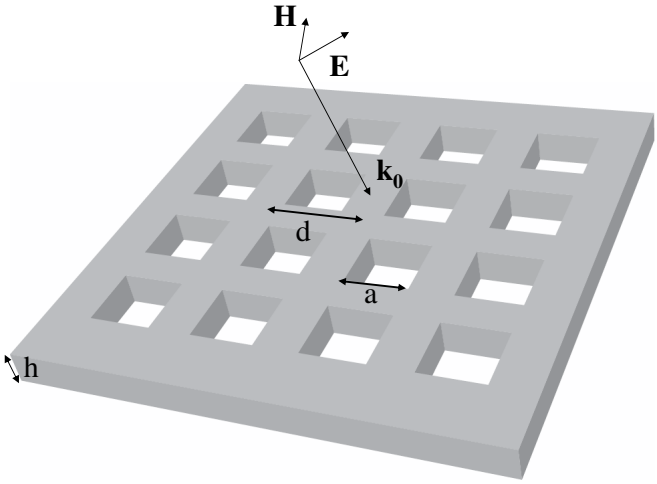

FIG. 23 Schematic picture of a 2D hole array of square holes of side a forming a square array of period d perforated on a metallic film of thickness h. The incident EM-field is a p-polarized plane wave.

Figure 24 renders the normal incidence transmittance spectra for a square lattice of holes in a PEC film of thickness $h = 0.2d$. The holes have square cross section, with side $a = 0.4d$. The cutoff wavelength for the fundamental waveguide mode in the hole is $\lambda_C = 2a$ so, for $\lambda > 0.8d$ all the waveguide modes within the hole are evanescent. The black curve in Fig. 24 is the full multi-mode result, obtained using the method described in section I.B. The red line in Fig. 24 renders the transmission spectra computed within the single mode approximation (SMA) [set of Eqs.(3)], in which only the TE_{01} waveguide mode is considered in the modal expansion within each hole. The magnitudes appearing in Eqs.(3) are now: $\Sigma = \cot(q_z h)$ and $G^V = 1/\sin(q_z h)$, being the propagation constant of the TE_{01} mode, $q_z = \sqrt{k_\omega^2 - (\pi/a)^2}$. Let us recall that the illumination term, I, is basically the overlap integral between the incident plane wave ($\vec{k}_0\sigma_0$) and the TE_{01} mode: $I \equiv 2iY_{\vec{k}_0\sigma_0} < \vec{k}_0\sigma_0|\mathrm{TE}_{01} >$. The EM coupling between holes forming the array is accounted for the propagator G that can be expressed as a sum over both diffracted modes and the two polarizations (s and p): $G = \sum_{\vec{k}\sigma} Y_{\vec{k}\sigma} |\langle \mathrm{TE}_{01}|\vec{k}\sigma\rangle|^2$ where $\vec{k} = \vec{k}_0 + \vec{k}_R$.

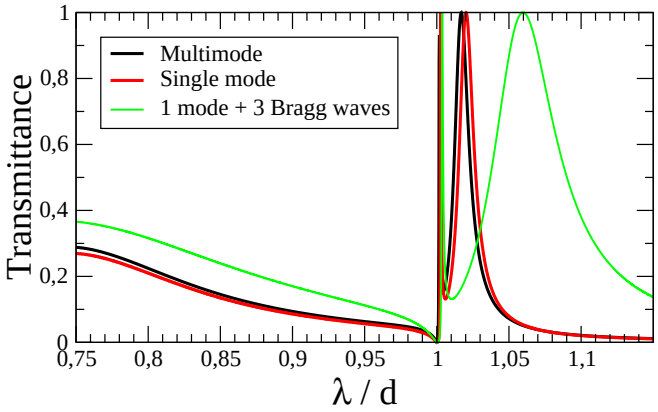

FIG. 24 Transmittance through a hole array drilled in a perfect electrical conductor. The side of the hole is $a = 0.4d$ and the film thickness $h = 0.2d$. The black curve is the result from the converged multi-mode expansion. The red curve is for the single mode expansion discussed in this work. The green curve corresponds to the minimal model described by Martin-Moreno *et al.* (2001).

When evaluating the results for the red curve in Fig.24, as many diffraction modes were included in the sum defining G as needed for convergence. As Fig. 24 shows, the single mode approximation already provides a very good estimation of the exact transmission curve even when the condition $a/\lambda \ll 1$ is not satisfied (in the considered case $a/\lambda \sim 0.3 - 0.5$). The good agreement between the SMA and the exact results stems from the properties of the coupling between the relevant diffraction orders and the waveguide modes: the coupling with the fundamental waveguide mode is stronger, as this mode presents the slower spatial variation. This mechanism takes precedence over the faster decay of higher order waveguide modes inside the hole, thus explaining why the SMA is still a good approximation even for relatively thin films (standard EOT studies in the optical regime are usually done for $h/d \approx 0.3 - 0.5$). The green curve in Fig. 24 was also computed within the SMA, but considering only the terms with p-polarization and reciprocal lattice vectors $\vec{k}_R = 0, \pm 2\pi/d\,\vec{u}_x$ in the sum defining G [this is the so-called *minimal model* as described by Martin-Moreno *et al.* (2001)]. While clearly the consideration of additional diffraction modes modify

the final numerical result, the basics of EOT are already present in this extremely simplified model.

Three features are readily visible in Fig. 24: one very deep minimum at $\lambda = d$ and two transmission peaks. We shall discuss later on that the presence of two peaks is associated with the EM coupling via the holes between the two interfaces of the holey metal film. The deep minimum is related to a divergence of G. Recall that G diverges whenever a p-polarized diffraction mode has $k_z = 0$, as the admittance of a p-polarized plane waves is defined as $Y_{\vec{k}p} = k_\omega/k_z$. In this case, Eqs.(4) give $E = E' = 0$, so there is no transmission because no field penetrates into the holes. Let us consider first the particular case of normal incidence. Then the diffraction order characterized by the reciprocal lattice vector $\vec{k}_R$ has $k_z = 0$ for $|\vec{k}_R| = k_\omega$. Therefore, for a square lattice and treating the metal as a PEC, transmission minima occur at $\lambda^{min}_{n,m} = d/\sqrt{n^2+m^2}$, where n and m are integers. So, the largest wavelength at which a deep minimum occurs is $\lambda^{min}_{\pm1,0} = \lambda^{min}_{0,\pm1} = d$. For the general case of incidence at an angle θ, the condition of grazing diffraction occurs at $|\,k_\omega \sin\theta\,\vec{i} + \vec{k}_R| = k_\omega$. Therefore, at $\theta \neq 0$, the minima associated to $\lambda^{min}_{\pm1,0}$ split, appearing now at $\lambda^{min}_{\pm1,0} = (1 \pm \sin\theta)d$ and $\lambda^{min}_{0,\pm1} = \sqrt{1-\sin^2\theta}\,d$. Figure 25 shows such splitting between transmission minima, for a hole array with the same geometrical parameters as in Fig.24 , but illuminated with a p-polarized plane wave impinging at $\theta = 5$ degrees: the expected minima are clearly seen at wavelengths $\lambda^{min}_{-1,0} = 0.913d$, $\lambda^{min}_{0,\pm1} = 0.996d$ and $\lambda^{min}_{1,0} = 1.087d$.

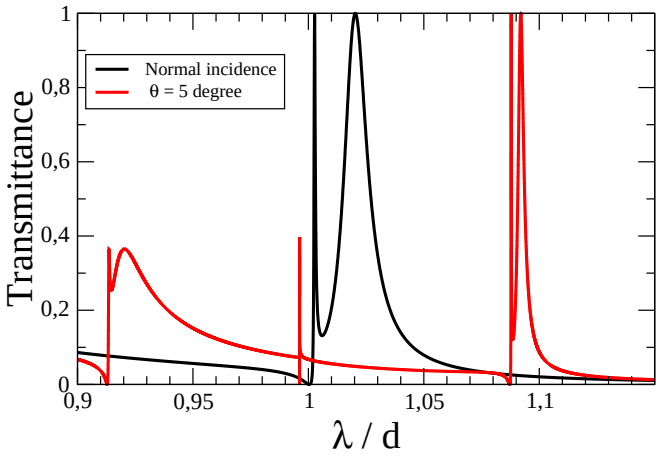

FIG. 25 Transmittance for p-polarized plane wave impinging into a hole array, within the single mode and PEC approximations. The side of the hole is $a = 0.4d$ and the film thickness is $h = 0.2d$. The black curve is for normal incidence, while the red curve is for incidence at 5 degree.

Transmission peaks are due to the presence of leaky surface EM modes of the corrugated metal film. In order to support the previous statement, it is convenient to work within the multiple scattering formalism, as described in section I.B. Within the single mode approximation, the zero-order transmission coefficient can be expressed as a function of two-media scattering coefficients:

$$t_0 = \frac{\tau^{12} e^{iq_z h} \tau^{23}}{1 - e^{2iq_z h}\rho^2} \tag{31}$$

As for the case of slit arrays presented in section III.A.2, the appearance of transmission peaks can be related to resonant properties of ρ, which gives the reflection coefficient for EM-fields coming from the interior of the hole. Fig. 26 renders the real and imaginary parts of ρ, for the cases considered in Fig. 25. Large values for $Im(\rho)$ and anomalous behavior for $Re(\rho)$ occur at spectral positions close to the transmission resonances, both for $\theta = 0°$ and $\theta = 5°$. The spectral dependence of $Re(\rho)$ and $Im(\rho)$ is the one expected, through Kramers-Kronig relations, for causal functions close to localized resonances (Landau *et al.*, 1960) (a reflected field obviously requires a preexisting incident one, so ρ must satisfy causality). Recall that ρ is a two-media scattering coefficient, so its resonances mark the existence of surface EM modes bound to a single interface.

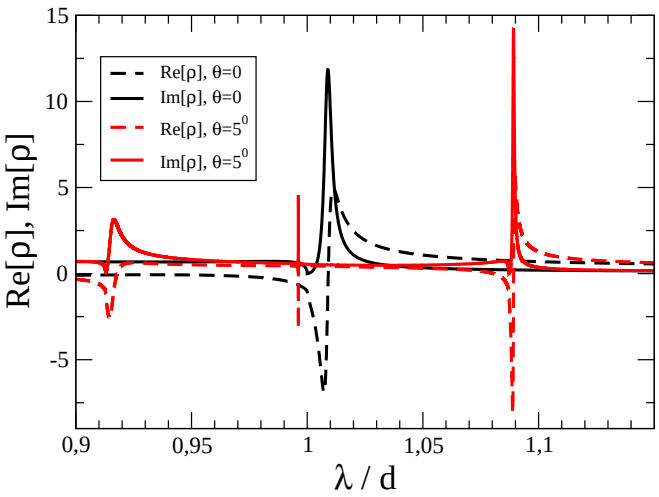

FIG. 26 Real (discontinuous lines) and Imaginary (continuous lines) parts of ρ, the reflection amplitude for a Bloch combination of TE_{01} waveguide modes impinging into vacuum. The Bloch wavevector forms either $0°$ with the normal to the surface (black curve) or $5°$ (red curve). The side of the hole is $a = 0.4d$.

Figure 26 presents spectral regions with $|\rho| > 1$, implying that the reflected field has a larger amplitude than the incident one. This is counter-intuitive, as it seems to wrongly indicate that the reflected current is larger than the incident one. However, for evanescent modes, current conservation only dictates $Im(\rho) > 0$, saying nothing about $|\rho|$. In what follows, we shall show how the existence of a resonant behaviour of ρ is a fingerprint of the emergence of geometrically-induced surface EM modes in a semi-infinite holey PEC film.

In principle, the band structure of these surface EM modes could be obtained by finding the solutions of $G-\Sigma=0$ as a function of the incident wavevector $\vec{k}_0$, as done previously for the case of 1D arrays of slits. Note that, as we are now considering a semi-infinite perforated metal, $G^V = 0$ in Eqs.(3). Complex values of $\vec{k}_0$ must be considered in the search for leaky modes, while truly bound surface modes can only show up for evanescent incident wavefields (with $|\vec{k}_0| > k_\omega$). However, the overall form of the band structure can be obtained without the need of numerical computations. For this, it is convenient to consider that the metal has an arbitrarily large (but not infinite) negative dielectric constant. In this case, a flat metal surface supports truly-bound SPPs. The presence of a periodic array of small holes can be considered within a perturbative approach. The result is that the dispersion relation of surface EM modes in the corrugated structure will closely follow the one for SPPs, except for $\vec{k}_0$ values lying close to a Brillouin Zone boundary, where bands bend in order to accommodate for band gaps. For frequencies above the first band gap, surface modes couple to radiation, thus becoming leaky. However, the band sector below the first band gap still represents a truly bound surface mode. As a result of the band bending caused by the array of holes, the lowest band of surface modes separates from the light line, therefore binding the EM field more strongly to the surface. This line of reasoning has been presented before (Ulrich, 1974), and is at the heart of the whole field of Frequency Selective Surfaces (FSS). Notice that this structure of the dispersion relation is based on general arguments, being applicable not only to SPPs but to any type of waves in periodic media.

However, in the particular case of the EM field in a perforated metal surface, there is an additional mechanism to periodicity-induced binding of the EM fields to the surface. In order to illustrate this point, the bands of a holey metal surface within the PEC approximation can be calculated. Note that PEC flat surfaces do not support truly bound SPPs. In a first approximation, we consider the hole array as a metamaterial and compute the band structure of surface EM modes by matching the *average* EM fields over the surface; the effect of periodicity will be included on a second stage. Matching of average fields can be readily done by using the techniques described in this paper (for instance by computing the resonances in ρ), but neglecting diffraction effects, as done previously for the case of slit arrays (see section III.A.2). Notice that, in this way, all information about the underlying lattice is lost.

Fig. 27 renders the dispersion relation along the $\Gamma - X$ direction for surface EM modes bound to an isolated holey interface, for both $\epsilon_{hole} = 1$ (black curve) and $\epsilon_{hole} = 9$ (red curve). Notice that bands flatten at certain frequencies, *although no diffraction effects have been included yet.* This result can be expressed in a metamaterial language by assigning an effective dielectric constant (ϵ_{eff}) and an effective magnetic permeability (μ_{eff}) to

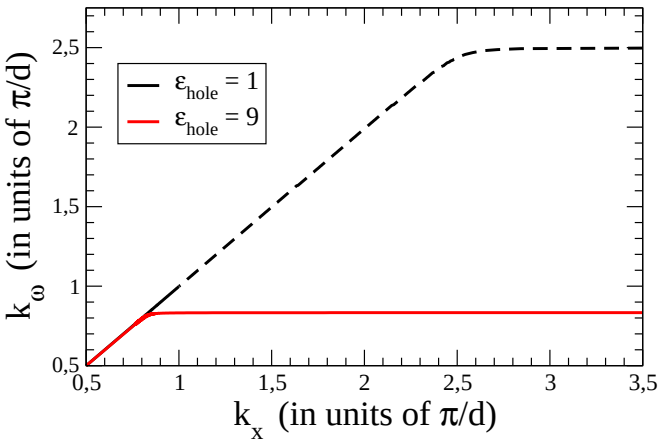

FIG. 27 Dispersion relations for geometrically-induced SPPs in a semi-infinite holey PEC film. The side of the square holes is $a = 0.4d$. A dielectric medium with dielectric constant $\epsilon = 1$ (black curve), or $\epsilon = 9$ (red curve) fills the holes. The discontinuous line marks the spectral region of leaky modes.

the structured surface. This derivation was done by Pendry *et al.* (2004), obtaining $\mu_{eff} = 8a^2/\pi^2 d^2$ and ϵ_{eff} given by:

$$\epsilon_{eff}(\omega) = \frac{\pi^2 d^2 \epsilon_{hole}}{8a^2}\left(1 - \frac{\omega_p^2}{\omega^2}\right) \qquad (32)$$

This functional form for $\epsilon_{eff}(\omega)$ is similar to Drude's expression for the dielectric constant of a metal. Therefore, it can be said that a corrugated PEC surface spoofs a flat surface of a *real* conductor, characterized by a (geometry dependent) "effective plasma frequency" $\omega_p = (c/\sqrt{\epsilon_{hole}})\,\pi/a$, which coincides with the cutoff frequency of the hole. Actually, the system is anisotropic, so care must be taken about the different components of the effective dielectric constant tensor. The anisotropy is also responsible for the fact that the flat region of the dispersion curve for the geometrically-induced SPP appears at $\epsilon_{eff} = 0$, whereas the dispersion relation for truly SPPs bounded to the interface between two *isotropic* media flattens at $\epsilon = -1$.

Periodicity has two effects on the dispersion relation of the geometrically-induced surface EM mode: it opens gaps at wavevectors $\vec{k}$ close to Brillouin zone boundaries and couples bands with $|\vec{k}| > \pi/d$ to radiative modes. This is illustrated in Fig. 27, where the discontinuous lines represent modes that become leaky when diffraction effects are considered. Surface EM modes still appear if higher order waveguide and diffraction modes are included in the calculation, and their dispersion relation still flattens at $\omega = \omega_p$, given by the hole cutoff. However, strong confinement only occurs for frequencies much closer to ω_p than what the effective parameter expression [Eq.(32)] predicts (De Abajo and Saenz, 2005).

Once we have explained the physical origin of the resonant features of ρ, the question is how the geometrically-induced surface EM modes couple in a metal film of fi-

nite thickness and how this coupling affects to the transmission spectrum. The answer to this question is illustrated in Fig. 28, which presents results for an array of square holes with $a = 0.4d$, illuminated at normal incidence. The upper panel shows the transmittance spectra for different metal thicknesses, while the middle panel renders the corresponding spectral dependence for both $e^{|q_z|h}$ (that in the subwavelength regime is always larger than 1 and increases exponentially with h) and $|\rho|$ (that, being a two-media scattering coefficient, does not depend on metal thickness).

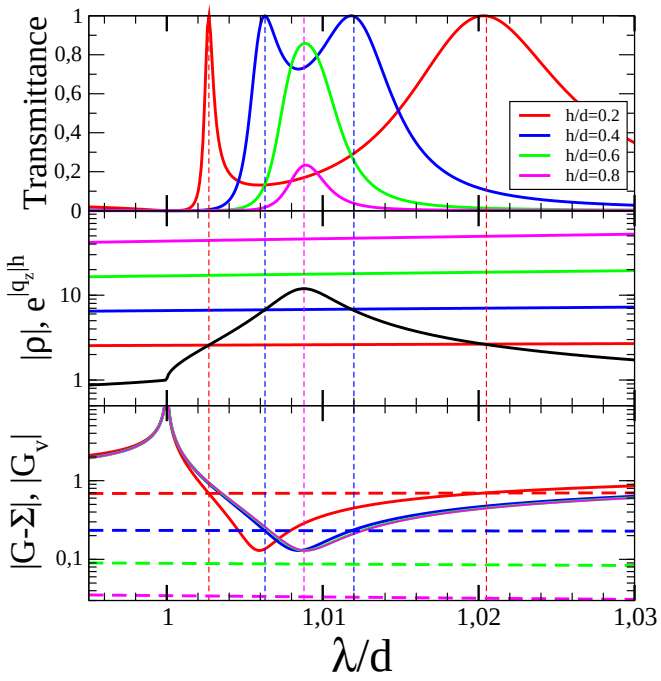

FIG. 28 Upper panel: Normal-incidence transmittance spectra through a hole array in PEC, for different metal thicknesses, h. The side of the holes is fixed at $a = 0.4d$. Middle panel: Spectral dependence of $|\rho|$ (black curve) and $e^{|q_z|h}$ (color lines, for the corresponding metal thicknesses represented in the upper panel). Lower panel: Spectral dependence of $|G - \Sigma|$ (continuous line) and $|G^V|$ (dashed lines). The vertical discontinuous lines are guides to the eye marking the crossings of $|\rho|$ with the different $e^{|q_z|h}$ curves or, alternatively, the cuts between $|G - \Sigma|$ and $|G^V|$.

As Fig. 28 shows, transmittance maxima occur at the wavelengths of minimal distance between the $|\rho|$ and $e^{|q_z|h}$ curves. Depending on the metal thickness, two transmission regimes appear for any given resonance of $|\rho|$. For small metal thicknesses (but still larger than $3-4$ times the skin depth, so the metal is optically opaque and the considered model makes sense), the curves for $|\rho|$ and $e^{|q_z|h}$ cross twice, leading to the presence of two transmission maxima which, for a lossless metal, reach 100% transmission (De Abajo *et al.*, 2005; Martin-Moreno *et al.*, 2001). This is the regime of strong coupling between the two surface EM modes of the two metal-dielectric interfaces: before being radiated, the EM field stays long enough at the surface to be able to build coupled resonances. For thick enough films, $e^{|q_z|h}$ is larger than the maximum value of $|\rho|$. In this case, the curves for $|\rho|$ and $e^{|q_z|h}$ do not cross but there is still one transmission maximum at the wavelength of minimum distance between them, i.e., approximately at the spectral position of the maximum of $|\rho|$. In this situation, the surface EM modes of the two surfaces are weakly coupled: the time that would take to build up the resonance (t_{res}) is smaller than the radiation lifetime (t_{rad}) or, in other words, the EM field does not stay long enough in the system to realize that there are two coupled modes. Conversely to what occurs in the strong coupling regime, transmission maxima in the weak coupling regime decay exponentially with h, even in the absence of absorption. Clearly, whether an EOT peak is at the strong coupling or weak coupling regime strongly depends on both the metal thickness (which controls the time for the resonance build-up) and geometry of the openings (which determines the radiation lifetime). The existence of these two transmission regimes was experimentally confirmed by (Degiron *et al.*, 2002).

The analysis of the existence of coupled leaky modes, and their relation to transmission maxima, can also be done within the formalism involving E and E' (see Eqs.(4)). In this case the resonant condition is expressed as $|G - \Sigma| = |G^V|$, in terms of the determinant of the set of linear equations (3). The lower panel of Fig. 28 renders the spectral dependence of both $|G - \Sigma|$ and $|G^V|$, for the different metal thicknesses considered in the upper and middle panels of the figure. As the figure shows, there is a univocal correspondence between the spectral position of transmission maxima and the wavelengths of minimum distance between $|G - \Sigma|$ and $|G^V|$. Notice that the resonances appear close to the divergences of G, associated with the condition $k_z = 0$ that mark the spectral location of the transmission minima.

The previous analysis was done for an infinite hole array and a lossless PEC film. Going beyond this idealization introduces another two time scales: the typical time the EM fields need for crossing the finite array and the typical time the EM fields can stay in the system before being absorbed. EOT peaks will be largely impaired whenever any of these times is smaller than t_{res}. The effect of a finite dielectric function in the metal, ϵ_M, is illustrated in Fig. 29 which shows the computed transmission spectra for an array of circular holes in a silver film in the optical regime, for a representative set of geometrical parameters. Results obtained with different approximations are rendered in this figure. The finite difference time domain (FDTD) result is obtained by using a small discretization mesh (5nm), and can be considered as virtually exact. Fig. 29 shows that transmittance peaks reaching 100% are still expected for a lossless metal. Also that absorption prevents 100% transmission, having a larger effect on the narrower peaks.

Another feature that is evident if Fig. 29 is that the transmission minimum at λ_{10}^{min} appears red-shifted in a

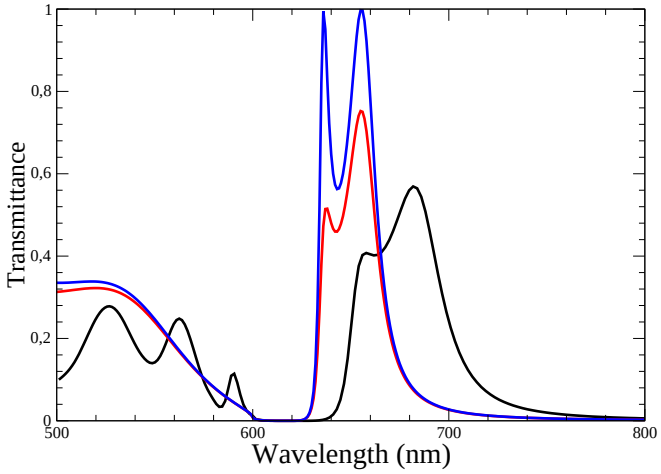

FIG. 29 Transmittance spectra through an array of circular holes in a free-standing silver film of thickness $h = 275$nm. The radius of the hole is $r = 134$nm and the period of the array $d = 600$nm. The dielectric function of silver is taken form Palik's book (Palik, 1985). The black curve is the FDTD result, obtained with a discretization mesh of 5nm. The red curve is the result obtained within the modal expansion and the SIBC approximation. The blue curve is as the last case, but setting the absorption in the metal to zero, i.e. $Im(\epsilon_M) = 0$.

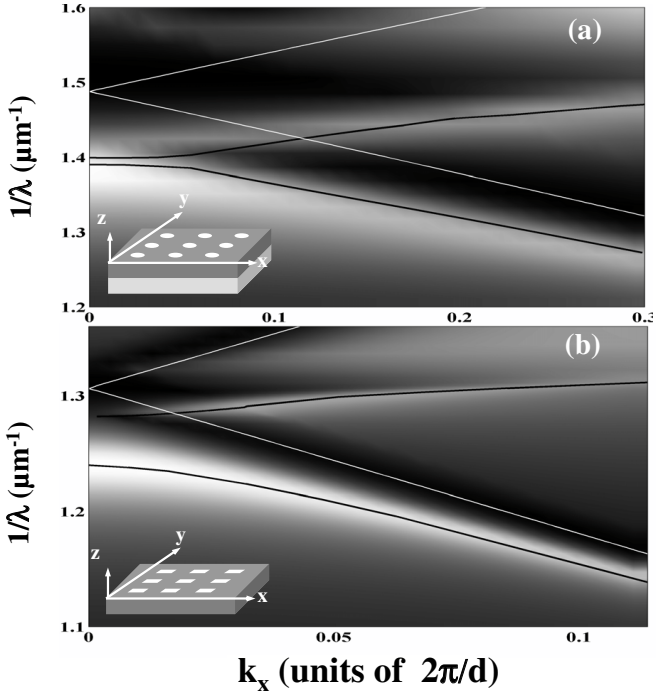

FIG. 30 Grey-scale images show the zero-order transmittance for two holey silver films as a function of the frequency and the in-plane wavevector k_x. (a) Circular hole geometry for a silver film on glass. The scale is linear and the maximum transmittance is 32%. (b) Square-hole geometry for a silver free-standing film. The maximum transmittance is 50% in this case. Superimposed black curves correspond to the SPP dispersion relation of perforated dielectric-silver interfaces, glass-silver perforated by circular holes (a) and air-silver perforated by square holes. The white curves correspond to the SPP dispersion relation for a flat interface, glass-silver for (a) and air-silver for (b). Figure taken from (Lalanne *et al.*, 2005b).

real metal film with respect to the PEC case. This minimum is still due to the divergence of G which, in a real metal, occurs when the corresponding diffraction order has a k_z satisfying $k_z + Z_S k_\omega = 0$. As commented before, this is exactly the condition for the existence of SPPs with parallel momentum, $k_{||} = 2\pi/d$ within the SIBC approximation in an un-corrugated metal surface. Therefore, in general, transmission minima are linked to the dispersion relation of SPPs for the *flat* interface, thus appearing at $\lambda^{min}_{n,m} = d\sqrt{\epsilon_M/(\epsilon_M+1)}/\sqrt{n^2+m^2}$.

This physical picture in which the EOT phenomenon is due to the excitation of surface EM modes has been corroborated by more sophisticated (virtually exact) calculations, able to deal with the dielectric response of metals at optical frequencies (Lalanne *et al.*, 2005b). These authors were able to match the spectral locations of transmission maxima and minima with the ones corresponding to the SPPs supported by the holey metal film, see Fig.30.

3. Dependence on the material properties

The role of the type of metal is important on the extraordinary transmission and has been verified experimentally in several studies. The original observation was made on silver, gold and chromium films at optical frequencies (Ebbesen *et al.*, 1998). In keeping with the previous theoretical discussion, when the imaginary part of the permittivity increases the height of the transmission peaks decrease and their linewidth increase (Chang *et al.*, 2007b; Ctitis *et al.*, 2007; Ekinci *et al.*, 2007; Grupp *et al.*, 2000; Przybilla *et al.*, 2006a; Williams and Coe, 2006).

As predicted by theory (Martin-Moreno *et al.*, 2001), EOT has been also observed for metals at microwave (Beruete *et al.*, 2004b) and THz (Cao and Nahata, 2004a,b; Miyamaru *et al.*, 2003; Qu and Grischkowsky, 2004) frequencies. For EOT in the THz regime, the peak intensity increases as the ratio of the absolute value of the real part of the dielectric constant to the imaginary part increases (Azad *et al.*, 2006).

Interestingly, only a thin layer with a thickness of the order of the skin depth suffices to establish EOT, which was shown by coating thin metal layers on an ordered arrays of microspheres (Farcau and Astilean, 2007; Landstrom *et al.*, 2005). Similarly, a thin layer with a low imaginary permittivity deposited on a more absorbing metal (Grupp *et al.*, 2000) or semiconductor (Fang *et al.*, 2007) is able to greatly influence the transmission. As expected from the SPP dispersion relation, the transmission is also very sensitive to the refractive index of the dielectric material at the metal interface which will affect

both the peak position and the transmission intensity (Krishnan *et al.*, 2001). As a consequence, the presence of even a thin dielectric layer can be detected (Tanaka *et al.*, 2005) and used for sensing purposes (Brolo *et al.*, 2004a) as further discussed in section V.A.

So far, extraordinary transmission has been observed for periodic arrays in a wide variety of materials for various frequencies: highly-doped Si (Gomez-Rivas *et al.*, 2003), metallic-organic conducting polymers (Matsui *et al.*, 2006), VO_2 (Donev *et al.*, 2006), metal-coated VO_2 double layers (Suh *et al.*, 2006), $SrTiO_3$ (Miyamaru *et al.*, 2006b), GaAs (Wasserman *et al.*, 2007), gold-coated GaAs (Zhou *et al.*, 2008), amorphous SiO_2 (Chen *et al.*, 2007b) and SiC (Urzhumov *et al.*, 2007).

Exhaustive studies of the dependence of EOT peaks on the type of metal have been conducted both experimentally (Przybilla *et al.*, 2006a) and theoretically (Rodrigo *et al.*, 2008). Figure 31(a) renders a resume of the evolution of the experimental EOT peak heights for different metals as a function of the resonant wavelength. On the other hand, Fig. 31(b) shows the FDTD calculated transmission spectra for Ag, Al, Ni and W. The main conclusion of these two studies is that the two main parameters that characterize the influence of the dielectric constant of the metal on EOT peaks are the skin depth (which effective enlarges the hole size, increasing the transmittance) and the absorption length (small absorption lengths impair the resonant process). "Good metals" like Au, Ag, and Cu sustain EOT peaks with transmission values that may exceed even those of a PEC with the same geometrical parameters (due to the effective hole enlargement). On the contrary, metals like Ni and Cr present very low EOT peaks due to the large absorption occurring in these metals. The skin depth in Al is much smaller than in any other metal: correspondingly EOT peaks in holey aluminum films resemble those in a PEC, except for the longer wavelengths in the optical regime, when absorption in Al increases and the EOT is more like the corresponding to a "bad metal". The case of W is interesting, as in the optical regime it behaves as a lossy dielectric. Still surface EM modes (known as Zenneck waves) exist in lossy dielectrics, leading to transmission peaks (Sarrazin and Vigneron, 2003). However, transmission peaks in W are much weaker than even those associated with bad metals (see Fig. 31).

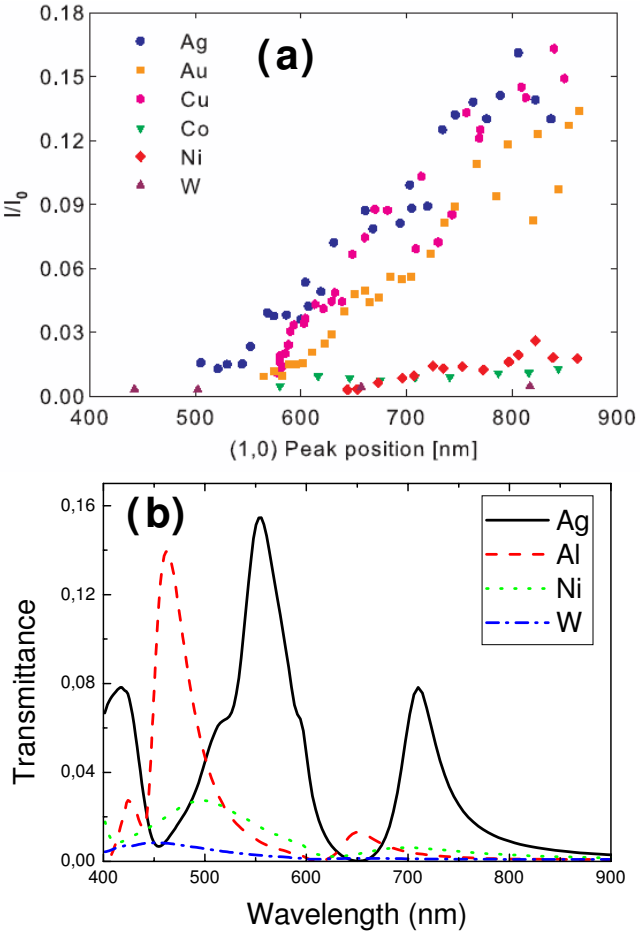

FIG. 31 (a) Experimental transmission intensities as a function of the $(1,0)$ peak position for different metals. The samples consist of perforated metal slabs (thickness 250nm) deposited on a glass substrate. The period of the square arrays is varied between 200nm and 500nm and the ratio between period of the array and diameter of the holes is fixed at 1.75. (b) Calculated transmission spectra for an array of circular holes in a metal film deposited on a glass substrate, for several metals. Calculations were performed with the FDTD method. The geometrical parameters considered are: period $d = 400$nm, metal thickness $h = 250$nm and hole radius diameter $r = 114$nm. Figures taken from (Przybilla *et al.*, 2006a)(a) and (Rodrigo *et al.*, 2008)(b).

4. Size and shape dependence

Already in the first report of EOT the size of the holes was shown to play an important role in the height of the transmission peaks (Ebbesen *et al.*, 1998). This observation has been confirmed in great detail as a function of incident angle for various reciprocal lattice directions (Williams *et al.*, 2004). As the hole diameter is increased, both the transmission intensity and the width of the peaks increase (Ishihara *et al.*, 2005b; Miyamaru *et al.*, 2006a). Clearly, these observations are consistent with a picture in which radiative damping of the SPP modes occurs due to SPP scattering with the holes (Kim *et al.*, 2003; Naweed *et al.*, 2003). When a large range of hole sizes is investigated, it becomes clear that no single power-law scaling can describe the increase of the normalized transmission (van der Molen *et al.*, 2004). Figure 32 presents the dependence on hole size of the normalized transmission for a large range of hole sizes. A huge dependence of the transmitted intensity for small hole sizes can be observed, where the normalized transmission scales as high power of the diameter. At larger hole sizes and for a larger normalized transmission the trend saturates, which is a direct result of the fact that

the absolute transmission has already reached the saturation value of 90%. The existence of two regimes as a function of the hole size can be understood with the help of the theoretical modelling presented in section III.B.2. When the hole size is very small, the factor $e^{|q_z|h}$ is very large as the waveguide mode inside the hole decays very rapidly. Then, the field enhancement coming from the reflection coefficient, $|\rho|$, can not compensate the exponentially small factor (mathematically, there is not cut between $e^{|q_z|h}$ and $|\rho|$), and the transmission is extremely low. As the hole size is increased, $e^{|q_z|h}$ is strongly reduced, leading to the emergence of a cut between $|\rho|$ and $e^{|q_z|h}$, i.e., the transmission reaches its maximum value and saturates.

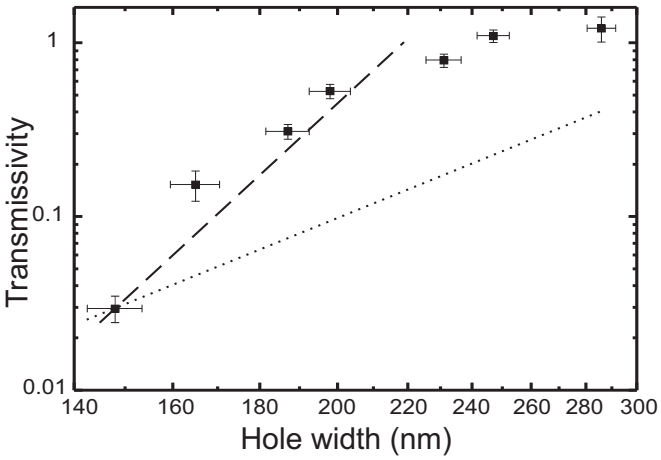

FIG. 32 Measured dependence of the transmission of the (0,1)-peak through an array of square holes as a function of size of the holes (double logarithmic representation). The thickness of the gold films is 200nm and are deposited on a glass substrate. All arrays investigated have a period of 425nm. The dotted line obeys $T \propto d^4$. The dashed line corresponds to $T \propto d^9$. For smaller holes the increase in normalized transmission is easily faster than d^4, while for the larger holes the normalized transmission saturates. Figure taken from (van der Molen *et al.*, 2004).

Hole size also affects the spectral position of the transmission peaks. A small blue shift can be observed for the main peaks as the hole size is decreased (van der Molen *et al.*, 2004; Naweed *et al.*, 2003). In this last reference, it is reported that the main EOT peak shifts by $\Delta\lambda \sim -30$nm as the hole width is decreased from 286nm to 148nm. This can be interpreted within the theoretical modelling presented before as due to the fact that when the hole size is decreased, the spectral location of the SPP in the corrugated surface tends to its corresponding value for a flat metal surface, with no holes. Intriguingly, transmission measurements in the THz regime as a function of hole size exhibit a blue shift with increasing size of the holes (Han *et al.*, 2007). On the other hand, the analysis of the crossover between the EOT regime appearing for small holes and the metal wire mesh limit (when the holes occupy most of the area of the unit cell) have been recently addressed both experimentally and theoretically (Bravo-Abad *et al.*, 2007b).

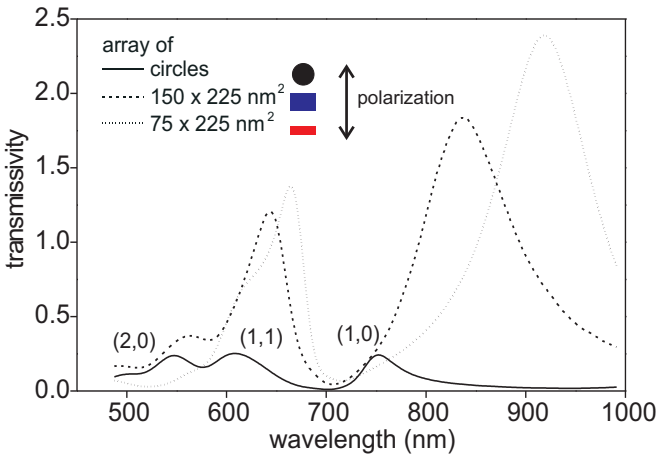

FIG. 33 Measured spectral extraordinary transmission spectra for three different hole shapes: circular (diameter 190nm), rectangular (150×225nm^2; aspect ratio 1.5) and rectangular (75×225nm^2; aspect ratio 3). As the aspect ratio of the holes is increased from 1 to 3, the normalized transmission of the primary peak increases by an order of magnitude. Arguably, more important the peak exhibits a red shift of 170nm. Figure taken from (Koerkamp *et al.*, 2004).

The role of the individual holes in the EOT phenomenon in 2D hole arrays becomes truly important when the shape of the holes is changed from circular to rectangular (Koerkamp *et al.*, 2004). Several key changes occur. First, the normalized transmission is increased by nearly an order of magnitude, even though the actual area per hole decreases (see Fig. 33). This is in agreement with the trend observed in individual rectangular apertures, as described in section II.B.2. Also a strong polarization anisotropy occurs between the best transmitted polarization, i.e., perpendicular to the long axis of the holes, and the polarization along the long axis of the holes. This anisotropy, which causes birefringence is also observed for elliptical hole shapes (Elliott *et al.*, 2004; Gordon *et al.*, 2004), and has been addressed theoretically (Strelniker, 2007). The birefringence exhibits a pronounced wavelength dependence (Elliott *et al.*, 2005), thus opening up a large perspective for polarization control through tuning the aspect ratio of the holes, wavelength and the angle of incidence (Sarrazin and Vigneron, 2004). The same polarization effects have also been observed for the transmission of THz radiation through arrays of rectangular subwavelength holes, even though the thickness of the metal layer, in that case, is only a small fraction of the incident wavelength (Cao and Nahata, 2004a).

But perhaps the most profound change to the transmission spectrum appearing in Fig. 33, is the observation that the primary, $(0,1)$-peak undergoes a huge red shift when hole shape is varied (Koerkamp *et al.*, 2004). A shift as large as 170nm can be observed. In these first

experiments the hole area was not kept constant and, while unlikely, this may have influenced the experiments.

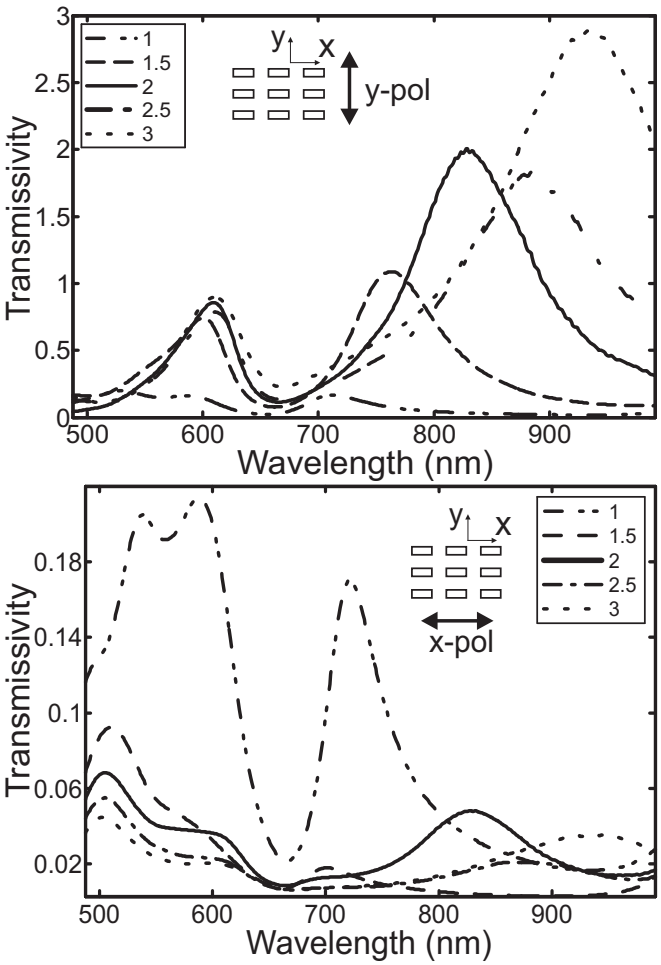

FIG. 34 Measured normalized transmission of nanohole arrays consisting of rectangular holes with varying aspect ratio for two different incident polarizations. The legends show the aspect ratios of the holes. The insets show the relative direction of the polarization with respect to the hole geometry. (a) The normalized transmission exhibits an increase for all peaks. The (0,1)-peak exhibits broadening and a pronounced red shift as the aspect ratio is increased. (b) For the x-polarized light the opposite trend is observed: an increase in aspect ratio results in a decrease in normalized transmission. For the largest aspect ratios a small amount of polarization cross-talk is observed that can be attributed to minute alignment imperfections. Figures taken from (van der Molen *et al.*, 2005).

In an investigation where only the aspect ratio of rectangular holes was varied, a smooth increase of the normalized transmission is observed in addition to a monotonous red shift as a function of aspect ratio (van der Molen *et al.*, 2005) (see Fig. 34). Clearly, for hole arrays with elongated holes the extraordinary transmission is mediated by a combination of localized effects and distributed effects related to the periodicity of the array. The spectral position of the main, $(0,1)$-peak shifts monotonously as the aspect ratio of the holes is increased from aspect ratios where periodicity governs the peak position, i.e., aspect ratio equal to 1, to aspect ratios where localized effects are important. Figure 34 also shows that the polarization anisotropy increases when the aspect ratio of the holes becomes larger. The large polarization anisotropy combined with the peak shifts induced by high aspect ratios can be exploited for practical purposes (see section V.A).

The dependence of the transmittance through periodic hole arrays as a function of the period, for a fixed hole shape, was experimentally studied by Degiron and Ebbesen (2005). The measured transmittance spectra through a suspended Ag film pierced with rectangular holes is rendered in Fig.35, for the two orthogonal polarizations. The different contributions to the transmittance are clearly visible as the period changes. The SPP mode associated with the periodicity dominates the transmittance and the contribution of the localized mode is either blocked or revealed depending on whether it coincides with a minimum or maximum of the SPP mode, respectively. At the same time, the fact that the SPP transmission peaks becomes strongly attenuated above 550nm when the polarization is perpendicular to the short axis of the aperture (see panel (a) in Fig. 35) as compared to being perpendicular to the long axis [Fig. 35(b)], is just due to a drastic shift in the cutoff wavelength of the individual apertures on going from the long to the short axis of the holes. This picture of the evolution and mixing between the transmission resonances associated with SPP and localized modes has been theoretically corroborated (Mary *et al.*, 2007).

Measurements show that hole shape also affects the dispersion of the EOT peaks. In particular, the flat region in the dispersion around $k_{\|} = 0$ widens as the aspect ratio is increased (Fig. 36). This indicates that the mechanism responsible for the transmission becomes more localized in real space, which has been confirmed with near-field optical microscopy for rectangular holes with high aspect ratio (Chu *et al.*, 2007).

The role of local effects can be enhanced through other hole shapes. Inspired by the fact that a co-axial cable has no cutoff, a periodic arrangement of annular/coaxial holes was proposed (Baida and Van Labeke, 2002, 2003). However, it was soon realized (Baida *et al.*, 2004) that this propagating mode cannot be excited by a normally incident plane wave and that plays a minor role for oblique incidence and p-polarized light (Baida, 2007). Therefore, the transmission resonances emerging in arrays of annular holes result from the interplay between SPP modes and localized resonances that are spectrally located at the cutoff wavelength of the TE_{11} waveguide mode of the annular aperture (Lomakin *et al.*, 2007; Orbons and Roberts, 2006). These last localized modes are very similar to those previously described for rectangular holes. Through an optimization of parameters, absolute transmissions were predicted up to 90% for arrays with a significant 'opaque' area. It was also predicted

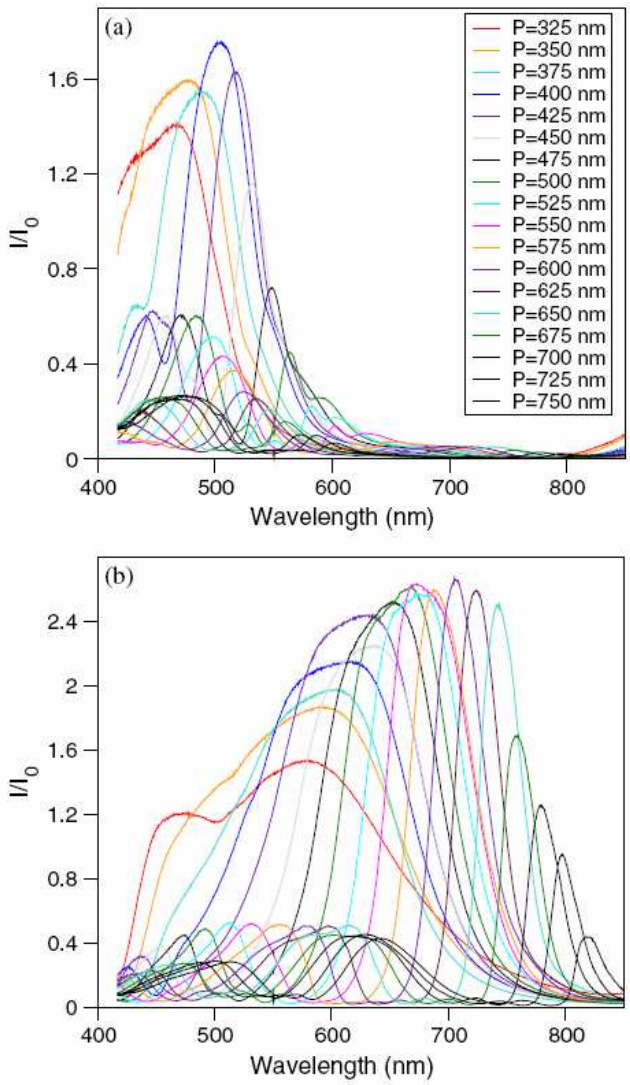

FIG. 35 Transmission spectra of rectangular holes with the lattice constant as a parameter, plotted for the polarization perpendicular to the short edge (a) and perpendicular to the long edge (b). All the samples were fabricated with the same rectangular holes ($260 \times 200\text{nm}^2$ perforated on suspended Ag films of thickness 400nm. Figure taken from (Degiron and Ebbesen, 2005).

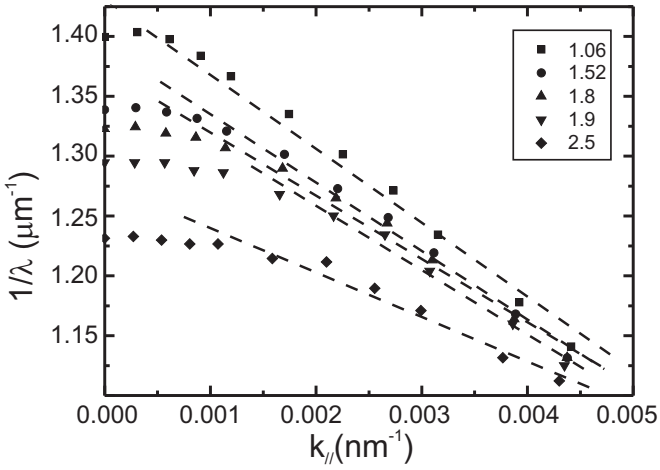

FIG. 36 Measured dispersion of the (0,1)-peak for different aspect ratios. The dispersion changes as the aspect ratio is increased: the fitting lines decrease in slope and the dispersion around $k_\parallel = 0$ becomes flatter for a larger range of $k_\parallel$. This indicates a stronger degree of localization in the transmission process. Figure taken from (van der Molen *et al.*, 2005).

that square coaxial structures would exhibit the same behavior and allow large transmission coefficients (Moreau *et al.*, 2003). The behavior of the annular holes has been alternatively described in terms of coupled cylindrical SPPs on the inner and outer surfaces of the annulus (Haftel *et al.*, 2006).

The theoretical predictions for the annular hole arrays were experimentally verified in the near-infrared. Careful polarization and angle-dependent measurements confirm an interplay between cutoff resonances in the coaxial holes and the delocalized resonances associated with SPPs (Fan *et al.*, 2005c). It was shown that in the mid-infrared the arrays of coaxial holes could transmit up to 5 times more than arrays of circular holes with the same open air fraction (Fan *et al.*, 2005a,b). In the visible range (700nm), a maximum transmission of 17% was achieved (Poujet *et al.*, 2006; Salvi *et al.*, 2005). The normalized transmission through annular hole arrays can be further enhanced by choosing the proper symmetry of the array (Sun *et al.*, 2006b). The role of cylindrical SPPs was experimentally confirmed through experiments in combination with simulations and a consideration of the dispersion of these SPP modes (Orbons *et al.*, 2007). Under certain circumstances and by using the proper cavity resonances in the annular holes, the transmission of annular holes arrays can even become independent of the arrangement of the holes with respect to each other (Rockstuhl *et al.*, 2007).

Periodic subwavelength hole arrays with more exotic hole shapes have also been show to exhibit EOT, such as arrays of diamond-shape holes (Sun *et al.*, 2006a) and triangles (Kim and Moyer, 2006a,b). A range of hole shapes has successfully been explored in order to red-shift the cut off of the individual holes. In particular H-shaped holes (Sun *et al.*, 2007) and cruciform-shaped holes (Chen *et al.*, 2007a; Ye *et al.*, 2007a,b) seem especially useful for this purpose. The use of shape in combination with array symmetry and periodicity provides a highly versatile tool box to fabricate, for example, THz filters (Lee *et al.*, 2006a). Arrays consisting of double holes that slightly overlap provide an additional, localized field enhancement near the resulting cusps (Gordon *et al.*, 2005; Kumar and Gordon, 2006), which can be exploited for enhancing nonlinear phenomena (see below). Recently, evidence has been found that also the structure in the holes perpendicular to the film can influence the transmission. Measurements in the THz regime show that arrays with holes in which the radius first decreases

and then increases to its original value exhibit blue shifts when the radius of the constriction in the holes is reduced (Batulla *et al.*, 2007).

In summary, EOT phenomenon in hole arrays is mediated by both localized effects and distributed effects related to the periodicity of the array. The final spectral shape is dependent on the relative contribution of the cutoff function of the individual apertures, the localized modes and SPP modes and these are all sensitive not only to the lateral dimensions of the aperture but also to factors such as the depth of the apertures and the density of apertures in the metal film.

5. Electric field enhancement and nonlinear effects

Calculations showed that EOT phenomenon is accompanied by highly localized field distributions (Krishnan *et al.*, 2001; Salomon *et al.*, 2001). Near-field experiments were able to confirm these predictions (Hohng *et al.*, 2002) by taking advantage of the subwavelength nature of the EM fields associated with SPP excitation. Interestingly, high field amplitudes between the holes can be found to accompany certain maxima in the far-field transmission. In the near field, different components of the diffraction interfere to set up complex field patterns (Hohng *et al.*, 2005). The exact spatial field distributions are determined by the spatial potential experienced by the Bloch modes (Zayats *et al.*, 2003). The free space wavelength with respect to the periodicity is also an important factor in the field patterns. When the free space wavelength is much smaller than the periodicity of the array, clear standing wave patterns between the holes can be observed (Gao *et al.*, 2006; Hou *et al.*, 2006; Rokitski *et al.*, 2005b). In that case, an amplitude modulation persists away from the interface, whereas for larger wavelengths, as only the zero-order diffracted beam is radiative, a homogeneous pattern is found (Hohng *et al.*, 2005). Even for quasi-periodic hole arrays *hot spots* with a diameter of roughly half the wavelength can be found up to 18 wavelengths away from the structure (Huang *et al.*, 2007b).

On the other hand, these high EM fields that accompany EOT phenomenon can be exploited to enhance nonlinear effects. Second harmonic generation (SHG) can arguably be considered as the most basic nonlinear optical effect. The first observation of enhanced SHG in a subwavelength hole was actually not observed in a hole array but in a bull's eye structure (see section IV) in which the subwavelength hole was surrounded by a set of concentric grooves (Nahata *et al.*, 2003). An enhancement of 10^4 was found with respect to the second harmonic yield obtained from a single hole without grooves. The first observation of SHG in a hole array has found a maximum yield for those incidence angles where the fundamental beam is maximally transmitted (Airola *et al.*, 2005). A fivefold enhancement of the second harmonic yield with respect to the yield of disordered arrays was found. By breaking the centro-symmetry of the individual holes the yield was further increased.

The second harmonic yield can also be increased by changing the hole shape while retaining the centro-symmetric nature of both the holes and the array, for example by using rectangular holes. In first instance this is not surprising: as the aspect ratio is varied, the linear transmission through the arrays is influenced. The nonlinear response may be expected to mimic the change in the linear response, albeit in a nonlinear fashion depending on the order of the nonlinear process being considered. Figure 37 presents both the linear transmission of the fundamental beam as the second harmonic yield behind the array as a function of the aspect ratio of the holes. For aspect ratios ranging from 0.36 to 1.6 an increase in the linear transmission by a factor of 60 is observed . At the same time the second harmonic yield is found to increase by a factor 4000.

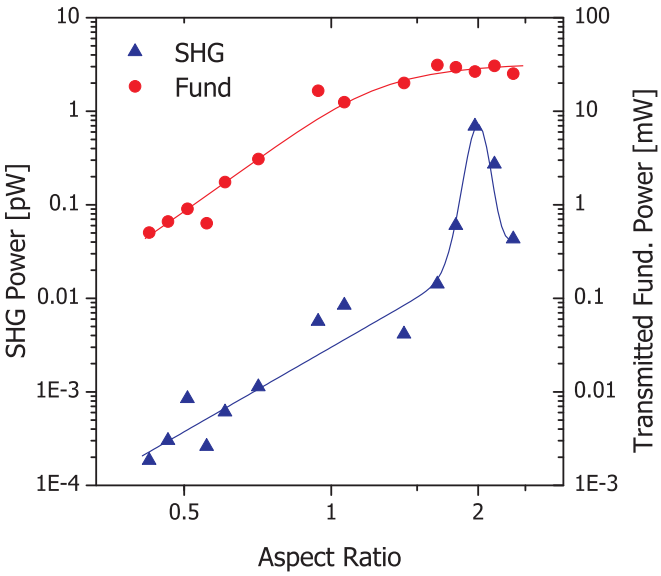

FIG. 37 Double logarithmic plot of transmission of the fundamental beam at 830nm (right axis, red dots) and the collected second harmonic signal (left axis, blue triangles) as a function of aspect ratio. The transmission of the fundamental beam exhibits a monotonic increase before levelling of at an aspect ratio of 1.6. The second harmonic shows an steady increase of slightly less than two orders of magnitude up to an aspect ratio of 1.6. Between aspect ratios of 1.6 and 2.3 a peak is observed in the second harmonic with a magnitude of a factor 50. The lines are guides to the eye. Figure taken from (van Nieuwstadt *et al.*, 2006).

However, a closer look at Fig. 37 shows that for aspect ratios ranging from 1.6 to 2.8, the transmission of the fundamental beam does not exhibit any increase. Nevertheless, the second harmonic yield is found to exhibit an additional increase of a factor 50, before showing a decrease. In order to put this observation in perspective, it is useful to derive the effective nonlinear susceptibility of the structure. By considering the array as an effective homogeneous medium, the nonlinear susceptibility can

be calculated from the second harmonic yield and all relevant linear transmission coefficients (Sutherland, 1996). Figure 38 shows the nonlinear susceptibility of the hole arrays as a function of the aspect ratio of the holes. For aspect ratios ranging from 0.36 to 1.6 it can be seen that the nonlinear susceptibility exhibits no clear trend as a function of aspect ratio. For the aspect ratios 1.6 to 2.8 a clear peak in the nonlinear susceptibility is found. An increase of the susceptibility of a factor of roughly ten is observed (van Nieuwstadt *et al.*, 2006). In other words, a "hot" hole shape is observed for aspect ratios around 2. This "hot" hole shape can be explained by the fact that for these aspect ratios the cutoff condition of the individual holes is met for the fundamental beam and, as explained in section II.B.2 when discussing the cutoff resonances appearing in single rectangular holes, a huge EM field enhancement is associated with the excitation of this resonance. The resulting slow light propagation through the holes close to cutoff will lead to an enhanced nonlinear response.

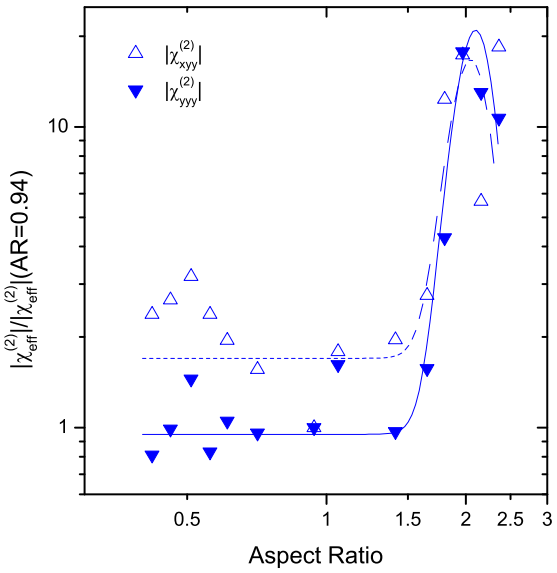

FIG. 38 Double logarithmic plot of two components of the effective second order nonlinear susceptibility versus aspect ratio. Between aspect ratios 0.36 and 2.8 no clear trend is observable in the effective nonlinear susceptibility. Between aspect ratios 1.6 and 2.8 a peak in the effective susceptibility of a factor more than one order of magnitude occurs. Figure taken from (van Nieuwstadt *et al.*, 2006).

The field enhancement in coaxial hole arrays has been exploited to generate second harmonic with very high efficiency. It has been demonstrated that second harmonic generation from GaAs, which is introduced in the gaps of a coaxial hole array, can be as efficient as SHG from z-cut $LiNbO_3$ (Fan *et al.*, 2006a). It turns out that the field enhancement inside circular hole arrays is also sufficient to generate a good second harmonic yield when GaAs is introduced in the holes (Fan *et al.*, 2006b). The SHG in circular hole arrays, without GaAs, can be enhanced through the use of double hole geometries in which two overlapping holes lead to a sharp ridge between the holes that induces a high local enhancement. The SHG efficiency can be boosted by a factor of 14 with respect to circular holes (Lesuffleur *et al.*, 2007b). The SHG process can be improved by tuning a linear transmission resonance to the second harmonic wavelength through a proper change in array periodicity or incidence angle for a wide range of hole and array symmetries (Xu *et al.*, 2007).

So far only a limited number of investigations have used hole arrays to boost third order nonlinear processes, rather than the second order process of SHG. By exploiting Kerr nonlinearity it is possible to time-gate one beam of photons being transmitted through a circular hole array with a second beam (Smolyaninov *et al.*, 2002). The change in polarization of the beam that was switched shows that the enhanced fields inside the holes are crucial for an efficient switching. The Kerr nonlinearity can lead to bistability in the extraordinary transmission as shown theoretically and experimentally by Porto *et al.* (2004) and Wurtz *et al.* (2006). In this case the high intensity of a control laser induces changes of the local index of refraction. This leads to a modification in the transmission which persists when the intensity is subsequently reduced, resulting in a characteristic hysteresis loop in the transmission as a function of the intensity of the control field. Two-dimensional FDTD calculations of subwavelength gratings have identified the layer thickness of the Kerr medium and the size of the apertures as crucial parameters for maximizing the bistability (Min *et al.*, 2007).

6. Finite size effects

The question on the dependence of EOT efficiency with the number of apertures has also been also addressed from both the experimental and theoretical points of view. As EOT results from the collective response of the array, the resonant transmittance should increase as the number of holes forming the array increases. Indeed, experimental measurements in the infrared (Thio *et al.*, 1999), in the THz regime (Miyamaru and Hangyo, 2004) and in the visible range of the EM spectrum (Henzie *et al.*, 2007) have confirmed this expectation. More recently, Przybilla *et al.* (2008) have presented a study on how the transmission per hole reaches saturation with the number of holes. They found, both experimental and theoretically, that the number of holes needed for saturation depends very strongly on the size of the holes: the larger the hole diameter, the faster a transmission saturation is reached. As seen in Figure 39, for holes with diameter $r = 134$nm, this saturation is reached between $21\times21(441)$ and $31\times31(961)$ holes. This saturation value

is marked by the propagation length of the SPP which is mainly controlled by the size of the hole.

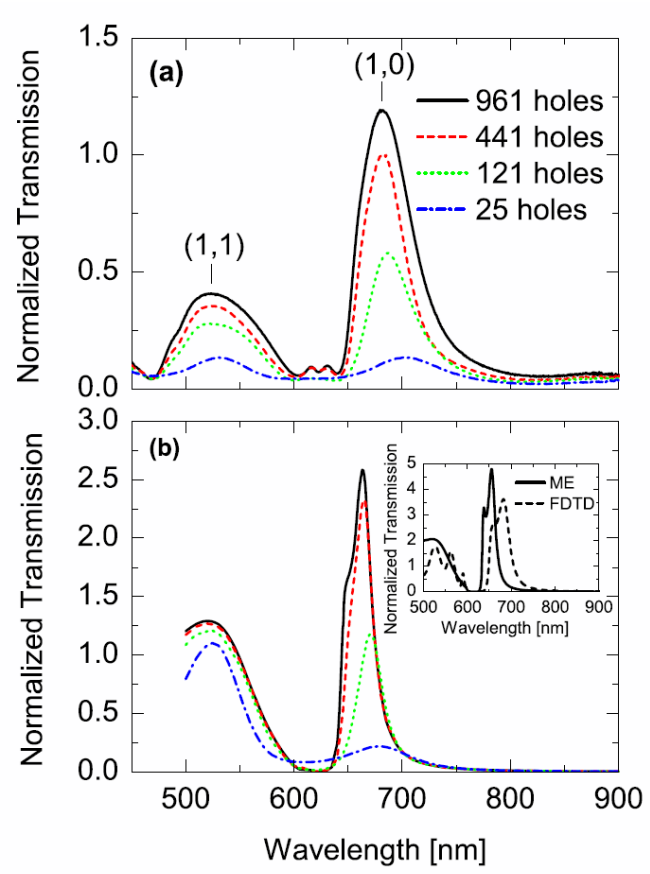

FIG. 39 (a) Experimental transmission spectra for 2D square arrays containing 5×5, 11×11, 21×21 and 31×31 circular holes. The arrays were milled in thick 275nm free-standing silver films with a period $d = 600$nm and a hole radius $r = 134$nm. Transmissions are normalized to the hole area. (b) Normalized-to-area transmission spectra obtained from the modal expansion formalism explained in section I.B in which the SIBC have applied. The geometrical parameters are the same as in the experiments. Inset: comparison between the modal expansion and FDTD results for a infinite square arrays. Figure taken from (Przybilla *et al.*, 2008).

Przybilla *et al.* (2008) also analyzed the value of the EOT transmittance in large arrays, and compared it to the transmittance through a single hole. The experimental results showed that the enhancement in the transmittance per hole in arrays is larger for the smaller holes: this enhancement is around 40 for holes with diameter 150nm in 40×40 arrays (see Fig. 40). Theoretically, it was computed that this value would be 100, and much larger values are obtained for smaller holes and larger array sizes. In contrast to some claims that the maximum transmission efficiency in EOT is around 7 (Lezec and Thio, 2004), no theoretical fundamental upper limit exists to the possible enhancement attainable in the EOT phenomenon (within the macroscopic Maxwell equations).

Finite size effects have been also theoretically analyzed in 1D arrays of holes and slits. For the case of holes, it was found that a chain of subwavelength holes can be considered as the basic geometrical unit showing EOT. A 2D hole array can be seen as a collection of weakly EM coupled 1D chains of holes, these chains oriented in the direction of the in-plane component of the E-field (Bravo-Abad *et al.*, 2004a). Regarding slits, the ratio between the width of the slits and period of the array is the main parameter controlling how the saturation is reached for the resonant transmission associated with surface modes (Fernandez-Dominguez *et al.*, 2007). As expected, the other channel for transmission, linked to the excitation of a slit-cavity resonance, does not depend strongly on the number of slits in the array.

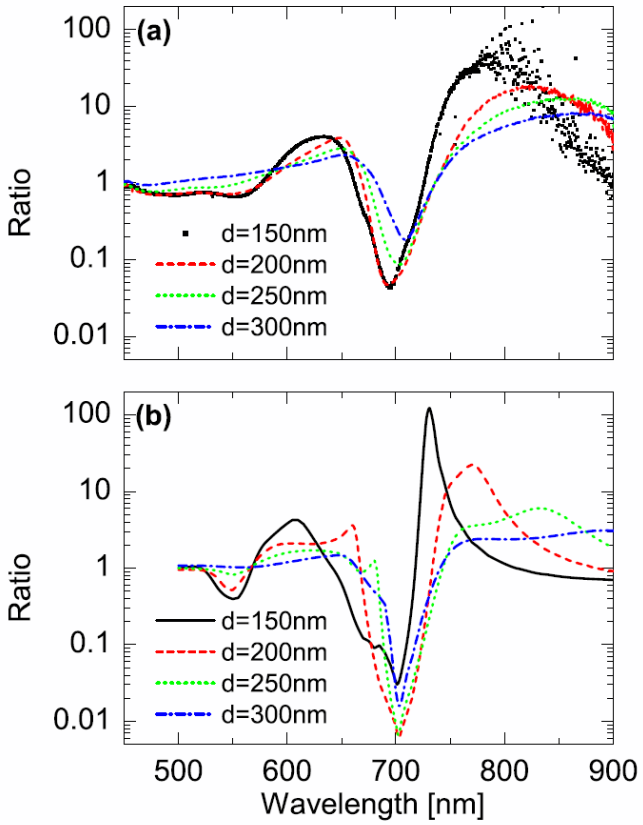

FIG. 40 Experimental (a) and theoretical (b) ratio of the transmission of 40×40 arrays to the transmission of the corresponding single hole with diameters, 150, 200, 250 and 300nm. All data are presented in a logarithmic scale for better visualization. Figure taken from (Przybilla *et al.*, 2008).

Another interesting question is how the finite size effects affect the spatial dependence of the re-emission pattern. This issue was addressed both theoretically and experimentally (Bravo-Abad *et al.*, 2006). As shown in Fig. 43, the re-emission pattern is far from being uniform and, for a hole array of square shape [see panel (b)], the transmission per hole is maximum at the cen-

ter of the sample, decreasing to the edges of the array. Additionally, this re-emission pattern is very sensitive to the angle of incidence. By tilting the samples by just few degrees, the central band of maximum transmittance in Fig. 43(b) moves to the edge of the array. The strong non-uniformity of the light emerging from the hole array is also reflected in time-resolved measurements in the near-field region (Kim *et al.*, 2003; Muller *et al.*, 2003) (see section III.B.8). Interestingly, light emerging from very small arrays also presents very low divergence. It has been shown experimentally that 75% of the transmission is actually non-divergent in arrays formed by just 16 holes, opening perspectives for microscopy applications (Chowdhury *et al.*, 2007; Docter *et al.*, 2006).

7. Polarization effects

Polarization effects associated with the shape of the holes have been already discussed in section II.B.2 for single holes and for 2D arrays in section III.B.4. Here we focus on polarization effects due to the symmetry of the periodic array in relation with the polarization of the incident light.

The coupling of the incident plane wave with the surface EM modes is much more efficient when the direction of the incoming E-field, as projected on the interface, has a non-zero component in the direction of a reciprocal lattice vector. For example, for a simple rectangular lattice, this means that if the normal incident light is polarized along the x-direction, potential resonances owing to reciprocal lattice vectors pointing in the y-direction will not lead to transmission peaks. The influence of the polarization leads to a rich transmission behavior. Depending on the projection of the incident E-field on the various periodicities present in the lattice, results in the excitation of different resonances, each of which will in turn lead to a transmission resonance with its own amplitude, polarization direction and phase. All put together they will determine the polarization state of the transmitted light. The simplest consequence is that, when the sample is tilted away from normal incidence, a geometrical birefringence is introduced. This was first confirmed for THz transmission (Miyamaru *et al.*, 2003) and later for optical frequencies (Ren *et al.*, 2007). Subsequently, the full richness of the polarization behavior was investigated for optical frequencies (Altewischer *et al.*, 2003). For square lattices, normal incidence and a polarization along the $(1, 1)$-direction, SPP modes can be excited in both the x- and y-directions with the same efficiency and phase to the extent that the paths become indistinguishable when far-field experiments are performed.

The ultimate proof of this indistinguishability was given when polarization-entangled photons were transmitted through the subwavelength hole array in this configuration with only a minimal loss to the degree of entanglement (Altewischer *et al.*, 2002; Guo *et al.*, 2007b). By changing the focus of the experimental configuration, the interplay between polarization and the dispersive propagation of the SPP modes led to a deterioration of the degree of entanglement. It was subsequently found experimentally (Altewischer *et al.*, 2005b), and confirmed by theory (Altewischer *et al.*, 2005d; Genet *et al.*, 2005; Moreno *et al.*, 2004a), that the polarization of the beam transmitted by a hole array was depolarized through a combination of a non-local response of the array due to SPP propagation and to the spread of wavevectors in the incident beam. The classical depolarization of a transmitted polarized beam and the quantum decoherence experienced by a polarization-entangled photon pair can be compared (Altewischer *et al.*, 2005a). Under certain conditions the quantum visibility and the classical degree of polarization can be found to be the same. It was also shown that a coupling exists between the temporal and spatial decoherence channels, which may be attributed to transverse propagation of SPPs (Lee *et al.*, 2006b).

Another way to play with the polarization of the transmitted beam is by working with 2D hole arrays made of elliptical holes arranged in two sublattices in which the ellipses are orthogonally oriented. The polarization induced frequency shift of the primary peak can be exploited to gain insight in the energy redistribution in the array (Masson and Gallot, 2006).

8. Dynamics of the EOT phenomenon

In order to gain further understanding of the EOT phenomenon, its dynamics was also investigated. It was found early that the transmission through a subwavelength hole array through a film with typical thicknesses of several hundreds of nm, occurred on a fs timescale (Dogariu *et al.*, 2002, 2001). A transit time was found of 7 fs for a film with a thickness of 300nm. Using the thickness as a distance travelled, this finding indicates a group velocity of $c/7$. The transit time can be related to a lifetime of the resonant modes. This lifetime, which directly determines the linewidth of the transmission peaks, is on the one hand governed by electron-phonon coupling, which leads to Ohmic losses (van Exter and Lagendijk, 1988; Groeneveld *et al.*, 1990). On the other hand, the SPP modes experience radiative losses directly related to the EOT phenomenon itself. It has been neatly shown through ultrafast investigations that the SPP modes had coherent propagation lengths of only a few μm, which is consistent with a (sub)-10 fs lifetime. The radiative lifetime is limited by SPP scattering with the periodic array itself, which leads to the homogeneous broadening of the transmission peaks (Kim *et al.*, 2003). Further investigations have shown that the light transmitted through the subwavelength hole arrays exhibits clear oscillations on a fs timescale (Muller *et al.*, 2003). The observation underpins the coupling between both interfaces of the metal layer through photon tunneling. The diameter of the holes has been found to determine the period and damping of these oscillations. In other words,

the size of the subwavelength holes governs both the coupling between the interfaces but also the radiation damping and hence the linewidth of the transmission peaks. This is in agreement with the theoretical modelling presented in section III.B.2. and it has been corroborated by more sophisticated FDTD calculations (Müller *et al.*, 2004). Similar ringing has also been observed for the transmission of THz pulses through subwavelength metal hole arrays on high resistivity silicon, albeit at different timescales owing to the large difference in frequency (Qu and Grischkowsky, 2004). The radiation-limited lifetime of the SPP modes is crucially influenced by the symmetry of the mode: for the so-called anti-symmetric mode, the radiative damping time constant is reduced by almost an order of magnitude (Ropers *et al.*, 2005, 2006). Visualization of the bound modes in time with sophisticated far-field experiments reveals their group velocity (Rokitski *et al.*, 2005a).

The dynamic measurements of the transmission process (Kim *et al.*, 2003; Muller *et al.*, 2003), which exhibit a two-component structure of a fast transmission of an virtually unperturbed pulse followed by a single long tail, is the temporal fingerprint of a Fano-type process, as discussed before in section III.B.1. Careful investigation of the point spread function provides more proof for the transmission scenario through a Fano process (Altewischer *et al.*, 2006, 2005c). Polarization dependent distortions in near-field investigations confirm the conclusions obtained in far-field investigations (Mrejen *et al.*, 2007).

C. Quasi-periodic arrays

The first experimental study showing the emergence of EOT phenomenon in quasi-periodic arrangements of subwavelength holes was published by Sun *et al.* (2006c). They fabricated an eightfold quasi-periodic hole array with a parallelogram-square tiling system, with the side length of the parallelogram and square being about 550nm. A very broad transmission peak at $\lambda = 700$nm dominated the transmission spectrum. These authors also pointed out that the long-range order existing in the quasi-periodic configuration makes it very similar to a grating and can offer some dominant discrete reciprocal vectors to assist the coupling of the incident EM field with the SPPs of the metal. The next experimental study showing this EOT phenomenon in the optical regime was conducted by Przybilla *et al.* (2006b). They built up 2D Penrose tiles composed of two types of rhombuses, with equal edges but different angles (36^0 for the thin rhombus and 72^0 for the flat one) that are matched to pave all the 2D plane with a fivefold symmetry. For the first time, they were able to correlate the spectral locations of the transmission maxima with peaks in the structure factors of the quasi-periodic arrangements. They also analyzed the variation of the transmission peak heights with the number of holes (N) present in the array, showing that there is a saturation as N increases (associated with the finite mean free path of the SPPs excited by the incoming plane wave). Figure 41 shows a typical experimental spectrum measured through a Penrose tile, as reported by Przybilla *et al.* (2006b). Although periodicity is absent, well defined peaks of enhanced transmission clearly emerge in the spectrum.

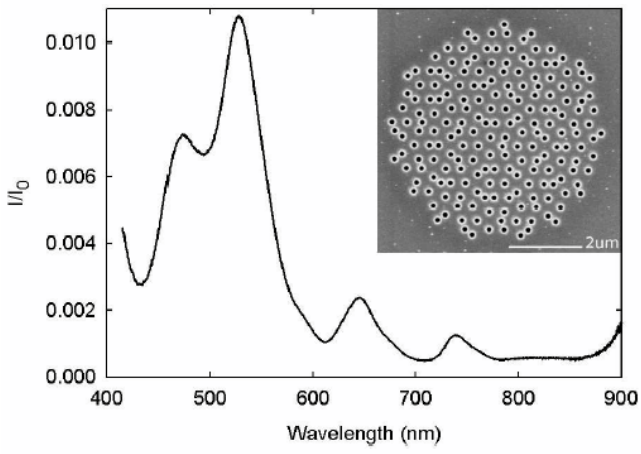

FIG. 41 Optical transmission spectrum of a Penrose array with rhombus edge $P = 450$nm and hole diameter 150nm. The transmitted intensity I is normalized to the incident one I_0. The inset is a scanning electron microscopy image of the array milled through a 300 nm thick silver film. Figure taken from (Przybilla *et al.*, 2006b).

Matsui *et al.* (2007) presented an experimental analysis of the EOT phenomenon in aperiodic arrays of subwavelength holes in the THz regime. They analyzed Penrose tiles exhibiting local five-fold rotational symmetry, similar to the ones analyzed in (Przybilla *et al.*, 2006b) but also Penrose lattices with ten-fold symmetry. This study corroborated the close link between transmission peaks and resonant features of the structure factor (i.e., diffraction pattern of the array). Furthermore, they designed an aperiodic array presenting 18-fold rotational symmetry in real space that was constructed by Fourier-transforming a *circular* 2D diffraction pattern. In this aperiodic arrangement, EOT peaks also appeared and their magnitude was even larger than in the quasi-periodic case. Finally, Papasimakis *et al.* (2007) demonstrated both theoretically and experimentally that EOT in quasi-periodic arrays also emerge in the microwave range of the EM spectrum.

The emergence of EOT phenomenon also in quasi-periodic arrangements made necessary to revisit the theoretical explanation of EOT based on the excitation of surface EM modes, as presented in section III.B.2. In what follows we present a brief summary of the theoretical foundation of the appearance of the EOT phenomenon in quasi-periodic arrays of subwavelength holes. In this section, we apply the general theoretical formalism described in section I.B. Notice that, as Bloch's theorem can not be applied for a quasi-periodic arrangement,

all the structures must be finite. The transmission properties of a finite collection of holes could be treated by means of the general system of Eqs.(1) where index α would run over holes and waveguide modes inside the holes. In order to present a complete picture, in this section we compare the transmission spectra of a periodic square lattice, a Penrose lattice and a random distribution of circular holes (in all cases with $N = 636$). The coordinates in the Penrose lattice were generated by the Dual Generalized Method (Levine and Steinhardt, 1986; Rabson *et al.*, 1991), being the length of the rhombus side defining the structure $L = 600$nm. The ordered structure is a circular portion of a square lattice, with lattice parameter $d = 562$nm, chosen so that the external radius of the circular array is the same as in the quasi-periodic case. In the disordered case, the N holes are randomly placed within the same external radius (but without overlapping). In all cases, the radius of the holes is $r = 130$nm and the depth of the free-standing metal film is $h = 170$nm. These geometrical values are typical of EOT experiments in the optical regime (Przybilla *et al.*, 2006b). Notice that, as we are assuming that the metal behaves as a PEC, our results are applicable to different frequency regimes, just by scaling all lengths by the same factor.

Figure 42 shows the corresponding optical transmission spectra evaluated at normal incidence. The transmittance for the collection of N holes is normalized to N times the normalized-to-area transmission through a single circular hole T_0, i.e., by the transmittance expected for a set of N independent holes. In the ordered case (dashed line), the transmittance spectrum is smooth, with values close to those of independent holes ($T/(NT_0) \approx 1$), except near the resonant peak appearing at $\lambda = 575$nm, where the transmission enhancement is around 13. This is the canonical EOT peak, appearing in periodic arrays at a resonant wavelength slightly larger that the lattice parameter, $d = 562$nm. Resonant transmission also appears when holes are arranged in a Penrose lattice (solid line in Fig. 42), in line with the experimental findings. In the numerical results, transmission enhancements of about 3 and 5 are obtained at the resonant wavelengths $\lambda = 500$nm and $\lambda = 585$nm, respectively. In contrast, the transmission spectra for a random array (dotted line in Fig. 42) does not show any resonant feature, confirming the importance of long-range order to observe EOT effects.

As explained above, the appearance of EOT in quasi-periodic distributions of holes has been phenomenologically related to the lattice structure in reciprocal space, extending arguments borrowed from the ordered case (Przybilla *et al.*, 2006b). Next, we provide quantitative arguments which support this suggestion by working analytically in the reciprocal space, following the derivation presented by Bravo-Abad *et al.* (2007a). The Fourier components of the modal amplitudes can be written as: $E_n(\vec{q}) = \sum_{\vec{R}} \exp(-\imath\vec{q}\vec{R}) E_n(\vec{R})$. Note that now $E_n(\vec{R})$ refers to the modal amplitude in real space of mode n at

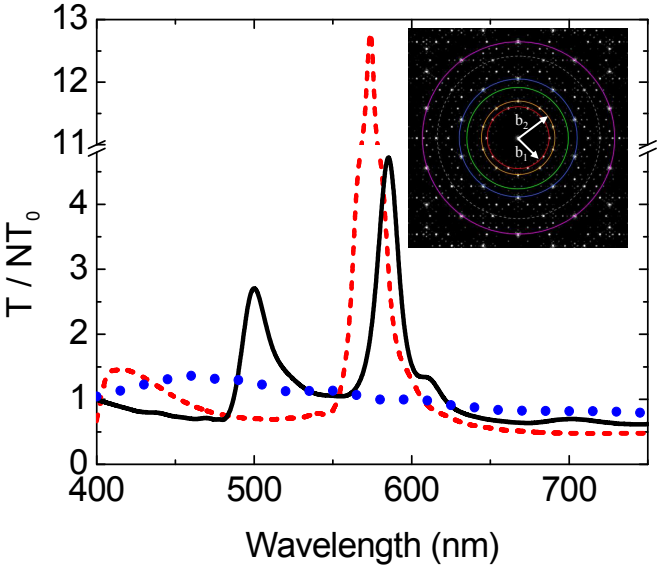

FIG. 42 Transmission (T) spectra for the ordered case (broken line), the Penrose lattice (continuous line) and the random configuration (dots). In all three cases, $r = 130$nm, $h = 170$nm and $N = 636$. T is normalized to the one obtained for N independent holes. Inset shows the structure factor of the Penrose lattice.

the hole location $\vec{R}$. By applying a Fourier-transform to the set of Eqs.(1) [further details can be found in (Bravo-Abad *et al.*, 2007a)], the structure factor of a given distribution of holes [$S(\vec{q}) = \sum_{\vec{R}} \exp(-i\vec{q}\vec{R})$] appears explicitly in the set of equations governing $\{E_n(\vec{q}), E'_n(\vec{q})\}$:

$$\begin{aligned}(\Omega_n(\vec{q}) - \Sigma_n)E_n(\vec{q}) - G^V_n E'_n(\vec{q}) &= I_n S(\vec{q} - \vec{k}_0),\\ (\Omega'_n(\vec{q}) - \Sigma_n)E'_n(\vec{q}) - G^V_n E_n(\vec{q}) &= 0 \end{aligned} \quad (33)$$

where $\vec{k}_0$ is the in-plane component of the incident wavevector. Notet that the set of Eqs.(33) is just the k-space version of the set of linear equations (1).

The re-ilumination term in Eqs.(33), $\Omega^{(\prime)}_n(\vec{q})E^{(\prime)}_n(\vec{q})$, is now represented by the scattering process that couples $E^{(\prime)}_n(\vec{q})$ to the continuum $E^{(\prime)}_m(\vec{k})$, the momentum difference being provided by the lattice through $S(\vec{q} - \vec{k})$:

$$\Omega^{(\prime)}_n(\vec{q})E^{(\prime)}_n(\vec{q}) = \sum_m \int d\vec{k}\, G_{mn;\vec{k}}\, S(\vec{q} - \vec{k})\, E^{(\prime)}_m(\vec{k}) \quad (34)$$

The amplitude of this process is governed by $G_{mn;\vec{k}}$:

$$G_{mn;\vec{k}} = \frac{i}{(2\pi)^2} \sum_\sigma Y_{\vec{k}\sigma} < n|\vec{k}\sigma >< \vec{k}\sigma|m > \quad (35)$$

An important property is that $G_{mn;\vec{k}}$ diverges whenever a p-polarized diffraction wave goes glancing ($k_z = 0$), as can be directly seen from Eq.(35). By looking at Eq.(34), it is clear when and where resonant peaks would emerge in the transmission spectrum for quasi-periodic

arrays. Whenever a divergence in $G_{mn;\vec{k}}$ coincides with a peak in the structure factor, $S(\vec{q})$, Ω_n is maximum. In other words, Ω_n presents maxima at wavelengths corresponding to the glancing condition for the main wavectors of the structure factor. For the quasi-periodic array, this happens for $\lambda_1 = 566$nm ($|\vec{b}_1| = 2\pi/\lambda_1$) and $\lambda_2 = 483$nm ($|\vec{b}_2| = 2\pi/\lambda_2$), see inset of Fig.42. Consequently, T shows two minima at these two wavelengths. At slightly larger wavelengths, two transmission peaks appear in the spectrum, much in the same way as it occurs in periodic arrays. Therefore, we can conclude that the resonant transmission peaks emerging in quasi-periodic arrays stem from the excitation of surface EM modes at the metallic surfaces. Notice that, however, in the quasiperiodic case, there is no minimum wavevector for diffraction [i.e. the structure factor is non-zero for wavevectors with modula smaller than $|\vec{b}_1|$, see inset of Fig.42]. This results in diffraction onto additional radiative modes in vacuum (other than the zero-order mode), which leads to both smaller resonant peaks and less pronounced minima than those appearing in the periodic case.

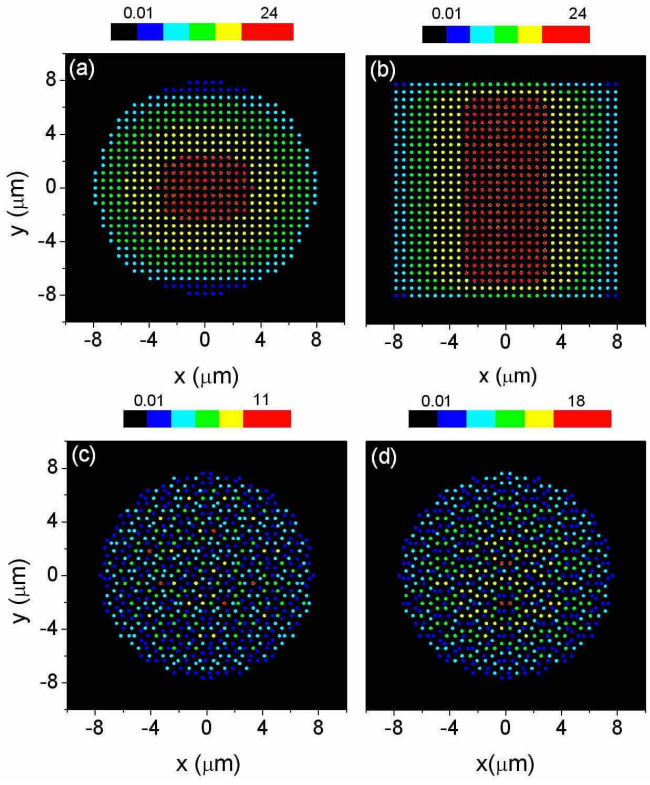

FIG. 43 Transmission-per-hole (normalized to the single hole transmission) displayed in a color scale. Panels (a) and (b) correspond to ordered arrays with circular and square external shapes, respectively. Both patterns were computed at the resonant wavelength of both structures: $\lambda = 575$nm. The results for the Penrose lattice at the corresponding resonant wavelengths are rendered in panel (c) ($\lambda = 500$nm) and panel (d) ($\lambda = 585$nm). The geometrical parameters are the same as in Figure 42.

The fact that surface EM modes are involved in EOT in quasi-periodic systems does not mean that the transmission distribution is uniform across the array. This fact is illustrated in Fig. 43, which renders the transmission per hole in a Penrose lattice of $N = 636$ holes at the two resonant wavelengths ($\lambda = 500$nm and $\lambda = 585$nm in panels (c) and (d) of Figure 43, respectively). For comparison, panels (a) and (b) of Fig. 43 show the corresponding distribution for the ordered array at the resonant wavelength 575nm for circular and square external shapes of the array, respectively. In all four cases, the incident **E**-field is pointing along the x-direction. The pattern in the ordered case can be understood by considering the 2D hole array as a collection of weakly coupled 1D chains of holes (Bravo-Abad *et al.*, 2004a). Due to finite size effects, transmittance is larger at the center of the chain than at the edges. In arrays with a square shape, with one of the axis of the square lattice oriented along the incident E-field, the lengths of all "horizontal" chains are the same, resulting in a characteristic pattern where the edge effects are more noticeable along the direction parallel to the incident field than to the perpendicular one (Bravo-Abad *et al.*, 2006)[see Fig. 43(b)]. On the other hand, when the shape of the square array is circular, the number of holes within field-aligned chains reduces close to the top and bottom regions, and the transmission per hole presents its maximum values just at the central region of the system, as shown in panel (a) of Fig. 43.

In the quasi-periodic arrangement, the transmission-per-hole distribution presents a completely different pattern: it is far from being uniform, showing the appearance of some holes with very high transmittance *hot spots*. Interestingly, at a given resonant wavelength, hot spots show a similar local environment. For $\lambda = 500$nm (panel c), hot spots appear in the center of a pentagon defined by their nearest neighbors while for $\lambda = 585$nm (panel d), hot spots are located within a stadium-like structure. The emergence of these hot spots at the metal surface when light is transmitted through a quasi-periodic array of holes has been experimentally confirmed by taking advantage of their replication in the far-field through the Talbot effect (Dennis *et al.*, 2007; Huang *et al.*, 2007b).

IV. TRANSMISSION THROUGH SINGLE APERTURES FLANKED BY PERIODIC CORRUGATIONS

A. Experimental results

As discussed in previous sections, surface EM modes are known to be responsible of enhancing the transmission of light through periodic and quasi-periodic arrays of subwavelength apertures. The main ingredients to observe the EOT phenomenon are: i) the existence of a surface EM mode. In a metal at optical frequencies, these modes are the SPPs. ii) The presence of a grating coupler that allows the incident light to couple with the surface

EM mode. In the case of a perforated perfect conductor, this grating is also responsible of the formation of the surface EM mode, i.e. a geometrically-induced surface EM mode. This fundamental knowledge suggested the appearance of EOT phenomenon also in single apertures, if they were surrounded by a finite periodic array of indentations. This hypothesis was experimentally verified by Lezec *et al.* (2002); Thio *et al.* (2001) both for a 1D slit surrounded by a finite array of grooves [see Fig.44(a)] and for the *bull's eye* structure (a 2D cylindrical hole flanked by circular trenches, see panel (b) of Fig.44).

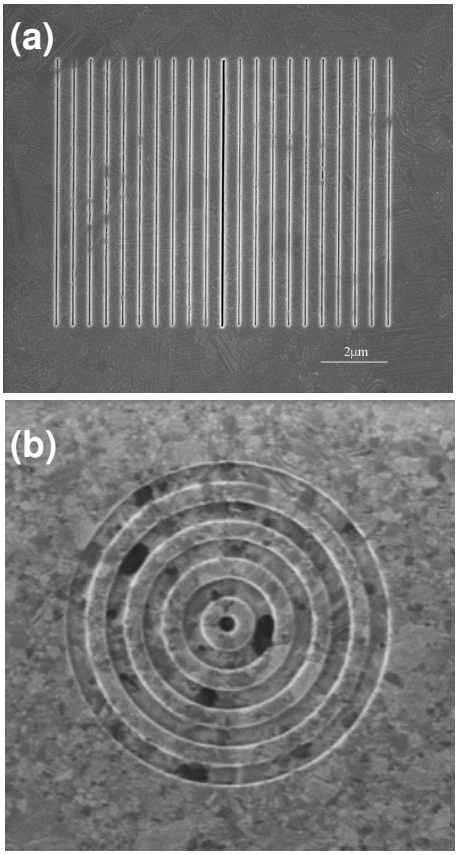

FIG. 44 Electron micrograph images of two samples showing a single aperture surrounded by periodic corrugations. (a) 1D case: a single slit symmetrically flanked by grooves. (b) 2D case: the so-called bull's eye structure, a cylindrical hole surrounded by circular trenches.

Experiments also showed that, unexpectedly, when the periodic corrugation was placed at the output surface of the aperture, the angular distribution of the transmitted radiation was strongly modified (Lezec *et al.*, 2002): light emerged from the structure as a strongly collimated beam, at some resonant wavelengths. Figure 45(a) shows several transmission spectra at various angles (using a collection aperture with an angular resolution of $\pm 3^0$) on the exit side of a single slit of width $a = 40$nm surrounded by 10 grooves with the same width and depth $w = 60$nm and the period of the array is 500nm. The free-standing film is made of silver and the thickness is 300nm. The transmission spectrum is angle dependent, as clearly seen in Fig.45(a). As the collection angle separates from the normal direction, the transmission resonance splits into two smaller peaks that move to lower and higher wavelengths. This implies that, at a given wavelength, light emerges with maximum intensity at a particular angle from the surface. For example, at $\lambda = 580$nm and 800nm, the angles of maximum transmittance are 0^0 and 30^0, respectively. The evolution of the transmittance spectrum with the output collection angle presents a slightly different behavior for the 2D case, the bull's eye geometry, as shown in Fig.45(b). Here, a strong transmission peak is evident at $\lambda = 660$nm with an intensity that strongly reduces as the collection angle increases. This implies that light emerges as a well-defined beam with a full-width at half maximum (FWHM) divergence of $\pm 5^0$ for the resonant wavelength, $\lambda = 660$nm. When the finite angular resolution of the experimental apparatus is taken into account, the actual beam divergence is reduced to $\pm 3^0$. Atomic fluorescence mapping of the optical field intensity profile of these structures suggests an even smaller beam divergence (Gay *et al.*, 2005).

In a detailed experimental analysis of the transmission process through a bull's eye structure on a suspended silver film, with corrugations on one or both metal-air interfaces, it was demonstrated that the total transmission through the structure is the product of three distinct contributions: the coupling efficiency on the input surface, the transmission or cutoff function of the aperture and decoupling efficiency of the output surface (Degiron and Ebbesen, 2004). It was found that the SPP grating modes of the input surface dominate the bull's eye spectrum, eventhough the contribution of the localized mode of the central hole can still be detected as in the case of hole arrays (see section III.B). The beaming effect is however controlled by the corrugations of the output surface as further discussed in section IV.B.

Both enhanced transmission and beaming phenomena in single apertures have been observed in other frequency regimes. Within the microwave range of the EM spectrum, Hibbins *et al.* (2002) presented a study of the enhanced transmission of radiation through a single slit placed at the center of a pair of grooves. The beaming effect in 1D structures at this frequency range was analyzed in detail by Akarca-Biyikli *et al.* (2004), reporting a 4^0 angular divergence for a system with 10 grooves. The 2D case (bull's eye geometry) at microwave frequencies was first addressed by Lockyear *et al.* (2004, 2005). In this reference, a single hole surrounded by four circular trenches also presented both enhanced transmission and beaming effects.

In the THz range of the EM spectrum, it was possible to analyze the phenomenon of enhanced transmission for the 2D bull's eye geometry in the time domain (Agrawal *et al.*, 2005), allowing a detailed study of the transmission process. These authors were able to determine the contribution of each individual groove to the transmitted terahertz waveform. A posterior development demon-

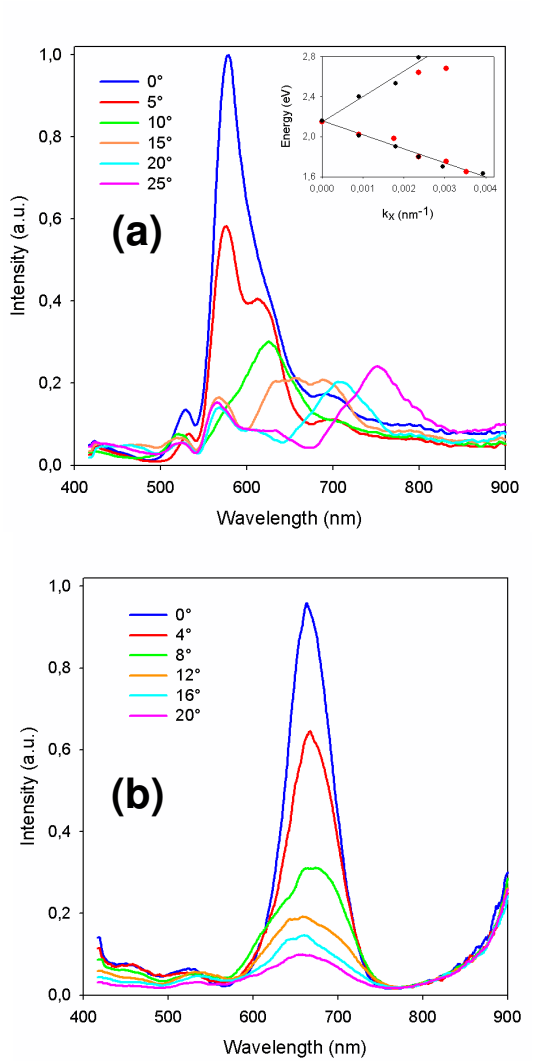

FIG. 45 (a) Transmission spectra for a single slit flanked by a periodic array of 10 grooves (5 grooves placed to the left and right of the slit). The width of the slit and grooves is 40nm, the groove periodicity is $d = 500$nm and the metal thickness is $h = 300$nm. The nominal depth of the grooves is 60nm. The spectra are recorded at various collection angles, from 0^0 to 25^0. The normal incident radiation is p-polarized. The inset shows a dispersion curve of the transmission peaks locations versus parallel momentum. (b) Transmission spectra for the bull's eye geometry: a cylindrical hole of diameter 250nm is milled into a silver film of thickness 300nm. It is surrounded by 5 circular trenches of depth 60nm and the groove periodicity is 600nm. The tail above $800nm$ is an experimental artifact. Figure taken from (Lezec *et al.*, 2002).

strated, also in this frequency regime (Cao *et al.*, 2005), that by varying the phase of the surface corrugation relative to the central aperture, dramatic changes can be made in the transmission resonance lineshape. Beaming effects at THz frequencies were studied by Agrawal and Nahata (2006). It was shown how each groove produces a time-delayed replica of the total THz pulse that is evanescently coupled through the subwavelength aperture. These replicas are coherently superposed on each other and temporally shifted from one another in accordance with the spatial distance between grooves.

There have been several studies dedicated to improving both the enhanced transmission and beaming capabilities of the basic structure discovered in 2002. Ishihara *et al.* (2005a,b) demonstrated that the inclusion of a Bragg reflector into the structure further increases the enhanced transmission through the bull's eye geometry, if this contains a small number of rings. The same group has recently shown (Ishihara *et al.*, 2006) that by changing the aperture from a circular one to a bow-tie shaped aperture, not only the transmittance is largely increased but the spatial resolution of this structure is of the order of $\lambda/17$. On the other hand, Caglayan *et al.* (2006b) have experimentally tested the beaming capabilities of annular apertures surrounded by periodic arrays of concentric grooves, showing that the angular confinement can be as strong as 3^0. Another important improvement on the transmissivity of these structures is associated with the use of sharp-apex shape for the grooves in the periodic grating (Ishi *et al.*, 2005b). Fabricated samples with this type of gratings shows greater transmission than that of samples with a rectangular grooves. Also, a modulation of the groove depth along the periodic array of indentations (Shi *et al.*, 2007) can lead to a better confinement of the light emerging from the subwavelength aperture.

Theoretical calculations showed (Bravo-Abad *et al.*, 2003) that resonant transmission and collimation of light can be achieved for two different wavelengths, when the single aperture is surrounded by asymmetric configurations of periodic arrays of indentations. The generation of off-axis directional beaming of light by a single subwavelength slit perforated on a metal film has also been recently proposed (Kim *et al.*, 2007; Lin *et al.*, 2007). The combination of single apertures perforated on a metal film with dielectric surface gratings (as proposed by Lin *et al.* (2006)) seems to offer a better performance than the one obtained when metallic gratings are considered. Along this line, it has been shown that the dielectric properties of the surface surrounding the aperture can be modulated by using metallic heterostrutures constructed with aluminum and silver (Wang and Wang, 2006). Very recently, Li and colleagues (Li *et al.*, 2008) have also proposed an improved structure by surrounding the central aperture with nonuniform and nonperiodic grooves. In this way, the amplitude and phase of the power flowing from each groove can be adjusted in order to enhance the final transmission.

An interesting spin-off of EOT and beaming effects in corrugated single apertures has been the appearance of both phenomena in the so-called photonic crystals. As stated before, the main ingredient to observe both phenomena is the excitation of surface EM modes. A photonic crystal may support a surface EM mode whose band may lie within the photonic band gap of the material, depending on the truncation of its surface. The emergence of both phenomena in photonic crystal waveguides

was theoretically predicted by Moreno *et al.* (2004b). In a parallel development, Kramper *et al.* (2004) reported the emergence of directional beams with very low divergence angles from photonic crystal waveguides of subwavelength width. They also identify the key role played by the evanescent surface EM modes in achieving the low divergence beams. Since the publication of these two articles, several works have been devoted to analyze EOT and beaming phenomenon in photonic crystals. The first experimental study on the enhanced transmission assisted by surface modes in photonic crystals was presented by Bulu *et al.* (2005). Further theoretical investigations of those two effects (Frei *et al.*, 2005; Moreno *et al.*, 2004c; Morrison and Kivshar, 2005; Tang *et al.*, 2006) focused on the optimization of the surface geometry surrounding the waveguide in order to enhance both the transmission and collimation of the emerging beam. Two very recent experimental reports have been devoted to improving the directionality of the transmitted beam by tuning the number of grating layers (Moussa *et al.*, 2007) and to enlarge the operation bandwidth of the beaming effect by playing with the phase of the multiple beams emitted out of the surface of the photonic crystal (Li *et al.*, 2007).

B. Theoretical modelling

The theoretical modelling of both enhanced transmission and beaming effect in single apertures have confirmed that surface EM modes excited at the corrugated metal surface(s) play a key role in the emergence of both phenomena (Garcia-Vidal *et al.*, 2003a; Martin-Moreno *et al.*, 2003). This physical explanation has been corroborated and refined by other theoretical approaches and numerical investigations (Thomas and Hughes, 2004; Wang *et al.*, 2006a,b; Yu *et al.*, 2005). In what follows we present the theoretical foundation of these two phenomena (enhanced transmission and beaming) for the basic 1D structure, a single slit surrounded by a finite array of grooves (see Fig.46). It is worth mentioning here that the physical origin of the resonant phenomena in single apertures for 1D and 2D structures is very similar, as shown by Chang *et al.* (2006).

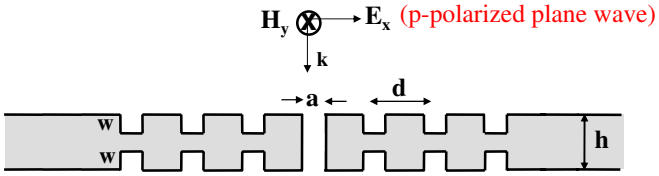

FIG. 46 Schematic picture of a single slit of width a in a metallic film of thickness h. This single slit is surrounded symmetrically by $2N$ grooves (of width a and depth w) in both the input and output surfaces. The structure is illuminated by a normal incident p-polarized plane wave.

In order to simplify to the maximum the modelling, we consider that the metal is a PEC and take into account only the TEM modes inside the central slit and grooves. For this case, the general system of equations (1) translates into:

$$\begin{aligned}(G_{\alpha\alpha}-\Sigma_\alpha)E_\alpha+\sum_{\beta\neq\alpha}G_{\alpha\beta}E_\beta-G^V_\alpha E'_\alpha\delta_{\alpha 0} &= I_\alpha\\ (G_{\gamma\gamma}-\Sigma_\gamma)E'_\gamma+\sum_{\nu\neq\gamma}G_{\gamma\nu}E'_\nu-G^V_\gamma E_\gamma\delta_{\gamma 0} &= 0\end{aligned} \quad (36)$$

where index α denotes the TEM mode at indentation α (either the slit or the grooves). The central slit is represented as $\alpha = 0$ and, as shown in Eqs.(36), it is the only one in which the input and output modal amplitudes are electromagnetically coupled. The expressions for the different magnitudes appearing in this set of equations are: $\Sigma_0 = \cot(k_\omega h)$, $\Sigma_\alpha = \cot(k_\omega w)$ for $\alpha \neq 0$, $G^V_0 = 1/\sin(k_\omega h)$. We consider p-polarized normal incidence and the illumination term, I_α=2i, is such that the flux over the central slit is normalized to 1. The electromagnetic coupling between indentations α and β, $G_{\alpha\beta}$, can be expressed shortly as $<\alpha|\hat{G}|\beta>$ where the expression for the propagator $\hat{G}$ in real space is given by Eq.(A18). Once the self-consistent set of modal amplitudes is obtained, the final transmittance through the central slit can be calculated by means of the equation: $T = G^V_0\, Re[E^*_0 E'_0]$.

First, we analyze the influence of patterning the input surface surrounding the central on the final transmittance through the structure. Figure 47 shows the dependence of the normalized-to-area transmittance, $T(\lambda)$, with the number of grooves. The notation $[N, 0]$ means that $2N$ grooves are placed symmetrically to the left and right of the central slit at the input surface, whereas the output surface presents no corrugation. For the calculation of all the spectra displayed in Fig.47, we have chosen the geometrical parameters: $a = 0.08d$, $w = 0.2d$ and $h = 0.7d$. As in previous cases, the period of the array, d, is used as the unit length of the structure. The curve for $N = 0$ corresponds to the single slit case. In this wavelength regime $T(\lambda)$ presents two maxima whose origin is related to the excitation of Fabry-Perot resonances inside the slit, as discussed in section II.A. Fig.47 also shows that a maximum in $T(\lambda)$ develops at $\lambda \approx 1.1d$ as the number of grooves is increased. The enhancement factor for $N = 10$ is around 9 and it can be shown that there is a saturation of this peak value as N is larger than 10 for this particular set of geometrical parameters (Garcia-Vidal *et al.*, 2003a). Notice also that the transmission peaks associated with the excitation of Fabry-Perot resonances of the single slit remain almost unaltered when grooves are placed at the input surface.

Figure 48 shows that the output corrugation has little effect on the total transmittance: the spectra for different number of grooves at the output surface are similar to the single slit spectrum (black curve). Corrugating the output surface induces a change in $T(\lambda)$ of, at most, some

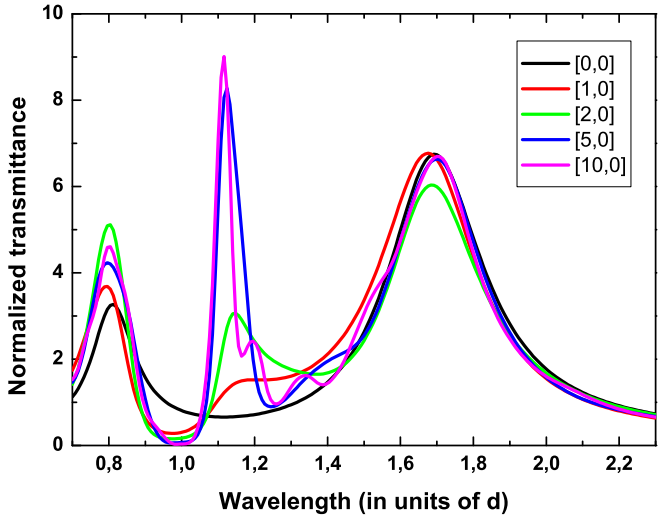

FIG. 47 Normalized-to-area transmittance as a function of the number of grooves when only the input surface is corrugated. The width of the slit and grooves is $a = 0.08d$, the depth of the grooves is $w = 0.2d$ and the metal thickness is $h = 0.7d$. Notation $[N, 0]$ means that $2N$ grooves are perforated in the input surface and 0 in the exit surface. Figure taken from (Garcia-Vidal *et al.*, 2003a).

20% at the resonant wavelength.

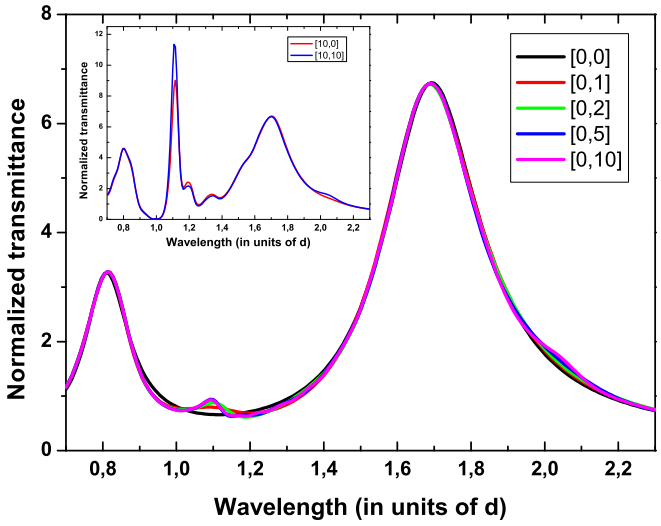

FIG. 48 Normalized-to-area transmittance as a function of the number of grooves when only the exit surface of the slit is corrugated. As in Fig.47, the width of the slit and grooves is $a = 0.08d$, the depth of the grooves is $w = 0.2d$ and the metal thickness is $h = 0.7d$. Notation $[0, N]$ means that $2N$ grooves are milled at the exit surface and 0 at the input surface. The inset shows the transmittance for the $[10, 0]$ and $[10, 10]$ configurations. Figure taken from (Garcia-Vidal *et al.*, 2003a).

Therefore, in order to understand the features appearing in the total transmittance, we concentrate on the analysis of the structure in which the single slit is surrounded by a finite array of indentations at the entrance surface. In this case, the system of equations (36) can be further simplified to a set of $2N + 2$ equations, being $2N$ the number of grooves:

$$(G_{\alpha\alpha} - \Sigma_\alpha)E_\alpha + \sum_{\beta\neq\alpha} G_{\alpha\beta}E_\beta - G^V_\alpha E'_\alpha \delta_{\alpha 0} = I_\alpha$$
$$(G_{00} - \Sigma_0)E'_0 - G^V_0 E_0 = 0 \quad (37)$$

From these equations, it is possible to identify two mechanisms that could enhance $T(\lambda)$ (additionally to the Fabry-Perot resonances already emerging in single, isolated slits). The excitation of groove cavity modes provide large E_α at the resonant condition $G_{\alpha\alpha} - \Sigma_\alpha \approx 0$. For the case of very narrow grooves, this condition is fulfilled for $\lambda = 4w/(2n+1)$, with n integer. From Eqs.(37) it is clear that large E_α can provide extra illumination into the central slit. However, the situation is more complicated because this re-illumination process at the central slit depends on a weighted sum over all E_α, so extreme care must be taken of the phases of the different contributions coming from the grooves. As explained before, the coupling between grooves and central slit, $G_{\alpha 0}$, is governed by the Hankel function $H_0^{(1)}(x)$ (for a perforated PEC). From the asymptotic behavior of $H_0^{(1)}$ for large x, $G_{\alpha 0} \approx exp(ik_\omega d|\alpha|)$. Therefore, all light that is re-emitted by the grooves reaches the central slit in phase for $\lambda = d$. The extra peak in transmittance appearing at λ close to d is due to the combination of these two mechanisms: groove cavity mode excitation and in-phase groove re-emission.

This theoretical explanation based on those two mechanisms can be further elaborated by invoking the formation of a geometrically-induced surface EM mode when the surface of a semi-infinite PEC is perforated by a periodic array of 1D grooves. As in the case of a 1D array of slits, it is possible to calculate the dispersion relation of the surface EM modes supported by an infinite periodic array of grooves. For this case, within the single TEM mode approximation, the equation from which the dispersion relation of the EM modes propagating along this structure can be extracted is quite simple: $G - \Sigma = I$, where $\Sigma = \cot(k_\omega w)$ and $G = \frac{a}{d}\frac{k_\omega}{\sqrt{k_x^2 - k_\omega^2}}$ if we ignore diffraction effects. The resulting dispersion relation is simple written as:

$$\frac{\sqrt{k_x^2 - k_\omega^2}}{k_\omega} = \frac{a}{d}\tan k_\omega h \quad (38)$$

These surface EM modes may become leaky modes when diffraction effects are considered. As a first approximation, the spectral locations of the surface EM modes which can be excited by a normal incident p-polarized plane wave can be calculated from Eq.(38) by imposing $k_x = 2\pi/d$. Fig. 49 shows the close correspondence between the spectral locations of both the transmission resonances and the surface EM modes for an infinite array

of rectangular grooves (with the same geometrical parameters). Figure 49 also shows (white dots) that these surface EM modes originate from the interplay between the groove cavity mode [$\tan k_\omega h \to \infty$ in Eq. (38)] and the in-phase groove re-emission mechanism (in the limit $h \to 0$, $k_x \to k_\omega$ in Eq.(38)).

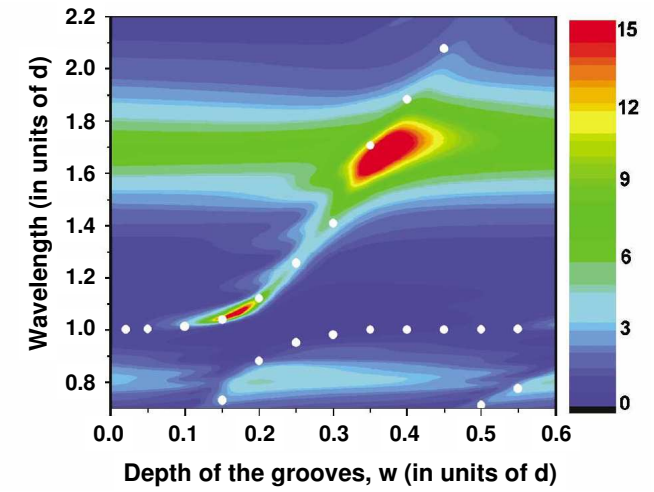

FIG. 49 Contour plot of the transmittance versus groove depth (w) and wavelength (both in units of d) when a central slit is flanked symmetrically by 20 grooves. Here $a = 0.08d$ and the thickness of the metal $h = 0.7d$. White dots correspond to the locations of the surface EM modes of an infinite array of rectangular grooves with varying w as calculated from Eq.(38) with $k_x = 2\pi/d$. Figure taken from (Garcia-Vidal *et al.*, 2003a).

This link between transmission resonances and excitation of surface EM modes is illustrated in Fig. 50 which renders the E-field amplitude for the $[10, 0]$ case analyzed in Fig. 47 and evaluated at the resonant wavelength $\lambda = 1.1d$. It is clearly seen that this surface EM mode excitation is accompanied by a large enhancement of the E-field inside the grooves, whose re-emission into the central slit leads to an enhancement of the transmittance. This surface EM mode acts as a funnel that collects the light impinging at the area surrounding the slit and is able to re-direct it into slit area.

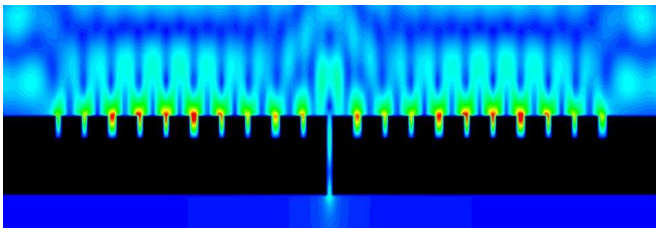

FIG. 50 Electric field amplitude associated with the transmission peak $\lambda = 1.1d$ emerging when a single slit when is flanked by 20 grooves, placed symmetrically at its entrance surface. The geometrical parameters of the structure are as in Fig.47.

The existence of two types of resonances (Fabry-Perot cavity mode and surface EM mode) to enhance the transmission through a single subwavelength slit surrounded by a periodic corrugation has been experimentally observed (Garcia-Vidal *et al.*, 2003a). In this work, several silver films of thickness $h = 350$nm were evaporated on top of a quartz substrate. Different samples corresponding to different values of d and w were fabricated by using a focused-ion-beam that milled a single slit surrounded by 10 grooves. The central slit and grooves were 10 microns long with a width of $a = 40$nm. The transmittance spectrum of a single slit which presents a broad maximum, associated with a Fabry-Perot mode excitation, at around $\lambda = 725$nm [see black curve and inset of Fig.51(a)]. Fig.51(a) also shows the transmittance spectra when the slit is surrounded by grooves of nominal depth equal to 40nm and different values of d, ranging from $d = 500$nm to $d = 800$nm. Under the presence of a period array of grooves, an additional peak emerges in the spectrum and moves to larger wavelengths as d is increased. The peak is strongest for $d = 650$nm, when it appears at a wavelength that coincides with the slit waveguide mode excitation, $\lambda = 750$nm. Panel (b) of Figure 51 shows that there is an optimum value for the depth of the grooves, as predicted by the theoretical calculations. For the considered set of geometrical parameters (with $d = 650$nm), the optimal depth is $w = 40$nm, for which the experimental normalized transmittance is of the order of 7.

Let us now present the theoretical foundation of the beaming phenomenon for the 1D case, a single slit flanked by a periodic array of grooves. As shown before, the angular distribution of the transmitted light depends only on the properties of the output surface. Therefore, we can focus on a simplified geometry, composed by a single slit (driven by a wave of amplitude A_0) and surrounded by a finite array of grooves at its exit surface. We are not interested here in analyzing the total transmittance but how light is spatially distributed in the far field region. Within both the single TEM mode and PEC approximations, the set of equations that describe this electromagnetic problem can be written as:

$$(G_{\alpha\alpha} - \Sigma_\alpha)E_\alpha + \sum_{\beta\neq\alpha} G_{\alpha\beta}E_\beta = 2iA_0\delta_{\alpha 0} \qquad (39)$$

where now $\Sigma_0 = -i$ for the central slit and $\Sigma_\alpha = \cot(k_\omega w)$ for the grooves. The illumination term is now characterized by the amplitude A_0 of the TEM that is propagating towards the interface. Indexes α and β run over all indentations (slit and grooves). Once the different modal amplitudes are obtained, it is possible to calculate the y-component of the magnetic field in the transmission region ($z > 0$):

$$H_y(\vec{r}) = \frac{1}{\mu_0 c}\sum_\alpha E_\alpha G(\alpha, \vec{r}) \qquad (40)$$

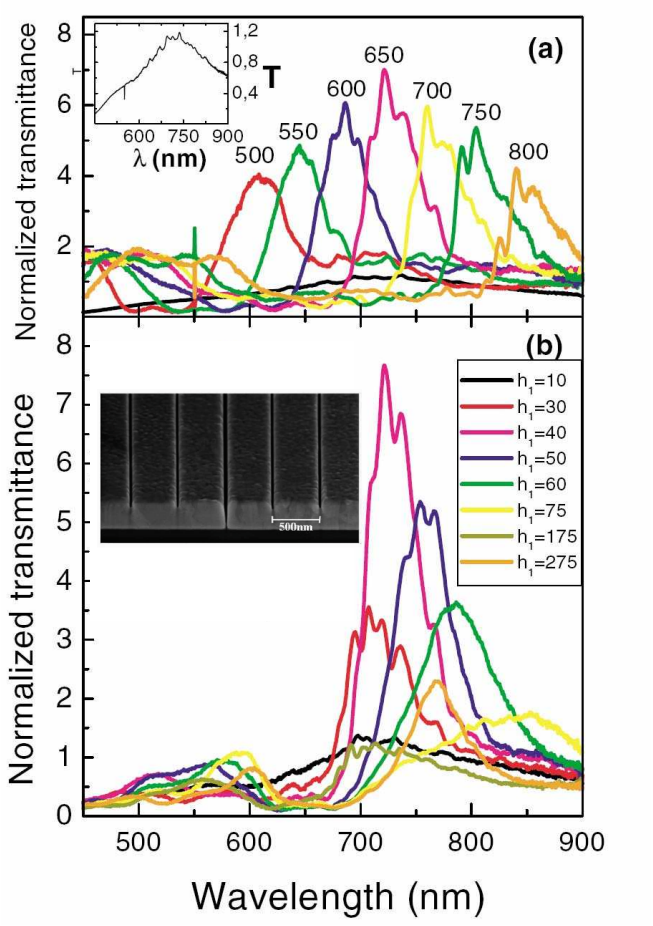

FIG. 51 Collection of several normalized-to-area transmittance spectra for different structures formed by a central slit symmetrically flanked by 10 grooves on the input surface ($[5,0]$ in our notation). The width of the slits is 40nm and the thickness of the free standing silver film is $h = 350$nm. (a) In these spectra the depth of the grooves is fixed at $w = 40$nm and the period of the groove array d is varied between 500 and 800nm. Black curve corresponds to the single slit that is also reproduced in the inset for clarity (b) Here the period is fixed $d = 650$nm and the depth of the grooves is changed between $w = 10$nm up to $w = 275$nm. Inset shows an electron micrograph image of one of the devices analyzed. Figure taken from (Garcia-Vidal *et al.*, 2003a).

For the polarization we are considering (p-polarized light), all the other components of the EM fields can be obtained from $H_y(\vec{r})$. In particular, the radial component of the Poynting vector, $S_r(\theta,\lambda)$, can be computed. This magnitude governs the angular distribution of the transmitted radiation, $I(\theta,\lambda)$, that can be directly evaluated from S_r as: $I = rS_r(\theta,\lambda)/T(\lambda)$ in the limit $r \to \infty$. Note that this angular distribution is normalized to the total transmittance, $T(\lambda)$. In this way, $I(\theta,\lambda) = 1/\pi$ for a single slit in the extreme subwavelength limit.

It is worth noticing that the propagator that connects indentation α with point $\vec{r}$, $G(\alpha,\vec{r})$, is also related to $H_0^{(1)}$:

$$G(\alpha,\vec{r}) = \frac{ik_\omega}{2\sqrt{a}} \int_{x_\alpha - a/2}^{x_\alpha + a/2} H_0^{(1)}(k_\omega |x\vec{u}_x - \vec{r}|)dx \qquad (41)$$

where x_α is the x-coordinate of the center of indentation α. As Eq.(40) shows, the system under consideration behaves like an equivalent diffraction grating, in which the EM field amplitudes at the emitters present a strong dependence on wavelength and on the distance to the central slit, as we shall show below.

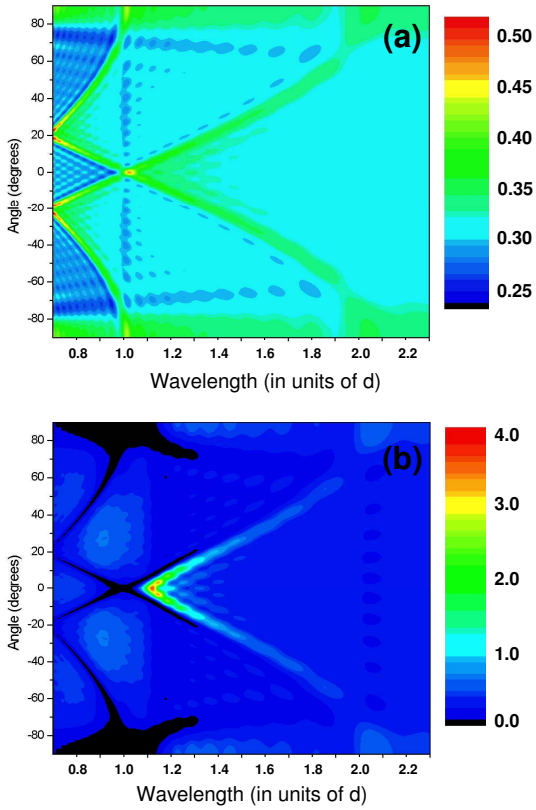

FIG. 52 Contour plots for $I(\theta,\lambda)$ for two different groove depths, $w = 0.02d$ in panel (a) and $w = 0.2d$ in panel (b). The width of the central slit and grooves is $a = 0.2d$. The number of grooves that are placed symmetrically with respect to the central slit is 20. Figure taken from (Martin-Moreno *et al.*, 2003).

Figure 52(a) shows $I(\theta,\lambda)$ for very shallow grooves, $w = 0.02d$. In this case, the angular transmission profile is well described a diffraction-like first order approximation as $|E_\alpha| \ll |E_0|$. In this case, $\Sigma_\alpha \gg 1$ (for $\alpha \neq 0$) and for the central slit $E_0 \approx 2iA_0/(G_{00} - \Sigma_0)$. In this weak coupling limit, $E_\alpha \approx -G_{\alpha 0}E_0/(G_{\alpha\alpha} - \Sigma_\alpha)$. From the asymptotic expansion of $H_0^{(1)}(k_w x)$, $|E_\alpha| \propto \alpha^{-1/2}$, while the phase of E_α is $\phi_\alpha = k_w d|\alpha| + \phi$ for groove α and a value ϕ_0, not following the previous law, for the central slit. The origin of the weak beaming observed in Fig.52(a) at angles $\theta^{(m,\pm)}(\lambda) = \arcsin(m\lambda/d \pm 1)$, for integer m is that, as the phase difference for grooves at one of the slit is constant, it can be cancelled by

the far field at those angles. When w is increased, Σ_α and $G_{\alpha\alpha}$ may be comparable (leading to large E_α) and self-consistency is needed when solving the set of linear equations (39). Indeed, close to groove cavity mode condition, $Re(G_{\alpha\alpha} - \Sigma_\alpha) = 0$, we find the formation of a collective surface EM mode, characterized by a large increase of E_α and a more pronounced beaming phenomenon, as observed in Fig.52(b). As discussed by Martin-Moreno *et al.* (2003), it is possible to associate the non-convergence of iterative solutions to the set of linear Eqs.(39) with the building-up of surface EM resonances. In this case, these surface EM modes are leaky modes as they couple to radiative modes. This interpretation of the beaming phenomenon in terms of the excitation of surface EM modes is also supported by the coincidence of the resonant wavelength in which beaming phenomenon at 0^0 occurs with the wavelength of maximum transmittance (when the same corrugation is placed at the input surface).

Associated with the beaming effect, there is also a focusing effect (Garcia-Vidal *et al.*, 2003b). Figure 53 serves as an illustration of this new phenomenon. This figure renders the E-field amplitude evaluated at the resonant wavelength for the case $N = 10$. A very elongated focus emerge in the intermediate field regime, between the near and far fields. The center of the focus is located at around 100 times the wavelength of the EM field. As in the case of beaming, this lensing ability (focal depth, length and width) is controlled by the output corrugation. A complete characterization of this focusing effect was presented by Garcia-Vidal *et al.* (2003b).

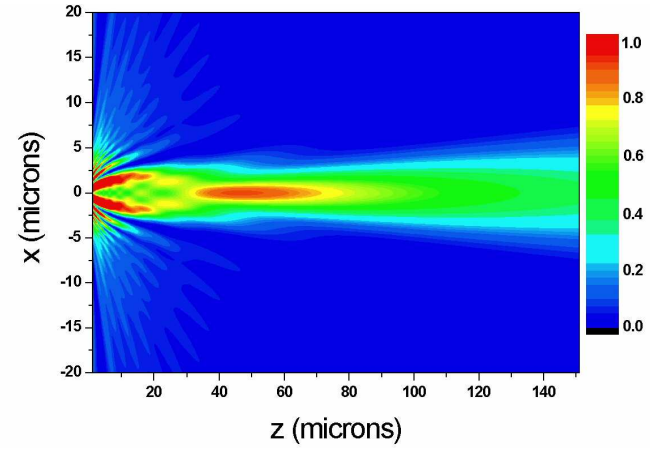

FIG. 53 Electric field amplitude profile (in arbitrary units) as a function of x and z for the case $N = 10$ with $a = 0.08d$ and $w = 0.17d$ that correspond to the optimal parameters for beaming. In this case d is chosen to be 500nm, as in experimental samples discussed in section IV.A. This E-field profile is evaluated at the resonant wavelength, $\lambda_R = 1.06d$. Figure taken from (Garcia-Vidal *et al.*, 2003b).

V. APPLICATIONS

Before the EOT phenomenon was reported in 1998, subwavelength apertures were commonly seen as suffering from poor transmission and strong diffraction. For instance, for scanning near-field optical microscopy (SNOM), the aperture provided the subwavlength resolution but was also the source of the low signal intensity, typically explained with Bethe's theory (Betzig and Trautman, 1992). For the past decade, the potential applications of subwavelength apertures has been revisited with the new understanding that the EM fields can be strongly enhanced at the apertures in the metal film. The interest has been further stimulated by the high contrast provided by these structures combined with the possibility of tailoring their properties by sculpting the metal surface. The two areas that have been the object of numerous studies are molecular sensing and spectroscopy and stand-alone photonic devices. These applications will be presented in greater detail below.

A. Molecular Sensing and Spectroscopy

Surface plasmons have played a major role in sensing and molecular spectroscopy for the past 30 years, for instance in the detection of small refractive index variations by the technique known as surface plasmon resonance (SPR) (Nylander *et al.*, 1982) and in surface enhanced Raman spectroscopy (SERS) (Jeanmaire and Van Duyne, 1977). With this in mind and considering the involvement of SPPs in the EOT process, it is not surprising that aperture structures have been extensively explored for spectroscopic purposes. In addition, aperture structures can be added easily to standard equipment. Since applications in this area has already been the subject of detailed reviews (Coe *et al.*, 2008, 2006; Gordon *et al.*, 2008; Sinton *et al.*, 2008), only representative studies will be outlined below. Aperture structures have been used for molecular absorption, fluorescence, vibrational spectroscopy (IR and Raman) and SPR.

SPR. In traditional SPR, minute refractive index variations are measured at the interface of a translucent metal film placed on a prism. A light beam impinges on the back of the metal film and is mostly reflected except at an angle or wavelength which allows evanescent coupling to SPPs on the opposite side. This coupling condition is very sensitive to the local index and hence any molecular process at the surface that results in a net index variation can be detected. The transmission of hole arrays are also very sensitive to the refractive index at the metal surface (Krishnan *et al.*, 2001), and the binding of biomolecules can be followed by simply measuring a shift in the transmission peaks under a microscope (Brolo *et al.*, 2004b; Liu and Blair, 2004). The simplicity of the setup was however offset by low sensitivity due to the broadness of the peaks. Further developments have brought the sensitivity to a level where this approach is competitive

with existing commercial SPRs apparatuses (Stark *et al.*, 2005; Tetz *et al.*, 2006). For instance, by adding two polarizers at 90 degrees in the path of the transmitted beam, the hole array transmission peak becomes so narrow that refractive index variations smaller than 10^{-5} can be detected (Tetz *et al.*, 2006). Isolated holes as well as disordered patterns of holes have also been used, demonstrating the various approaches that can be used for SPR sensing (Dahlin *et al.*, 2005; Gao *et al.*, 2007; Rindzevicius *et al.*, 2005).

Enhanced Absorption. The use of hole arrays to measure molecular vibrational spectra illustrate very well the potential of metallic aperture structures for spectroscopy. In 2003, Coe and colleagues reported that an array tuned to the IR with transmission resonances around $1000cm^{-1}$ could enhance the molecular absorption by at least two orders of magnitude (Williams *et al.*, 2003). The free standing arrays covered with a molecular monolayer was simply placed in the beam of a commercial FTIR and the transmission spectra recorded. Except for some spectral deconvolution, the approach is simple and allows to follow chemical processes such as catalysis (Coe *et al.*, 2006). The enhancement is related to the lifetime of the SPP, or the SPP propagation length, on the arrays surface which increases the absorption probability by the molecules. In the visible, the absorption enhancement is smaller (factor ca. 10), due to the reduced SPP propagation length (Dintinger *et al.*, 2006a). Nevertheless, because the incident beam is reconstructed at the exit of hole array, the latter can be easily used in pump-probe to do time resolved spectroscopy and explore, for instance, excited state properties of very thin molecular layers or SPP-molecule interactions (Dintinger *et al.*, 2006b). SERS has also been investigated on hole arrays (Brolo *et al.*, 2004b; Lesuffleur *et al.*, 2007a; Reilly *et al.*, 2007; Reilly and Rowlen, 2004). In a thorough quantitative analysis of the Raman signal intensity from a non-resonant probe at monolayer concentrations placed a hole array in Ag films reveals that out of the 6×10^7 observed enhancement factor, 10^5 is the result of the Ag film roughness whereas 600 is associated with the SPP modes at the apertures (Reilly *et al.*, 2007).

Fluorescence. Considering the absorption enhancement discussed above, it is only natural to expect that fluorescence can also be boosted. Indeed this has been demonstrated using both single and arrays of apertures (Brolo *et al.*, 2006, 2005; Levene *et al.*, 2003; Liu and Blair, 2003; Rignault *et al.*, 2005). To analyze the enhancement, several factors have to be considered. The fluorescence can be increased due to the enhancement of the excitation rate but the radiative lifetime and the fluorescence quantum yield can also be modified. For instance, the fluorescence is quenched at short distances from the metal surface (< 20 nm) and can be boosted at longer distances (Barnes, 1998; Drexhage, 1974). Finally the environment can modify the radiation pattern of the fluorophore. Fluorescence correlation spectroscopy can particularly benefit from the use of a subwavelength aperture (Edel *et al.*, 2005; Levene *et al.*, 2003; Rignault *et al.*, 2005; Wenger *et al.*, 2008). The analyzed volume is reduced by 10^3 as compared to using the focal point of a laser beam which in turn allows the characterization of molecular fluorescence statistics at physiological concentrations (Blom *et al.*, 2006). Both the excitation and emission can be enhanced due to an increase in the local density of states at the aperture (Wenger *et al.*, 2008). Small apertures in metal films also have the advantage of facilitating parallel assays with multiple aperture structures on a given substrate. Note that in such case, care must be taken to avoid cross talk between the apertures since each one can launch SPPs. The possibility of structuring the metal surface around the aperture to increase the excitation intensity and also beam the emission towards the photo-detector should also be explored (Lezec *et al.*, 2002).

Aperture structures also lend themselves well for integration in microfluidics systems (Sinton *et al.*, 2008), where they can add label free sensor capacity (De Leebeeck *et al.*, 2007; Ji *et al.*, 2008; Lesuffleur *et al.*, 2008; Sharpe *et al.*, 2008). The combination of optical contrast and simplicity of the transmission mode is particularly suited for analyzing rapidly small volumes at a given location in the high throughput of such systems. In addition, the ability to tailor the SPP resonance (wavelength, polarization sensitivity, etc) to obtain signal enhancements should enable the measurement of various spectroscopic signals and boost the screening capacity as the analyte progresses in the channels. Finally, optical trapping by single holes or hole arrays could create new opportunities for on-chip integration and sensing (Sinton *et al.*, 2008).

B. Photonic Devices and Methods

Perhaps the simplest application of aperture structures is as filters and polarizing elements (Genet and Ebbesen, 2007). Periodic arrays have well defined resonances that can be tuned with geometrical parameters (lattice symmetry, period, hole shape) and that can be changed by simply changing the relative angle of the filter to the incident beam. Such structures can also be made to act as polarizing filters by lowering the symmetry at the level of the holes and/or the arrays, as discussed in sections III.B.4 and III.B.7. Appropriately designed aperture structures can also act as waveplates to change the state of polarization of light (Drezet *et al.*, 2008). On the other hand, the large polarization anisotropy combined with the peak shifts induced by the high aspect ratios in arrays of rectangular holes (as discussed in section III.B.4) can be exploited to generate structures of which the color of the emitted light can be tuned through a modulation of the polarization (DiMaio and Ballato, 2006). These color filters and polarization elements have the advantage of being robust to high laser powers as long as the metal absorption is negligible at the wavelength of interest.

Such features have stimulated quite a few studies to use aperture structures in lasers, in particular in vertical-cavity-surface-emitting lasers (VCSELs) (Guo *et al.*, 2007a, 2008; Hashizume and Koyama, 2004; Ohno *et al.*, 2007; Onishi *et al.*, 2007; Shinada *et al.*, 2003). While single resonant apertures can provide a very small bright subwavelength laser beam, multiple apertures structures with polarization selectivity can stabilize and control the polarization output angle of VCSEL's. As a consequence, several VCSELs on the same chip can be operated in parallel and coupled to one optical fiber opening new possibilities for polarization multiplexing (Hashizume and Koyama, 2007; Onishi *et al.*, 2007). Considerable amount of light remains trapped in light emitting diodes (LEDs), whether inorganic or organic, due to the high refractive index of the materials. In addition, conductive electrodes are necessary on both sides of the LEDs for current injection purposes which can add to the problem. The light emitted by the diode can couple to SPPs in the electrode which are then damped in the metal unless scattered out and decoupled into freely propagating light. If an array of apertures are engraved in the electrodes, the electrode can still serve it is original function but also provide an outcoupling mechanism of the SPPs and the trapped light as has been demonstrated for organic LEDs (Hsu *et al.*, 2008; Liu *et al.*, 2005, 2004). Such results are very promising and need to be tested for inorganic LEDs which remain the major product on the market.

Just as photoemitters, photodetectors can also benefit from incorporating metallic apertures (Collin *et al.*, 2003, 2004; Ishi *et al.*, 2005a; Laux *et al.*, 2008). Corrugated metal surfaces can act as resonant antennas to capture the incoming light which can then be transmitted through one or more apertures to the photovoltaic elements. Smaller photovolatic elements can therefore be used to capture the same amount of light which reduces the impedance of the device and thereby increases the operational speed, which should be particularly beneficial for silicon based technology where such miniature photodetectors could be used for clocking purposes (Ishi *et al.*, 2005b). Recently it was also demonstrated that interdigitated metallic corrugations could also be used to separate different wavelengths of light impinging on the surface which are then transmitted through individual apertures as illustrated in Fig. 54. This photon-sorting capacity appears very promising for spectral and polarimetric imaging (Laux *et al.*, 2008).

Ever since it was shown that light could be beamed from a subwavelength aperture by texturing the output surface of the metal surrounding the opening (Garcia-Vidal *et al.*, 2003b; Lezec *et al.*, 2002; Martin-Moreno *et al.*, 2003)), the possibility of using such structures as novel kind of lenses and multiplexing devices has been the subject of many studies (Beruete *et al.*, 2004a; Caglayan *et al.*, 2006a; Chang *et al.*, 2006; Chen *et al.*, 2006; Feng and Dawson, 2007; Hendry *et al.*, 2008, 2007; Huang *et al.*, 2007a; Kim *et al.*, 2007, 2008; Min *et al.*, 2008; Shi *et al.*, 2007). The profile of the beam emerging from

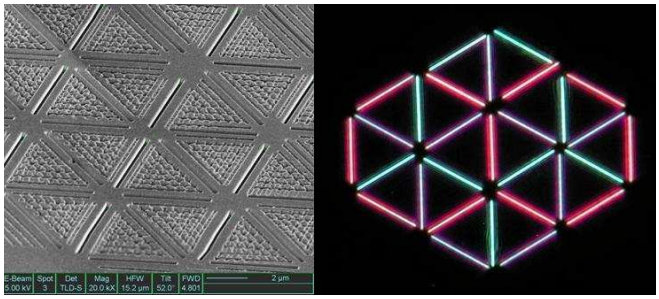

FIG. 54 Left: SEM image of a triangular lattice of slits fabricated by FIB in a Au film. Inside each triangle, gratings with different periods to couple light of different wavelengths are superimposed. Each grating selectively send the resonating colour to a slit where it is transmitted to the opposite side. Right: far-field image of the light emerging from the structure on the left. (Image courtesy of Eric Laux)

the surface is sensitive to the various modes present and the scattering of the electromagnetic waves in the structure. Even quasi-periodic arrays can lead to focusing (Huang *et al.*, 2007b). The addition of all optical control by resonant excitation (Hendry *et al.*, 2008) or by adding a non-linear material (Min *et al.*, 2008) allows for further beam control. More generally, it has been shown that the transmission through aperture arrays can be controlled optically using bistable materials (Porto *et al.*, 2004; Wurtz *et al.*, 2006) and molecular excited states (Dintinger *et al.*, 2006b), electrically with liquid crystals (Dickson *et al.*, 2008; Kim *et al.*, 1999) and semiconductors (Shaner *et al.*, 2007), and acoustically (Gerard *et al.*, 2007). Such control is possible because the SPP resonances which give rise to the EOT are very sensitive to the refractive index at the metal surface which is modified in these processes. The transmission of hole arrays has also been switched directly by optical femtosecond pumping into the interband transitions of Au films (Halte *et al.*, 2005) which modifies momentarily the dielectric function of the metal and thereby the surface plasmon resonances. The transmission (filter) switching speeds that have been demonstrated reach terahertz frequencies using all optical control (Dintinger *et al.*, 2006b).

The realization of surface plasmonic miniature photonic circuits will require, among other things, efficient surface plasmon launchers (Ebbesen *et al.*, 2008). Hole arrays and individual apertures have been used to generate SPP beams at a metal surface (Baudrion *et al.*, 2008; Devaux *et al.*, 2003; Kihm *et al.*, 2008; Kim *et al.*, 2003). The shape of the SPP beam can be controlled by the disposition of the holes in the array (Laluet *et al.*, 2007) or by texturing the metal surface near the aperture (Lopez-Tejeira *et al.*, 2007). The exact configuration will depend on the application but one of the advantages of the aperture structures is the coupling of light to SPPs via backside illumination thereby avoiding parasitic light and noise.

From the very beginning, it was quite clear that the

EOT process had potential for achieving subwavelength lithography when one considered the subwavelength dimensions of the apertures and the high contrast the optically thick metal films provided. Such lithography mask would be activated by periodic corrugations with apertures only at desired locations. Naturally it will have however only work in the near or proximate field. Such sub-diffraction lithography with sub-100 nm features has been demonstrated using a variety of conditions (Alkaisi *et al.*, 1999; Chang *et al.*, 2007a; Luo and Ishihara, 2004; Schellenberg *et al.*, 2005; Seo *et al.*, 2007; Shao and Chen, 2005, 2008; Srituravanich *et al.*, 2004; Wei *et al.*, 2007) and could be an alternative to the complex and costly modern projection lithographic techniques.

VI. CONCLUSIONS AND PERSPECTIVES

From what has been presented in the previous pages, it should be clear that much insight has been gained over the past decade into the optics of subwavelength apertures in metal films which has found applications in a variety of areas. The contributions of various optical modes to the transmission process resulting in high local EM fields which more than offset the attenuation by the cutoff function of the apertures have been identified. The transmission can be tailored and optimized for a given need by an appropriate choice of geometrical and material parameters.

Maximizing the electric fields at a given location on and/or off the surface can still benefit from further work. Shaping the electrical fields on multiple length scales is expected to be of significant interest for various applications. For instance for cold atom research (Alloschery *et al.*, 2006), the simultaneous manipulation of a large number of optical traps, all aspects of light fields near subwavelength apertures will be important, as the traps have to be situated at a suitable distance from the metal surfaces to prevent heating of the atoms through an interaction with the Fermi electrons. In an alternative approach, it has been demonstrated theoretically that the EOT phenomenon can be applied to matter waves to manipulate cold atoms such as Bose Einstein condensates (Fernandez-Dominguez *et al.*, 2006; Moreno *et al.*, 2005), which again would require tailoring the EM fields in and around the apertures.

Furthermore, the use of nonlinear interactions to switch the fields in the vicinity of the apertures will allow a high degree of spatio-temporal control of electrical fields, which is both of fundamental and applied interest. It is anticipated that coherent control, with or without learning algorithms, will play an important role to achieve the desired spatio-temporal control. By all-optical switching of the transmission through subwavelength apertures, not only the amplitude but also polarization properties may be efficiently modified on femtosecond time scales thereby enabling an ultrafast control of electromagnetic fields. This will allow for time-controlled filters, as already demonstrated at terahertz rates (Dintinger *et al.*, 2006b) but also time-dependent coupling to plasmonic circuitry (Ebbesen *et al.*, 2008). More efforts on the texturing the output surface around apertures could lead to miniature photonic devices with dynamic steering and mulitplexing capacity.

The combination of several hole arrays can also lead to improved capabilities and new properties. Already cascading two hole arrays in the path of the light beam can lead to increased transmission as compared to a single array due to interlayer coupling (Ye and Zhang, 2005). The transmission can be very strong even when no direct line of sight exists between the apertures in the layers (Chan *et al.*, 2006; Teeters-Kennedy *et al.*, 2007). The opto-magnetic response and the left-handed behavior of such stacks have also been analyzed in detail (Beruete *et al.*, 2007a,b; Li *et al.*, 2006, 2007). Such results suggest further exploration of the metamaterial like behavior of coupled aperture structures.

Finally we anticipate much research activity from the transfer and application of the EOT phenomenon to other domains. As discussed above, the EOT process can be applied to matter waves for the realization of aperture based optical elements which should be ideally suited for beams of atoms or other particles (Moreno *et al.*, 2005). Introducing such elements in a cold atom setup will not be trivial but the potential seems well worth it. Giant transmissions are also observed for perforated films involving surface phonon polaritons (Korobkin *et al.*, 2007). The acoustic equivalent of the EOT process has received much attention recently (Cai *et al.*, 2007; Christensen *et al.*, 2007, 2008; Estrada *et al.*, 2008; Lu. *et al.*, 2007; Mei *et al.*, 2008; Zhou and Kriegsmann, 2007). Beyond the interesting fundamental aspects, the applications to acoustics open numerous possibilities from sound insulation to beaming which could rapidly find practical use.

As stated earlier, the potential of metallic aperture structures lies in the high contrast and high local fields they provide and in the simplicity of their implementation. The capacity to further texture the metal around the apertures adds another important element which has not yet been completely evaluated. It is therfore expected that this will not only improve existing applications but also expand them. Overall, many developments can be expected in the years to come whether in optics or in other domains as properties of aperture structures are fully explored.

Acknowledgements

APPENDIX A: Modal expansion formalism

In this appendix we describe the details of the modal expansion framework presented in section I.B, which has been used in this review paper to describe the light transmission through subwavelength apertures.

By denoting with z the direction normal to the film, we take the metal-dielectric interfaces to be located at $z = 0$ and $z = h$. We assume a rectangular supercell, with lattice parameters L_x and L_y, along the x and y axis, respectively (see Fig.2). This supercell may be real (if we are considering an infinitely periodic system) or artificial, if the system is finite. In this latter case, the limit $L_x, L_y \to \infty$ must be taken.

First, we analyze the expansion of the EM fields in the three different regions (reflection, perforated metal and transmission) defining the structure. For a incident plane wave with parallel wavevector $\vec{k}_0$ and polarization σ_0, the parallel components of the EM fields at $z = 0^-$ (at the metal interface in which radiation is impinging on) can be written, in terms of the reflection coefficients $r_{\vec{k}\sigma}$, as:

$$|\vec{E}(z=0^-)> \;=\; |\vec{k}_0\sigma_0> + \sum_{\vec{k}\sigma} r_{\vec{k}\sigma}|\vec{k}\sigma> \qquad \text{(A1)}$$

$$-\vec{u}_z \times |\vec{H}(z=0^-)> \;=\; Y_{\vec{k}_0\sigma_0}|\vec{k}_0\sigma_0> - \sum_{\vec{k}\sigma} r_{\vec{k}\sigma} Y_{\vec{k}\sigma}|\vec{k}\sigma>,$$

where we have used a Dirac notation, and expressed the bi-vectors $< \vec{r}|\vec{E} >= \vec{E}(\vec{r}) = (E_x(\vec{r}), E_y(\vec{r}))^T$ and $\vec{H} = (H_x, H_y)^T$ (T standing for transposition) in terms of the EM plane wave eigenmodes, $|\vec{k}\sigma>$. The expressions for these eigenmodes in real space are:

$$< \vec{r}|\vec{k}p> \;=\; (k_x, k_y)^T \exp(\imath\vec{k}\vec{r})/\sqrt{L_x L_y |k|^2} \qquad \text{(A2)}$$
$$< \vec{r}|\vec{k}s> \;=\; (-k_y, k_x)^T \exp(\imath\vec{k}\vec{r})/\sqrt{L_x L_y |k|^2}.$$

These modes are orthonormal when integrated over a unit cell, i.e. $< \vec{k}\sigma|\vec{k}'\sigma' >= \delta_{\vec{k},\vec{k}'}\delta_{\sigma,\sigma'}$, where δ is the Kronecker delta. The electric and magnetic fields in Eqs. (A1) are related through the admittances $Y_{\vec{k}s} = k_z/k_\omega$ and $Y_{\vec{k}p} = \epsilon_1 k_\omega/k_z$ (for s- and p- polarization, respectively), where $k_\omega = \omega/c$ (ω is the frequency and c the speed of light) and $|k|^2 + k_z^2 = k_\omega^2$. Notice that, according to Bloch's theorem, $\vec{k} = \vec{k}_0 + \vec{k}_R$, $\vec{k}_R$ being a (supercell) reciprocal lattice vector.

In a similar way, in the region of transmission, the EM fields at $z = h^+$ can be expressed as a function of the transmission amplitudes, $t_{\vec{k}\sigma}$, as

$$|\vec{E}(z=h^+)> \;=\; \sum_{\vec{k}\sigma} t_{\vec{k}\sigma}|\vec{k}\sigma> \qquad \text{(A3)}$$
$$-\vec{u}_z \times |\vec{H}(z=h^+)> \;=\; \sum_{\vec{k}\sigma} t_{\vec{k}\sigma} Y_{\vec{k}\sigma}|\vec{k}\sigma>$$

For the modal expansion of the EM fields within the indentations, we use a compact notation by denoting with "object" α to any waveguide EM mode considered in the expansion. Therefore, an object is characterized by the indentation it belongs to, by its polarization (TM or TE modes) and by the indexes related to its mode spatial dependence. All that needs to be known are the electric field bivectors, $|\alpha>$, and the propagation constants, $q_{z\alpha}$, associated with the object. For indentations with simple cross sections as slits or rectangular and circular holes, the required expressions for $|\alpha>$ and $q_{z\alpha}$ can be found analytically. As in the case of the plane waves, the magnetic field can be related to the electric field bivector as $-\vec{u}_z \times |\vec{H}>_\alpha = \pm Y_\alpha|\alpha>$, with the admittance, Y_α, being $Y_\alpha = q_{z\alpha}/k_\omega$ for TE modes, while for TM modes $Y_\alpha = k_\omega/q_{z\alpha}$. Then, the electric and magnetic fields inside the indentations can be written in terms of the expansion coefficients A_α, B_α as:

$$|\vec{E}(z)> \;=\; \sum_\alpha |\alpha> \left[A_\alpha e^{\imath q_{z\alpha} z} + B_\alpha e^{-\imath q_{z\alpha} z}\right] \qquad \text{(A4)}$$
$$-\vec{u}_z \times |\vec{H}(z)> \;=\; \sum_\alpha |\alpha> Y_\alpha \left[A_\alpha e^{\imath q_{z\alpha} z} - B_\alpha e^{-\imath q_{z\alpha} z}\right]$$

The way to extract the complete set of unknowns $\{A_\alpha, B_\alpha, t_{\vec{k}'\sigma}, r_{\vec{k}\sigma}\}$ is by matching the EM fields appropriately at the two horizontal interfaces ($z = 0$ and $z = h$). The parallel components of the electric field must be continuous over the whole surface whereas the magnetic field counterparts are continuous only over the apertures. As we can not consider the infinite number of modes in the structure (i.e., the sums in Eqs.(A1-A4) must be truncated), these matching relations can not be fulfilled at every point, so the matching procedure should not be done in real space. Instead, in the truncated Hilbert space, the correct procedure is to project each matching equation onto the set of modes which spans the spatial region over which the equation is defined. Hence, continuity of the E-field components should be expanded onto plane waves ($< \vec{k}\sigma|$) and the ones related to the H-field should be project onto waveguide modes $< \alpha|$. After this matching procedure, we end-up with a system of linear equations for the expansion coefficients, $\{A_\alpha, B_\alpha\}$. It is convenient to define the related quantities, $E_\alpha \equiv A_\alpha + B_\alpha$ and $E'_\alpha \equiv -(A_\alpha e^{\imath q_{z\alpha} h} + B_\alpha e^{-\imath q_{z\alpha} h})$, which are the modal amplitudes of the E-field at the input and output interfaces of the indentations, respectively. The set $\{E_\alpha, E'_\alpha\}$ satisfies:

$$(G_{\alpha\alpha} - \Sigma_\alpha)E_\alpha + \sum_{\beta\neq\alpha} G_{\alpha\beta}E_\beta - G^V_\alpha E'_\alpha \;=\; I_\alpha$$
$$(G'_{\gamma\gamma} - \Sigma_\gamma)E'_\gamma + \sum_{\nu\neq\gamma} G'_{\gamma\nu}E'_\nu - G^V_\gamma E_\gamma \;=\; 0 \qquad \text{(A5)}$$

This is the basic set of linear equations [in the main text, Eqs.(1)] used throughout this review article to describe the transmission properties of different structures containing subwavelength apertures. The different terms appearing in these "tight-binding" like equations have the following mathematical expressions. The illumination term, I_α, is proportional to the overlap integral between object α and the incident plane wave:

$I_\alpha = 2iY_{\vec{k}_0\sigma_0} < \vec{k}_0\sigma_0|\alpha >$. Σ_α is related to the bouncing back and forth of the EM-fields inside object α and for an aperture its expression is $\Sigma_\alpha = Y_\alpha/\tan(q_{z\alpha}h)$. In the case in which the indentation does not completely trespass the metal (a dimple in 2D or a groove in 1D), the expression for Σ_α is the same but h is replaced by the depth of the indentation. The coupling between the two sides of the aperture is accounted for $G_\alpha^V = Y_\alpha/\sin(q_{z\alpha}h)$. In the case of a waveguide mode α associated with a dimple or a groove, $G_\alpha^V = 0$ leading to $E'_\alpha = 0$.

The term $G_{\alpha\beta}$ controls the EM-coupling between objects α and β:

$$G_{\alpha\beta} = i\sum_{\vec{k}\sigma} Y_{\vec{k}\sigma} < \alpha|\vec{k}\sigma >< \vec{k}\sigma|\beta > \tag{A6}$$

where the overlap $< \alpha|\vec{k}\sigma >$ involves the evaluation of an integral in real space:

$$< \alpha|\vec{k}\sigma >= \int d\vec{r} < \alpha|\vec{r} >< \vec{r}|\vec{k}\sigma > \tag{A7}$$

If the system is periodic, $G_{\alpha\beta}$ can be easily calculated through the previous discrete sum [Eq.(A6)], by including enough diffraction waves.

Within the modal expansion formalism, the finite dielectric function of a real metal can be incorporated in an approximated way by means of the surface impedance boundary conditions (SIBC). The important point of this approach is that the system of linear equations (A5) still holds, only the different magnitudes appearing on it differ from their PEC values:

$$\begin{aligned} I_\alpha &= \frac{2iY_{\vec{k}_0\sigma_0} < \vec{k}_0\sigma_0|\alpha >}{1 + Z_S Y_{\vec{k}_0\sigma_0}} \\ \Sigma_\alpha &= iY_\alpha \frac{e^{iq_{z\alpha}h}(1+Z_SY_\alpha) + e^{-iq_{z\alpha}h}(1-Z_SY_\alpha)}{e^{iq_{z\alpha}h}(1+Z_SY_\alpha)^2 - e^{-iq_{z\alpha}h}(1-Z_SY_\alpha)^2} \\ G_\alpha^V &= \frac{2iY_\alpha}{e^{iq_{z\alpha}h}(1+Z_SY_\alpha)^2 - e^{-iq_{z\alpha}h}(1-Z_SY_\alpha)^2} \end{aligned} \tag{A8}$$

where $Z_S = 1/\sqrt{\epsilon_M(\omega)}$ is the surface impedance of the metal. As in the PEC case, the expression for Σ_α for a dimple or a groove is the same but h must be replaced by the depth of the indentation. The coupling term, $G_{\alpha\beta}$, also depends on Z_S:

$$G_{\alpha\beta} = i\sum_{\vec{k}\sigma} \frac{Y_{\vec{k}\sigma}}{1 + Z_S Y_{\vec{k}\sigma}} < \alpha|\vec{k}\sigma >< \vec{k}\sigma|\beta > \tag{A9}$$

Let us now describe how to evaluate the different two-media scattering coefficients as depicted in Fig. 3 by using the modal expansion formalism. By applying a matching procedure equivalent to that used for obtaining the set of Eqs.(A5), we can relate the different two-media scattering coefficients with those magnitudes appearing in the general set of Eqs.(A5). For example, for the scattering process depicted in Fig.3(a), we obtain the following set of equations for the different τ_α^{12}:

$$(G_{\alpha\alpha} + iY_\alpha)\tau_\alpha^{12} + \sum_{\beta\neq\alpha} G_{\alpha\beta}\tau_\beta^{12} = I_\alpha \tag{A10}$$

From them, it is then possible to extract the reflection coefficients associated with the interface I-II, $\rho_{\vec{k}\sigma}^{12}$:

$$\rho_{\vec{k}\sigma}^{12} = -\delta_{\vec{k}\vec{k}_0}\delta_{\sigma\sigma_0} + \sum_\alpha < \vec{k}\sigma|\alpha > \tau_\alpha^{12} \tag{A11}$$

The second two-media scattering problem is schematically depicted in Figure 3(b). The matching of the parallel components of the EM fields leads to a system of linear equations for $\rho_{\alpha\beta}^{23}$:

$$(G'_{\gamma\gamma} + iY_\gamma)\rho_{\alpha\gamma}^{23} + \sum_{\beta\neq\gamma} G'_{\gamma\beta}\rho_{\alpha\beta}^{23} = iY_\gamma\delta_{\gamma\alpha} - G'_{\gamma\alpha} \tag{A12}$$

The transmission coefficients in medium III can be extracted from the knowledge of $\{\rho_{\alpha\beta}^{23}\}$ by means of

$$\tau_{\alpha,\vec{k}\sigma}^{23} =< \vec{k}\sigma|\alpha > + \sum_\beta \rho_{\alpha\beta}^{23} < \vec{k}\sigma|\beta > \tag{A13}$$

The procedure for extracting the two-media coefficients associated with the II-I scattering problem is completely equivalent to that of the II-III previously discussed.

Up to this point, we have described the theoretical framework able to deal with infinite periodic structures (2D arrays of holes or 1D arrays of slits). The only difference between infinite and finite structures resides in the calculation of $G_{\alpha\beta}$ (the rest of the magnitudes appearing in Eqs.(A5) are the same). When treating a finite set of indentations, the limit $L_x, L_y \to \infty$ must be taken. In this way, $G_{\alpha\beta}$ is calculated by means of an integral over diffraction modes:

$$G_{\alpha\beta} = i\frac{L_xL_y}{(2\pi)^2}\sum_\sigma \int d\vec{k} \frac{Y_{\vec{k}\sigma}}{1 + Z_S Y_{\vec{k}\sigma}} < \alpha|\vec{k}\sigma >< \vec{k}\sigma|\beta > \tag{A14}$$

where the expression for a PEC can be obtained from (A14) by simply putting $Z_S = 0$. In Eq.(A14), the integration is over all possible $\vec{k}$ (in-plane components of the wavevector) and the factor L_xL_y cancels out with that coming from the normalization of the EM plane waves. Alternatively, $G_{\alpha\beta}$ can be calculated as a double integral in real space using the expression:

$$G_{\alpha\beta} \equiv < \alpha|\hat{G}|\beta >= \int\int d\vec{r}d\vec{r}' < \alpha|\vec{r} > \hat{G}(\vec{r},\vec{r}') < \vec{r}'|\beta > \tag{A15}$$

where $\hat{G}(\vec{r},\vec{r}')$ is related to the Green's dyadic tensor in a metal-dielectric interface whose formal expression can be extracted by comparing Eq.(A15) with Eq.(A14):

$$\hat{G}(\vec{r},\vec{r}') = \frac{iL_xL_y}{(2\pi)^2}\int d\vec{k}\frac{Y_{\vec{k}\sigma}}{1+Z_SY_{\vec{k}\sigma}} < \vec{r}|\vec{k}\sigma >< \vec{k}\sigma|\vec{r}' > \tag{A16}$$

Thus, the dyadic $\hat{G}(\vec{r},\vec{r}')$ controls the EM coupling between apertures. In order to illustrate its spatial dependence, let us concentrate in the case of 1D geometries illuminated by p-polarized light (and with zero component of the incident wavevector along the axis of symmetry of the structure). The Green's dyadic tensor for the 2D case (holes) is more complex and further details on how to calculate it can be found in (Bravo-Abad *et al.*, 2004a). The 1D Green's function for p-polarized light within the SIBC approach, $G(x,x')$, can be written as:

$$G(x,x') = \frac{i}{2\pi}\int_{-\infty}^{\infty} dk\frac{k_w}{\sqrt{k_w^2-k^2}+Z_S}e^{ik(x-x')} \tag{A17}$$

It is worth noticing that the corresponding expression for a PEC [$Z_S=0$ in Eq.(A17)] can be analytically evaluated and is related to the zero-order Hankel function of the first kind, $H_0^{(1)}$:

$$G^{PEC}(x,x') = \frac{i\pi}{\lambda}H_0^{(1)}(k_w|x-x'|) \tag{A18}$$

It is interesting to compare the behavior of the 1D Green's dyadic function for a real metal [Eq.(A17)] with that of a PEC, Eq.(A18). As a difference with the PEC case, $G(x,x')$ must be calculated numerically. For a good metal (silver or gold), however, this integral is dominated by the single pole of the integrand, due to the presence of SPPs (recall that, within SIBC approach, the dispersion relation of SPPs reads $k_z=-Z_Sk_\omega$, i.e., $k_{SPP}=k_\omega\sqrt{1-Z_S^2}$). Isolating the contribution from the pole gives an approximation to $G(x,x')$:

$$G^{SPP}(x,x') = -\frac{Z_S}{\sqrt{1-Z_S^2}}k_\omega^2 e^{ik_{SPP}|x-x'|} \tag{A19}$$

The behavior of the 1D Green's dyadic function is illustrated in Fig.55, which renders $G(x,x')$ for silver at $\lambda=600$nm. Together with the exact numerical evaluation of Eq.(A17), we also present the calculation for a PEC [Eq.(A18)] and the "asymptotic" expression, G^{SPP} as obtained from Eq.(A19). As Fig. 55 shows, the exact $G(x,x')$ resembles the PEC result at very small distances $|x-x'|\ll\lambda$ and is well approximated by G^{SPP} for $|x-x'|\geq 2\lambda$.

The formulation in real space previously described could also be used to compute the optical properties of an infinite periodic system. In this case, we know that the modal coefficients must satisfy Bloch's theorem,

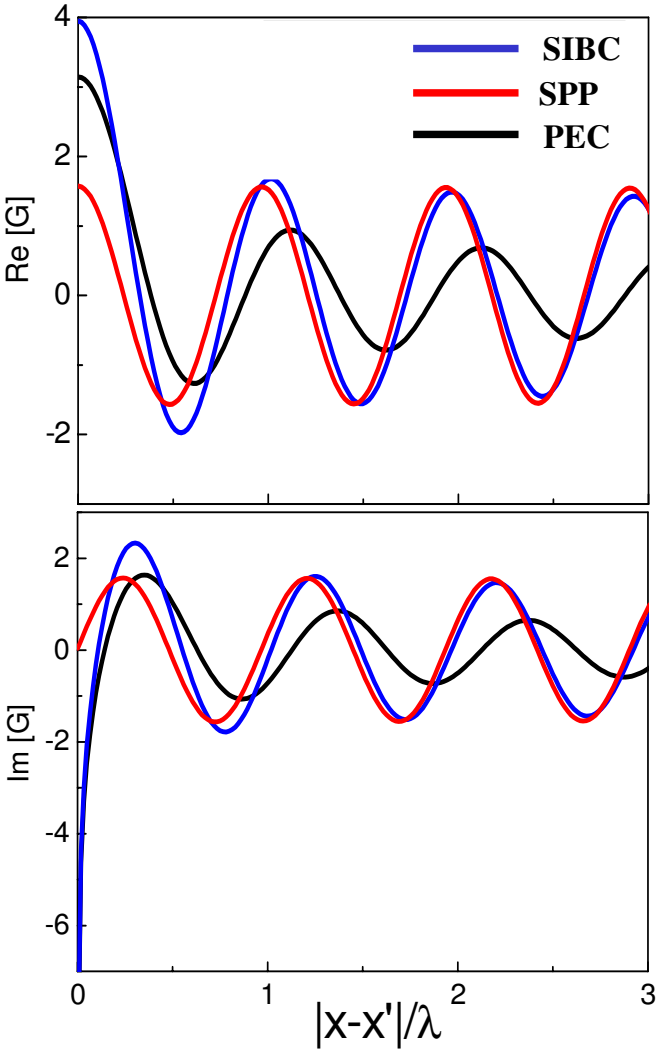

FIG. 55 1D Green's dyadic function (real and imaginary parts) for a metal-vacuum interface for p-polarized light of $\lambda=600$nm. The blue curves corresponds the SIBC approach [Eq.(A17)] whereas the black curves are for a PEC [Eq.(A18)]. The red curves display the SPP contribution to G, as given by Eq.(A19).

$E_\alpha(\vec{R}_n)=E_\alpha e^{i\vec{k}_0\vec{R}_n}$. Then, the coupling term between Bloch's modes α and β can be evaluated in real space as a sum over lattice locations:

$$G_{\alpha\beta} = \sum_{\vec{R}_m} G_{\alpha\beta}^{\vec{R}n\vec{R}_m} e^{i\vec{k}_0(\vec{R}_m-\vec{R}_n)} \tag{A20}$$

where $G_{\alpha\beta}^{\vec{R}_n\vec{R}_m}$ is the EM coupling between waveguide mode α of hole located at $\vec{R}_n$ and waveguide mode β belonging to a hole placed in $\vec{R}_m$: $G_{\alpha\beta}^{\vec{R}_n\vec{R}_m} =< \alpha(\vec{R}_n)|\hat{G}|\beta(\vec{R}_m) >$. Of course, expression (A20), which involves sums of difficult Sommerfeld integrals, is numerically much more complicated than Eq.(A6). However, Eq.(A20) is valuable as it sheds light on the origin of

the divergencies of $G_{\alpha\beta}$: they originate from constructive sums of re-illumination processes of light coming from other holes (Bravo-Abad *et al.*, 2004a; De Abajo and Saenz, 2005).

References

Adam, A. J. L., J. M. Brok, M. A. Seo, K. J. Ahn, D. S. Kim, J. H. Kang, Q. H. Park, M. Nagel, and P. C. M. Planken, 2008, Opt. Express **16**, 7407.

Agrawal, A., H. Cao, and A. Nahata, 2005, Opt. Express **13**, 3535.

Agrawal, A., and A. Nahata, 2006, Opt. Express **14**, 1973.

Airola, M., Y. Liu, and S. Blair, 2005, J. Opt. A-Pure and Applied Optics **7**, S118.

Akarca-Biyikli, S. S., I. Bulu, and E. Ozbay, 2004, Appl. Phys. Lett. **85**, 1098.

Alkaisi, M. M., R. B. Blaikie, S. J. McNab, R. Cheung, and D. R. S. Cumming, 1999, Appl. Phys. Lett. **75**, 3560.

Alloschery, O., R. Mathevet, J. Weiner, and H. J. Lezec, 2006, Opt. Express **14**, 12568.

Altewischer, E., M. P. van Exter, and J. P. Woerdman, 2002, Nature **418**, 304.

Altewischer, E., M. P. van Exter, and J. P. Woerdman, 2003, J. Opt. Soc. Am. B **20**, 1927.

Altewischer, E., M. P. van Exter, and J. P. Woerdman, 2005a, J. Opt. Soc. Am. B **22**, 1731.

Altewischer, E., M. P. van Exter, and J. P. Woerdman, 2006, New J. Phys. **8**, 57.

Altewischer, E., C. Genet, M. P. van Exter, J. P. Woerdman, P. F. A. Alkemade, A. van Zuuk, and E. W. J. M. van der Drift, 2005b, Opt. Lett. **30**, 90.

Altewischer, E., X. Ma, M. P. van Exter, and J. P. Woerdman, 2005c, Opt. Lett. **30**, 2436.

Altewischer, E., Y. C. Oei, M. P. van Exter, and J. P. Woerdman, 2005d, Phys. Rev. A **72**, 013817.

Astilean, S., P. Lalanne, and M. Palamaru, 2000, Opt. Commun. **175**, 265.

Auckland, D. T., and R. F. Harrington, 1978, IEEE Trans. Microwave Theory Tech. **MTT-26**, 499.

Azad, A. K., Y. G. Zhao, W. L. Zhang, and M. X. He, 2006, Opt. Lett. **31**, 2637.

Baida, F. I., 2007, Appl. Phys. B-Lasers and Optics **89**, 145.

Baida, F. I., and D. Van Labeke, 2002, Opt. Commun. **209**, 17.

Baida, F. I., and D. Van Labeke, 2003, Phys. Rev. B **67**, 155314.

Baida, F. I., D. Van Labeke, A. Moreau, G. Granet, and A. Belkhir, 2004, Appl. Phys. B-Lasers and Optics **79**, 1.

Barbara, A., P. Quemerais, E. Bustarret, and T. Lopez-Rios, 2002, Phys. Rev. B **66**, 161403.

Barnes, W. L., 1998, J. Mod. Optics **45**, 661.

Barnes, W. L., W. A. Murray, J. Dintinger, E. Devaux, and T. W. Ebbesen, 2004, Phys. Rev. Lett. **92**, 107401.

Batulla, A., Y. L. Lu, R. J. Knize, K. Reinhardt, and S. C. Chen, 2007, Opt. Express **15**, 14629.

Baudrion, A.-K., F. de Leon-Perez, O. Mahboub, A. Hohenau, H. Ditlbacher, F. J. Garcia-Vidal, J. Dintinger, T. W. Ebbesen, L. Martin-Moreno, and J. R. Krenn, 2008, Opt. Express **16**, 3420.

Bell, P. M., J. B. Pendry, L. M. Moreno, and A. J. Ward, 1995, Comp. Phys. Commun. **85**, 306.

Beruete, M., I. Campillo, J. S. Dolado, J. E. Rodriguez-Seco, E. Perea, and M. Sorolla, 2004a, IEEE Antennas and Wireless Propagation Lett. **3**, 328.

Beruete, M., I. Campillo, J. E. Rodriguez-Seco, E. Perea, M. Navarro-Cia, I. J. Nunez-Manrique, and M. Sorolla, 2007a, IEEE Microwave and wireless components letters **17**, 831.

Beruete, M., M. Navarro-Cia, M. Sorolla, and I. Campillo, 2007b, Opt. Express **15**, 8215.

Beruete, M., M. Sorolla, I. Campillo, J. S. Dolado, L. Martin-Moreno, J. Bravo-Abad, and F. J. Garcia-Vidal, 2004b, Opt. Lett. **29**, 2500.

Bethe, H., 1944, Phys. Rev. **66**, 163.

Betzig, E., and R. J. Chichester, 1993, Science **262**, 1422.

Betzig, E., and J. K. Trautman, 1992, Science **257**, 189.

Blom, H., L. Kastrup, and C. Eggeling, 2006, Curr. Pharm. Biotech. **7**, 51.

Bouwkamp, C. J., 1950, Philips Res. Rep. **5**, 401.

Bravo-Abad, J., A. Degiron, F. Przybilla, C. Genet, F. J. Garcia-Vidal, L. Martin-Moreno, and T. W. Ebbesen, 2006, Nature Physics **2**, 120.

Bravo-Abad, J., A. I. Fernandez-Dominguez, F. J. Garcia-Vidal, and L. Martin-Moreno, 2007a, Phys. Rev. Lett. **99**, 203905.

Bravo-Abad, J., F. J. Garcia-Vidal, and L. Martin-Moreno, 2003, Photonics and Nanostructures - Fundamentals and Applications **1**, 55.

Bravo-Abad, J., F. J. Garcia-Vidal, and L. Martin-Moreno, 2004a, Phys. Rev. Lett. **93**, 227401.

Bravo-Abad, J., L. Martin-Moreno, and F. J. Garcia-Vidal, 2004b, Phys. Rev. E **69**, 026601.

Bravo-Abad, J., L. Martin-Moreno, F. J. Garcia-Vidal, E. Hendry, and J. Gomez Rivas, 2007b, Phys. Rev. B **76**, 241102(R).

Brolo, A. G., E. Arctander, R. Grodon, and K. L. Kavanagh, 2004a, Nano Lett. **4**, 2015.

Brolo, A. G., R. Gordon, B. Leathem, and K. L. Kavanagh, 2004b, Langmuir **20**, 4813.

Brolo, A. G., S. C. Kwok, M. D. Cooper, M. G. Moffitt, C. W. Wang, R. Gordon, J. Riordon, and K. L. Kavanagh, 2006, J. Phys. Chem. B **110**, 8307.

Brolo, A. G., S. C. Kwok, M. G. Moffit, R. Gordon, J. Riordon, and K. L. Kavanagh, 2005, J. Am. Chem. Soc. **127**, 14936.

Bulu, I., H. Caglayan, and E. Ozbay, 2005, Opt. Lett. **30**, 3078.

Caglayan, H., I. Bulu, and E. Ozbay, 2006a, Microwave and Techn. Lett. **48**, 2491.

Caglayan, H., I. Bulu, and E. Ozbay, 2006b, J. Opt. Soc. Am. B **23**, 419.

Cai, F., F. Liu, Z. He, and Z. Liu, 2007, Appl. Phys. Lett. **91**, 203515.

Cao, H., A. Agrawal, and A. Nahata, 2005, Opt. Express **13**, 763.

Cao, H., and A. Nahata, 2004a, Opt. Express **12**, 1004.

Cao, H., and A. Nahata, 2004b, Opt. Express **12**, 3664.

Cao, Q., and P. Lalanne, 2002, Phys. Rev. Lett. **88**, 574031.

Catrysse, P. B., H. Shin, and S. Fan, 2005, J. Vac. Sci. Technol. B **23**, 2675.

Catrysse, P. B., G. Veronis, H. Shin, J.-T. Shen, and S. Fan, 2006, Appl. Phys. Lett. **88**, 031101.

Chan, H. B., Z. Marcet, K. Woo, D. B. Tanner, D. W. Carr, J. E. Bower, R. A. Cirelli, E. Ferry, F. Klemens, J. Miner, C. S. Pai, and J. A. Taylor, 2006, Opt. Lett. **31**, 516.

Chang, C. K., D. Z. Lin, C. S. Yeh, C. K. Lee, Y. C. Chang, M. W. Lin, J. T. Yeh, and J. M. Liu, 2006, Opt. Lett. **31**, 2341.
Chang, S.-H., S. K. Gray, and G. C. Schatz, 2005, Opt. Express **13**, 3150.
Chang, W. L., P.-H. Tsao, and P.-K. Wei, 2007a, Opt. Lett. **32**, 71.
Chang, Y.-T., T.-H. Chuang, M.-W. Tsai, M.-J. Lai, L.-C. Chen, and S.-C. Lee, 2007b, J. Appl. Phys. **101**, 054305.
Chen, C.-C., 1971, IEEE Trans. Microwave Theory Tech. **19**, 475.
Chen, C.-Y., M.-W. Tsai, T.-H. Chuang, Y.-T. Chang, and S.-C. Lee, 2007a, Appl. Phys. Lett. **91**, 063108.
Chen, D. Z. A., R. Hamam, M. Soljacic, and J. D. Joannopoulos, 2007b, Appl. Phys. Lett. **90**, 181921.
Chen, L., J. T. Robinson, and M. Lipson, 2006, Opt. Express **14**, 12629.
Chen, Z., I. R. Hooper, and J. R. Sambles, 2008, Phys. Rev. B **77**, 161405.
Chowdhury, M. H., J. M. Catchmark, and J. R. Lakowicza, 2007, Appl. Phys. Lett. **91**, 103118.
Christensen, J., A. I. Fernandez-Dominguez, F. de Leon-Perez, L. Martin-Moreno, and F. J. Garcia-Vidal, 2007, Nature Physics **3**, 851.
Christensen, J., L. Martin-Moreno, and F. J. Garcia-Vidal, 2008, Phys. Rev. Lett. **101**, 014301.
Chu, J., T.-J. Wang, J.-T. Yeh, M.-W. Lin, Y.-C. Chang, and J.-K. Wang, 2007, Appl. Phys. A **89**, 387.
Coe, J. V., J. M. Heer, S. Teeters-Kennedy, H. Tian, and K. R. Rodriguez, 2008, Ann. Rev. Phys. Chem. **59**, 179.
Coe, J. V., S. M. Williams, K. R. Rodriguez, S. Teeters-Kennedy, S. A., and F. Hrovat, 2006, Anal. Chem. **78**, 1385.
Collin, R. E., and W. H. Eggimann, 1961, IRE. Trans. on microwave theory and techniq. , 110.
Collin, S., F. Pardo, and J.-L. Pelouard, 2003, Appl. Phys. Lett. **83**, 1521.
Collin, S., F. Pardo, R. Teissier, and J. L. Pelouard, 2001, Phys. Rev. B **63**, 331071.
Collin, S., F. Pardo, R. Teissier, and J. L. Pelouard, 2002, J. Opt. A: Pure Appl. Opt. **4**, S154.
Collin, S., F. Pardo, R. Teissier, and J.-L. Pelouard, 2004, Appl. Phys. Lett. **85**, 194.
Crouse, D., and P. Keshavareddy, 2005, Opt. Express **13**, 7760.
Ctitis, G., P. Patoka, X. Wang, K. Kempa, and M. Giersig, 2007, Nano Lett. **7**, 2926.
Dahlin, A., M. Zach, T. Rindzevius, M. Kall, D. S. Sutherland, and F. Hook, 2005, J. Am. Chem. Soc. **127**, 5043.
Darmanyan, S. A., M. Neviere, and A. V. Zayats, 2004, Phys. Rev. B **70**, 075103.
De Abajo, F. J. G., 2002, Opt. Express **10**, 1475.
De Abajo, F. J. G., 2007, Reviews of Modern Physics **79**, 1267.
De Abajo, F. J. G., R. Gomez-Medina, and J. J. Saenz, 2005, Phys. Rev. E **72**, 016608.
De Abajo, F. J. G., and J. J. Saenz, 2005, Phys. Rev. Lett. **95**, 233901.
De Leebeeck, A., L. K. S. Kumar, V. De Lange, D. Sinton, R. Gordon, and A. G. Brolo, 2007, Anal. Chem. **79**, 4094.
Degiron, A., and T. W. Ebbesen, 2004, Opt. Express **12**, 3694.
Degiron, A., and T. W. Ebbesen, 2005, J. Opt. A: Pure Appl. Opt. **7**, S90.
Degiron, A., H. J. Lezec, W. L. Barnes, and T. W. Ebbesen, 2002, Appl. Phys. Lett. **81**, 4327.
Degiron, A., H. J. Lezec, N. Yamamoto, and T. W. Ebbesen, 2004, Opt. Commun. **239**, 61.
Dennis, M. R., N. I. Zheludev, and F. J. G. de Abajo, 2007, Opt. Express **15**, 9692.
Devaux, E., T. W. Ebbesen, J.-C. Weeber, and A. Dereux, 2003, Appl. Phys. Lett. **83**, 4936.
Dickson, W., G. A. Wurtz, P. R. Evans, R. J. Pollard, and A. V. Zayats, 2008, Nano Lett. **8**, 281.
DiMaio, J. R., and J. Ballato, 2006, Opt. Express **14**, 2380.
Dintinger, J., S. Klein, and T. W. Ebbesen, 2006a, Adv. Mat. **18**, 1267.
Dintinger, J., I. Robel, P. V. Kamat, C. Genet, and T. W. Ebbesen, 2006b, Adv. Mater. **18**, 1645.
Docter, M. W., I. T. Young, O. M. Piciu, A. Bossche, P. F. A. Alkemade, van den Berg P. M., and Y. Garini, 2006, Opt. Express **14**, 9477.
Dogariu, A., A. Nahata, R. A. Linke, L. J. Wang, and R. Trebino, 2002, Appl. Phys. B-Lasers and Optics **74**, S69.
Dogariu, A., T. Thio, L. J. Wang, T. W. Ebbesen, and H. J. Lezec, 2001, Opt. Lett. **26**, 450.
Donev, E. U., J. Y. Suh, F. Villegas, R. Lopez, R. F. Haglund, and L. C. Feldman, 2006, Phys. Rev. B **73**, 201401.
Dragila, R., B. Luther-Davies, and S. Vukovic, 1985, Phys. Rev. Lett. **55**, 1117.
Drexhage, K. H., 1974, Prog. Optics **12**, 165.
Drezet, A., C. Genet, and T. W. Ebbesen, 2008, Phys. Rev. Lett. (in press) .
Dykhne, A. M., A. K. Sarychev, and V. M. Shalaev, 2003, Phys. Rev. B **67**, 1954021.
Ebbesen, T. W., C. Genet, and S. I. Bozhevolnyi, 2008, Physics Today **May issue**, 44.
Ebbesen, T. W., H. J. Lezec, H. F. Ghaemi, T. Thio, and P. A. Wolff, 1998, Nature **391**, 667.
Edel, J. B., M. Wu, B. Baird, and H. G. Craighead, 2005, Biophys. J. **88**, L43.
Eggiman, W. H., and R. E. Collin, 1962, IRE Trans. Microwave Theory Tech. **10**, 528.
Ekinci, Y., H. H. Solak, and C. David, 2007, Opt. Lett. **32**, 172.
Elliott, J., I. I. Smolyaninov, N. I. Zheludev, and A. V. Zayats, 2004, Opt. Lett. **29**, 1414.
Elliott, J., I. I. Smolyaninov, N. I. Zheludev, and A. V. Zayats, 2005, Phys. Rev. B **70**, 233403.
Emerson, D. T., 1997, IEEE Trans. Microwave Theory Tech. **45**, 2267.
Enoch, E., E. Popov, N. M., and R. R., 2002, J. Opt. A: Pure Appl. Opt. **4**, S83.
Estrada, H., P. Candelas, A. Uris, F. Belmar, F. Meseguer, and F. J. G. de Abajo, 2008, Appl. Phys. Lett. **93**, 011907.
van Exter, M., and A. Lagendijk, 1988, Phys. Rev. Lett. **60**, 49.
Fan, W. J., S. Zhang, K. J. Malloy, and S. R. J. Brueck, 2005a, Opt. Express **13**, 4406.
Fan, W. J., S. Zhang, K. J. Malloy, and S. R. J. Brueck, 2005b, J. Vac. Sci. Technol. B **23**, 2700.
Fan, W. J., S. Zhang, B. Minhas, K. J. Malloy, and S. R. J. Brueck, 2005c, Phys. Rev. Lett. **94**, 033902.
Fan, W. J., S. Zhang, N. C. Panoiu, A. Abdenour, S. Krishna, R. M. Osgood, K. J. Malloy, and S. R. J. Brueck, 2006a, Nano Lett. **6**, 1027.
Fan, W. J., S. A. Zhang, K. J. Malloy, S. R. J. Brueck, N. C. Panoiu, and R. M. Osgood, 2006b, Opt. Express **14**, 9570.

Fang, X., Z. Y. Li, Y. B. Long, H. X. Wei, R. J. Liu, J. Y. Ma, M. Kamran, H. Y. Zhao, X. F. Han, and B. R. Zhao, 2007, Phys. Rev. Lett. **99**, 066805.
Fano, U., 1961, Phys. Rev. **124**, 1866.
Farcau, C., and S. Astilean, 2007, J. Opt. A: Pure Appl. Opt. **9**, S345.
Feng, L., and P. Dawson, 2007, Opt. Express **15**.
Fernandez-Dominguez, A. I., F. J. Garcia-Vidal, and L. Martin-Moreno, 2007, Phys. Rev. B **76**, 235430.
Fernandez-Dominguez, A. I., E. Moreno, L. Martin-Moreno, and F. J. Garcia-Vidal, 2006, Phys. Rev. A **74**, 021601(R).
Fong, K. Y., and P. M. Hui, 2006, Appl. Phys. Lett. **89**, 091101.
Colas des Francs, G., D. Molenda, F. U. C., and A. Naber, 2005, Phys. Rev. B **72**, 165111.
Frei, W. R., D. A. Tortorelli, and H. T. Johnson, 2005, Appl. Phys. Lett. **86**, 111114.
Gao, D., W. Chen, and A. Mulchandani, 2007, Appl. Phys. Lett. **90**, 073901.
Gao, H. W., J. Henzie, and T. W. Odom, 2006, Nano Lett. **6**, 2104.
Garcia-Vidal, F. J., H. J. Lezec, T. W. Ebbesen, and L. Martin-Moreno, 2003a, Phys. Rev. Lett. **90**, 213901.
Garcia-Vidal, F. J., and L. Martin-Moreno, 2002, Phys. Rev. B **66**, 1554121.
Garcia-Vidal, F. J., L. Martin-Moreno, H. J. Lezec, and T. W. Ebbesen, 2003b, Appl. Phys. Lett. **83**, 4500.
Garcia-Vidal, F. J., L. Martin-Moreno, E. Moreno, L. K. S. Kumar, and R. Gordon, 2006a, Phys. Rev. B **74**, 153411.
Garcia-Vidal, F. J., L. Martin-Moreno, and J. B. Pendry, 2005a, J. Opt. A: Pure Appl. Opt. **7**, S97.
Garcia-Vidal, F. J., E. Moreno, J. A. Porto, and L. Martin-Moreno, 2005b, Phys. Rev. Lett. **95**, 1.
Garcia-Vidal, F. J., S. G. Rodrigo, and L. Martin-Moreno, 2006b, Nature Physics **2**, 790.
Gay, G., B. V. de Lesegno, R. Mathevet, J. Weiner, H. J. Lezec, and T. W. Ebbesen, 2005, Appl. Phys. B **81**, 871.
Genet, C., M. P. Altewischer, E. van Exter, and J. P. Woerdman, 2005, Phys. Rev. B **71**, 033409.
Genet, C., and T. Ebbesen, 2007, Nature **445**, 39.
Genet, C., M. P. van Exter, and J. P. Woerdman, 2003, Opt. Commun. **225**, 331.
Gerard, D., V. Laude, B. Sadani, A. Khelif, V. L. D., and B. Guizal, 2007, Phys. Rev. B **76**, 235427.
Ghaemi, H. F., T. Thio, D. E. Grupp, T. W. Ebbesen, and H. J. Lezec, 1998, Phys. Rev. B **58**, 6779.
Gomez-Rivas, J., P. H. Janke, C. Bolivar, and H. Kurz, 2005, Opt. Express **13**, 847.
Gomez-Rivas, J., C. Schotsch, P. H. Bolivar, and H. Kurz, 2003, Phys. Rev. B **68**, 201306.
Gordon, R., and A. G. Brolo, 2005, Opt. Express **13**, 1933.
Gordon, R., A. G. Brolo, A. McKinnon, A. Rajora, B. Leathem, and K. L. Kavanagh, 2004, Phys. Rev. Lett. **92**, 037401.
Gordon, R., M. Hughes, B. Leathem, K. L. Kavanagh, and A. G. Brolo, 2005, Nano Lett. **5**, 1243.
Gordon, R., D. Sinton, K. L. Kavanagh, and A. G. Brolo, 2008, Acc. Chem. Res.(in press) .
Groeneveld, G. H. M., R. Sprik, and A. Lagendijk, 1990, Phys. Rev. Lett. **64**, 784.
Gruhlke, R., W. Holland, and D. Hall, 1986, Phys. Rev. Lett. **56**, 2838.
Grupp, D. E., H. J. Lezec, T. W. Ebbesen, K. M. Pellerin, and T. Thio, 2000, Appl. Phys. Lett. **77**, 1569.
Guo, B., G. Song, and L. Chen, 2007a, Appl. Phys. Lett. **91**, 021103.
Guo, B., G. Song, and L. Chen, 2008, Appl. Phys. B **91**, 7.
Guo, G.-P., X.-F. Ren, Y.-F. Huang, C.-F. Li, Z.-Y. Ou, and G.-C. Guo, 2007b, Phys. Lett. A **361**, 218.
Haftel, M. I., C. Schlockermann, and G. Blumberg, 2006, Phys. Rev. B **74**, 235405.
Halte, V., A. Benabbas, L. Guidoni, and J. Y. Bigot, 2005, Phys. Stat. Solidi B-Basic Solid State Physics **242**, 1872.
Han, J. G., A. K. Azad, M. F. Gong, Lu, X. C., and W. L. Zhang, 2007, Appl. Phys. Lett. **91**, 071122.
Harrington, R. F., and D. T. Auckland, 1980, IEEE. Trans. Antennas Prop. **AP-28**, 616.
Hashizume, J., and F. Koyama, 2004, Appl. Phys. Lett. **84**, 3226.
Hashizume, J., and F. Koyama, 2007, Electronics and Communication in Japan **90**, 49.
Hendry, E., F. J. Garcia-Vidal, L. Martin-Moreno, J. Gomez Rivas, M. Bonn, A. P. Hibbins, and M. J. Lockyear, 2008, Phys. Rev. Lett. **100**, 123901.
Hendry, E., M. J. Lockyear, J. Gomez-Rivas, L. Kuipers, and M. Bonn, 2007, Phys. Rev. B **75**, 235305.
Henzie, J., M. Lee, and T. Odom, 2007, Nature Nanotechnology **2**, 549.
Hessel, A., and A. A. Oliner, 1965, Appl. Opt. **4**, 1275.
Hibbins, A. P., I. R. Hooper, M. J. Lockyear, and J. R. Sambles, 2006, Phys. Rev. Lett. **96**, 257402.
Hibbins, A. P., J. R. Sambles, and C. R. Lawrence, 2002, Appl. Phys. Lett. **81**, 4661.
Hibbins, A. P., J. R. Sambles, C. R. Lawrence, and D. M. Robinson, 2001, Appl. Phys. Lett. **79**, 2844.
Hohng, S. C., D. S. Kim, Y. Yoon, V. Malarchuk, C. Lienau, J. W. Park, K. H. Yoo, J. Kim, S. H. Han, and Q. H. Park, 2005, J. Korean Phys. Soc. **46**, S205.
Hohng, S. C., Y. Yoon, D. S. Kim, V. Malarchuk, R. Muller, C. Lienau, J. W. Park, K. H. Yoo, J. Kim, H. Y. Ryu, and Q. H. Park, 2002, Appl. Phys. Lett. **81**, 3239.
Hongo, K., 1971, Elec. Comm. (Japan) **54-B**, 90.
Hooper, I. R., and J. R. Sambles, 2003, Phys. Rev. B **67**, 235404.
Hou, B., Z. H. Hang, W. J. Wen, C. T. Chan, and P. Sheng, 2006, Appl. Phys. Lett. **89**, 131917.
Hsu, S.-Y., M.-C. Lee, K.-L. Lee, and P.-K. Wei, 2008, Appl. Phys. Lett. **92**, 013303.
Huang, C., C. Du, and X. Luo, 2007a, Appl. Phys. Lett. **91**, 143512.
Huang, F. M., N. Zheludev, Y. F. Chen, and de Abajo F. J. G., 2007b, Appl. Phys. Lett. **90**, 091119.
van Hulst, N. F., J. A. Veerman, M. F. Garcia-Parajo, and L. Kuipers, 2000, J. Chem. Phys. **112**, 7799.
Ishi, T., J. Fujikata, K. Makita, T. Baba, and K. Ohashi, 2005a, Jap. J. Appl. Phys. **44**, L364.
Ishi, T., J. Fujikata, and K. Ohashi, 2005b, Jap. J. Appl. Phys. **44**, L170.
Ishihara, K., G. Hatakoshi, T. Ikari, H. Minamide, H. Ito, and K. Ohashi, 2005a, Jap. J. Appl. Phys. **44**, L1005.
Ishihara, K., T. Ikari, H. Minamide, J. Shikata, K. Ohashi, H. Yokoyama, and H. Ito, 2005b, Jap. J. Appl. Phys. **44**, L929.
Ishihara, K., K. Ohashi, T. Ikari, H. Minamide, H. Yokoyama, J. Shikata, and H. Ito, 2006, Appl. Phys. Lett. **89**, 201120.
Jeanmaire, D. L., and R. P. Van Duyne, 1977, J. Electroanal. Chem. **84**, 1.
Ji, J., J. G. O'Connell, D. J. D. Carter, and D. N. Larson,

2008, Anal. Chem. **80**, 2491.
Kashyap, S. C., and M. A. K. Hamid, 1971, IEEE. Trans. Antennas Prop. **AP-19**, 499.
Kats, A. V., M. L. Nesterov, and A. Y. Nikitin, 2005, Phys. Rev. B **72**, 193405.
Kats, A. V., and A. Y. Nikitin, 2004, Phys. Rev. B **70**, 235412.
Keilmann, F., 1981, Infrared Millim. Waves **2**, 1259.
Kihm, H. W., K. G. Lee, D. S. Kim, J. H. Kang, and Q.-H. Park, 2008, Appl. Phys. Lett. **92**, 051115.
Kim, D. S., S. C. Hohng, V. Malyarchuk, Y. C. Yoon, Y. H. Ahn, K. J. Yee, J. W. Park, J. Kim, Q. H. Park, and C. Lienau, 2003, Phys. Rev. Lett. **91**, 143901.
Kim, J. H., and P. J. Moyer, 2006a, Opt. Express **14**, 6595.
Kim, J. H., and P. J. Moyer, 2006b, Appl. Phys. Lett. **89**, 121106.
Kim, S., H. Kim, Y. Lim, and B. Lee, 2007, Appl. Phys. Lett. **90**, 051113.
Kim, S., Y. Lim, H. Kim, J. Park, and B. Lee, 2008, Appl. Phys. Lett. **92**, 013103.
Kim, T. J., T. Thio, T. W. Ebbesen, D. E. Grupp, and H. J. Lezec, 1999, Opt. Lett. **24**, 256.
Koerkamp, K. J. K., S. Enoch, F. B. Segerink, N. F. van Hulst, and L. Kuipers, 2004, Phys. Rev. Lett. **92**, 183901.
Korobkin, D., Y. A. Urzhumov, B. Neuner, Z. Zhang, I. D. Mayergoyz, and G. Shvets, 2007, Appl. Phys. A **88**, 605.
Kramper, P., M. Agio, C. M. Soukoulis, A. Birner, F. Muller, R. B. Wehrspohn, U. Gosele, and V. Sandoghdar, 2004, Phys. Rev. Lett. **92**, 113903.
Krishnan, A., T. Thio, T. J. Kim, H. J. Lezec, T. W. Ebbesen, P. A. Wolff, J. Pendry, L. Martin-Moreno, and F. J. Garcia-Vidal, 2001, Opt. Commun. **200**, 1.
Kumar, L. K. S., and R. Gordon, 2006, IEEE Journal of Selected Topics in Quantum Electronics **12**, 1228.
Lalanne, P., and J. P. Hogonin, 2006, Nature Physics **2**, 551.
Lalanne, P., J. P. Hugonin, S. Astilean, M. Palamaru, and K. D. Moller, 2000, J. Opt. A-Pure and Applied Optics **2**, 48.
Lalanne, P., J. P. Hugonin, and J. C. Rodier, 2005a, Phys. Rev. Lett. **95**, 263902.
Lalanne, P., J. C. Rodier, and J. P. Hugonin, 2005b, J. Opt. A: Pure Appl. Opt. **7**, 422.
Laluet, J.-Y., E. Devaux, C. Genet, T. W. Ebbesen, J.-C. Weeber, and A. Dereux, 2007, Opt. Express **15**, 3488.
Landau, L. D., E. M. Lifshitz, and L. P. Pitaevskii, 1960, *Electrodynamics of Continuous Media* (Pergamon Press).
Landstrom, L., D. Brodoceanu, K. Piglmayer, G. Langer, and D. Bauerle, 2005, Appl. Phys. A **81**, 15.
Laux, E., C. Genet, T. Skauli, and T. W. Ebbesen, 2008, Nature Photonics **2**, 161.
Lee, J. W., M. A. Seo, D. H. Kang, K. S. Khim, S. C. Jeoung, and D. S. Kim, 2007, Phys. Rev. Lett. **99**, 137401.
Lee, J. W., M. A. Seo, D. J. Park, D. S. Kim, C. Lienau, S. C. Jeoung, Q. H. Park, and P. C. M. Planken, 2006a, Opt. Express **14**, 1253.
Lee, K. G., and Q.-H. Park, 2005, Phys. Rev. Lett. **95**, 103902.
Lee, P. S. K., M. P. van Exter, and J. P. Woerdman, 2006b, J. Opt. Soc. Am. B **23**, 134.
Lehman, G. W., 1970, J. Math. Phys. **11**, 1522.
Lesuffleur, A., H. Im, N. C. Lindquist, K. S. Lim, and S.-H. Oh, 2008, Opt. Express **16**, 219.
Lesuffleur, A., L. K. S. Kumar, A. G. Brolo, K. L. Kavanagh, and R. Gordon, 2007a, J. Phys. Chem. C Lett. **111**, 2347.
Lesuffleur, A., L. K. S. Kumar, and R. Gordon, 2007b, Phys. Rev. B **75**, 045423.
Levene, M. J., J. Korlach, S. W. Turner, M. Fouquet, H. G. Craighead, and W. W. Webb, 2003, Science **299**, 682.
Levine, D., and P. J. Steinhardt, 1986, Phys. Rev. B **34**, 596.
Lewis, A., M. Isaacson, A. Harootunian, and A. Murray, 1984, Ultramicroscopy **13**, 227.
Lezec, H. J., A. Degiron, E. Devaux, R. A. Linke, L. Martin-Moreno, F. J. Garcia-Vidal, and T. W. Ebbesen, 2002, Science **297**, 820.
Lezec, H. J., and T. Thio, 2004, Opt. Express **12**, 3629.
Li, L., 1997, J. Opt. Soc. Am. A **14**, 2758.
Li, T., H. Liu, F. M. Wang, Z. G. Dong, S. N. Zhu, and X. Zhang, 2006, Opt. Express **14**, 11155.
Li, Z., K. Aydin, and E. Ozbay, 2007, Appl. Phys. Lett. **91**, 121105.
Li, Z., H. Caglayan, E. Colak, and E. Ozbay, 2008, Appl. Phys. Lett. **92**, 011128.
Lin, D. Z., C. K. Chang, Y. C. Chen, D. L. Yang, M. W. Lin, J. T. Yeh, J. M. Liu, C. H. Kuan, C. S. Yeh, and C. K. Lee, 2006, Opt. Express **14**, 3503.
Lin, D. Z., T. D. Cheng, C. K. Chang, J. T. Yeh, J. M. Liu, C. S. Yeh, and C. K. Lee, 2007, Opt. Express **15**, 2585.
Liu, C., V. Kamaev, and Z. V. Vardeny, 2005, Appl. Phys. Lett. **86**, 143501.
Liu, H., and P. Lalanne, 2008, Nature **452**, 728.
Liu, W. C., and D. P. Tsai, 2002, Phys. Rev. B **65**, 1554231.
Liu, Y., J. Bishop, L. Williams, S. Blair, and J. Herron, 2004, Nanotechnology **15**, 1368.
Liu, Y., and S. Blair, 2003, Opt. Lett. **28**, 507.
Liu, Y., and S. Blair, 2004, Opt. Express **12**, 3686.
Lochbihler, H., 1994, Phys. Rev. B **50**, 4795.
Lockyear, M. J., A. P. Hibbins, J. R. Sambles, and C. R. Lawrence, 2004, Appl. Phys. Lett. **84**, 2040.
Lockyear, M. J., A. P. Hibbins, J. R. Sambles, and C. R. Lawrence, 2005, J. Opt. A: Pure Appl. Opt. **7**, S152.
Lomakin, V., S. Q. Li, and E. Michielssen, 2007, Microwave and Opt. Tech. Lett. **49**, 1554.
López-Tejeira, F., F. J. Garcia-Vidal, and L. Martin-Moreno, 2005, Phys. Rev. B **72**, 161405.
Lopez-Tejeira, F., S. G. Rodrigo, L. Martin-Moreno, F. J. Garcia-Vidal, E. Devaux, T. W. Ebbesen, J. R. Krenn, I. P. Radko, S. I. Bozhevolnyi, M. U. Gonzalez, J.-C. Weeber, and A. Dereux, 2007, Nature Physics **3**, 324.
Lu., M.-H., X.-K. Liu, L. Feng, J. Li, C.-P. Huang, Y.-F. Chen, Y.-Y. Zhu, S.-N. Zhu, and M. N.-B., 2007, Phys. Rev. Lett. **99**, 174301.
Luo, X., and T. Ishihara, 2004, Appl. Phys. Lett. **64**, 4780.
Marquier, F., J. J. Greffet, S. Collin, F. Pardo, and J. L. Pelouard, 2005, Opt. Express **13**, 70.
Marquier, F., K. Joulain, and J. J. Greffet, 2004, Opt. Lett. **29**, 2178.
Martin-Moreno, L., F. J. Garcia-Vidal, H. J. Lezec, A. Degiron, and T. W. Ebbesen, 2003, Phys. Rev. Lett. **90**, 167401.
Martin-Moreno, L., F. J. Garcia-Vidal, H. J. Lezec, K. M. Pellerin, T. Thio, J. B. Pendry, and T. W. Ebbesen, 2001, Phys. Rev. Lett. **86**, 1114.
Mary, A., S. G. Rodrigo, L. Martin-Moreno, and F. J. Garcia-Vidal, 2007, Phys. Rev. B **76**, 195414.
Masson, J. B., and G. Gallot, 2006, Phys. Rev. B **73**, 121401.
Matsui, T., A. Agrawal, A. Nahata, and Z. V. Vardeny, 2007, Nature **446**, 517.
Matsui, T., Z. V. Verdeny, A. Agrawal, A. Nahata, and R. Menon, 2006, Appl. Phys. Lett. **88**, 071101.

Mei, J., B. Hou, M. Ke, S. Peng, H. Jia, Z. Liu, J. Shi, W. Wen, and P. Sheng, 2008, Appl. Phys. Lett. **92**, 124106.
Min, C., P. Wang, X. Jiao, Y. Deng, and H. Ming, 2008, Appl. Phys. B **90**, 97.
Min, C. J., P. Wang, X. J. Jiao, Y. Deng, and H. Ming, 2007, Opt. Express **15**, 12368.
Mitsuishi, A., Y. Otsuka, S. Fujita, and H. Yoshinaga, 1963, Jpn. J. Appl. Phys. **2**, 574.
Miyamaru, F., and M. Hangyo, 2004, Appl. Phys. Lett. **84**, 2742.
Miyamaru, F., and M. Hangyo, 2005, Phys. Rev. B **71**, 165408.
Miyamaru, F., T. Kondo, T. Nagashima, and M. Hangyo, 2003, Appl. Phys. Lett. **82**, 2568.
Miyamaru, F., M. Tanaka, and M. Hangyo, 2006a, Phys. Rev. B **74**, 153416.
Miyamaru, F., M. Tanaka, and M. Hangyo, 2006b, Phys. Rev. B **74**, 115117.
Moerland, R. J., N. F. van Hulst, H. Gersen, and L. Kuipers, 2004, Opt. Express **13**, 1604.
van der Molen, K. L., K. J. Klein Koerkamp, F. B. Segerink, N. F. van Hulst, and L. Kuipers, 2005, Phys. Rev. B **72**, 045421.
van der Molen, K. L., F. B. Segerink, N. F. van Hulst, and L. Kuipers, 2004, Appl. Phys. Lett. **85**, 4316.
Moreau, A., G. Granet, F. I. Baida, and D. Van Labeke, 2003, Opt. Express **11**, 1131.
Moreno, E., 2008, private communication .
Moreno, E., A. I. Fernandez-Dominguez, J. I. Cirac, F. J. Garcia-Vidal, and L. Martin-Moreno, 2005, Phys. Rev. Lett. **95**, 170406.
Moreno, E., F. J. Garcia-Vidal, D. Erni, J. I. Cirac, and L. Martin-Moreno, 2004a, Phys. Rev. Lett. **92**, 236801.
Moreno, E., F. J. Garcia-Vidal, and L. Martin-Moreno, 2004b, Phys. Rev. B **69**, 121402(R).
Moreno, E., L. Martin-Moreno, and F. J. Garcia-Vidal, 2004c, Photonics and Nanostructures - Fundamentals and Applications **2**, 97.
Morrison, S. K., and Y. S. Kivshar, 2005, Appl. Phys. Lett. **86**, 081110.
Moussa, R., B. Wang, G. Tuttle, T. Koschny, and C. M. Soukoulis, 2007, Phys. Rev. B **76**, 235417.
Mrejen, M., A. Israel, H. Taha, M. Palchan, and A. Lewis, 2007, Opt. Express **15**, 9129.
Muller, R., V. Malyarchuk, and C. Lienau, 2003, Phys. Rev. B **68**, 205415.
Müller, R., C. Ropers, and C. Lienau, 2004, Opt. Express **12**, 5067.
Munk, B. A., 2000, *Frequency Selective Surfaces: Theory and Design* (Willey Interscience).
Nahata, A., R. A. Linke, T. Ishi, and K. Ohashi, 2003, Opt. Lett. **28**, 423.
Naweed, A., F. Baumann, W. A. Bailey, A. S. Karakashian, and W. D. Goodhue, 2003, J. Opt. Soc. Am. B **20**, 2534.
Neerhoff, F. L., and G. Mur, 1973, Appl. Sci. Res. **28**, 73.
Neviere, M., 1980, *Electromagnetic theory of gratings* (Springer Verlag).
van Nieuwstadt, J. A. H., M. Sandtke, R. H. Harmsen, F. B. Segerink, J. C. Prangsma, S. Enoch, and L. Kuipers, 2006, Phys. Rev. Lett. **97**, 146102.
Nylander, C., B. Liedberg, and T. Lind, 1982, Sensors and Actuators **3**, 79.
Obermuller, C., and K. Karrai, 1995, Appl. Phys. Lett. **67**, 3408.
Ohno, T., J. A. Bain, and T. E. Schlesinger, 2007, J. Appl. Phys. **101**, 083107.
Onishi, T., T. Tanigawa, T. Ueda, and D. Ueda, 2007, IEEE J. Quant. Elect. **43**, 1123.
Orbons, S. M., and A. Roberts, 2006, Opt. Express **14**, 12623.
Orbons, S. M., A. Roberts, D. N. Jamieson, M. I. Haftel, C. Schlockermann, D. Freeman, and B. Luther-Davies, 2007, Appl. Phys. Lett. **90**, 251107.
Palik, E. D., 1985, *Handbook of Optical Constants of Solids* (Academic Press).
Pang, Y., C. Genet, and T. W. Ebbesen, 2007, Opt. Commun. **280**, 10.
Papasimakis, N., V. A. Fedotov, A. S. Schwanecke, N. I. Zheludev, and F. J. G. De Abajo, 2007, Appl. Phys. Lett. **91**, 081503.
Parthasarathy, R., A. Bykhovski, B. Gelmont, T. Globus, N. Swami, and D. Woolard, 2007, Phys. Rev. Lett. **98**, 153906.
Pendry, J. B., and A. MacKinnon, 1992, Phys. Rev. Lett. **69**, 2772.
Pendry, J. B., L. Martin-Moreno, and F. J. Garcia-Vidal, 2004, Science **305**, 847.
Pohl, D. W., W. Denk, and M. Lanz, 1984, Appl. Phys. Lett. **44**, 651.
Popov, E., N. Bonod, M. Neviere, H. Rigneault, P.-F. Lenne, and P. Chaumet, 2005, Appl. Opt. **44**, 2332.
Popov, E., M. Neviere, S. Enoch, and R. Reinisch, 2000, Phys. Rev. B **62**, 16100.
Porto, J. A., F. J. Garcia-Vidal, and J. B. Pendry, 1999, Phys. Rev. Lett. **83**, 2845.
Porto, J. A., L. Martin-Moreno, and F. J. Garcia-Vidal, 2004, Phys. Rev. B **70**, 081402.
Poujet, Y., M. Roussey, J. Salvi, F. I. Baida, D. Van Labeke, A. Perentes, C. Santischi, and P. Hoffmann, 2006, Photonics and Nanostructures-Fundamentals and applications **4**, 47.
Prikulis, J., P. Hanarp, L. Olofsson, D. Sutherland, and M. Kall, 2004, Nano Lett. **4**, 1003.
Przybilla, F., A. Degiron, C. Genet, T. W. Ebbesen, de Leon-Perez, J. Bravo-Abad, F. Garcia-Vidal, and L. Martin-Moreno, 2008, Opt. Express **16**, 9571.
Przybilla, F., A. Degiron, J. Y. Laluet, C. Genet, and T. W. Ebbesen, 2006a, J. Opt. A: Pure Appl. Opt. **8**, 458.
Przybilla, F., C. Genet, and T. W. Ebbesen, 2006b, Appl. Phys. Lett. **89**, 121115.
Qu, D., and D. Grischkowsky, 2004, Phys. Rev. Lett. **93**, 196804.
Rabson, D. A., N. D. Mermin, D. S. Rokshar, and D. C. Wright, 1991, Rev. Mod. Phys. **63**, 699.
Reilly, T. H., S.-H. Chang, J. D. Corbman, G. C. Schatz, and K. L. Rowlen, 2007, J. Phys. Chem. C **111**, 1689.
Reilly, T. H. I., and K. L. Rowlen, 2004, Proc. SPIE **5513**, 250.
Ren, X.-F., G.-P. Guo, P. Zhang, Y.-F. Huang, Z.-W. Wang, and G.-C. Guo, 2007, Appl. Phys. B-Lasers and Optics **89**, 257.
Renk, R. W., and L. Gensel, 1962, Appl. Opt. **1**, 643.
Rhoads, C. M., E. K. Damon, and B. A. Munk, 1982, Appl. Opt. **21**, 2814.
Rignault, H., J. Capoulade, J. Dintinger, J. Wenger, N. Bonod, E. Popov, T. W. Ebbesen, and P.-F. Lenne, 2005, Phys. Rev. Lett. **95**, 117401.
Rindzevicius, T., Y. Alaverdyan, A. Dahlin, F. Hook, D. S. Sutherland, and M. Kall, 2005, Nano Lett. **5**, 2535.

Roberts, A., 1987, J. Opt. Soc. Am. A **4**, 1970.
Rockstuhl, C., F. Lederer, T. Zentgraf, and H. Giessen, 2007, Appl. Phys. Lett. **91**, 151109.
Rodrigo, S. G., F. J. Garcia-Vidal, and L. Martin-Moreno, 2008, Phys. Rev. B **77**, 075401.
Rokitski, R., K. A. Tetz, and Y. Fainman, 2005a, Phys. Rev. Lett. **95**, 177401.
Rokitski, R., K. A. Tetz, and Y. Fainman, 2005b, Nano Lett. **5**, 1963.
Ropers, C., D. J. Park, G. Stibenz, G. Steinmeyer, D. S. Kim, and C. Lienau, 2005, Phys. Rev. Lett. **94**, 113901.
Ropers, C., G. Stibenz, G. Steinmeyer, R. Muller, D. J. Park, K. G. Lee, J. E. Kihm, J. Kim, Q. H. Park, D. S. Kim, and C. Lienau, 2006, Appl. Phys. B-Lasers and Optics **84**, 183.
Salomon, L., F. Grillot, A. V. Zayats, and F. De Fornel, 2001, Phys. Rev. Lett. **86**, 1110.
Salvi, J., M. Roussey, F. I. Baida, M. P. Bernal, A. Mussot, T. Sylvestre, H. Maillotte, D. Van Labeke, A. Perentes, I. Utke, C. Sandu, P. Hoffmann, *et al.*, 2005, Opt. Lett. **30**, 1611.
Sarrazin, M., and J. P. Vigneron, 2003, Phys. Rev. E **68**, 166031.
Sarrazin, M., and J. P. Vigneron, 2004, Opt. Commun. **240**, 89.
Sarrazin, M., J. P. Vigneron, and J. M. Vigoureux, 2003, Phys. Rev. B **67**, 085415.
Schellenberg, F. M., K. Adam, J. Matteo, and L. Hessenlink, 2005, J. Vac. Sci. Technol. B **23**, 3106.
Schroter, U., and D. Heitmann, 1998, Phys. Rev. B **58**, 15419.
Seo, S., H. C. Kim, H. Ko, and M. Cheng, 2007, J. Vac. Sci. Technol. B **25**, 2271.
Sepúlveda, B., Y. Alaverdyan, J. Alegret, M. Käll, and P. Johansson, 2008, Opt. Express **16**, 5609.
Shaner, E. A., J. G. Cederberg, and D. Wasserman, 2007, Appl. Phys. Lett. **91**, 181110.
Shao, D. B., and S. C. Chen, 2005, Appl. Phys. Lett. **86**, 254107.
Shao, D. B., and S. C. Chen, 2008, J. Vac. Sci. Technol. B **26**, 227.
Sharpe, J. C., J. S. Mitchell, L. Lin, N. Sedoglavich, and R. J. Blaikie, 2008, Anal. Chem. **80**, 2244.
Shen, J. T., P. B. Catrysse, and S. Fan, 2005, Phys. Rev. Lett. **94**, 1.
Shi, H., C. Du, and X. Luo, 2007, Appl. Phys. Lett. **91**, 093111.
Shinada, S., J. Hashizume, and F. Koyama, 2003, Appl. Phys. Lett. **83**, 836.
Sick, B., B. Hecht, U. P. Wild, and L. Novotny, 2001, J. Microscopy-Oxford **202**, 365.
Sinton, D., R. Gordon, and A. G. Brolo, 2008, Microfluid Nanofluid **4**, 107.
Skigin, D. C., and R. A. Depine, 2005, Phys. Rev. Lett. **95**, 217402.
Skigin, D. C., and R. A. Depine, 2006, Opt. Commun. **262**, 270.
Smolyaninov, I. I., A. V. Zayats, A. Stanishevsky, and C. C. Davis, 2002, Phys. Rev. B **66**, 205414.
Sondergaard, T., and S. I. Bozhevolnyi, 2004, Phys. Rev. B **69**, 045422.
Sonnichsen, C., A. C. Duch, G. Steininger, M. Koch, G. von Plessen, and J. Feldmann, 2000, Appl. Phys. Lett. **76**, 140.
Srituravanich, W., N. Fang, S. Durant, M. Ambati, S. Sun, and X. Zhang, 2004, J. Vac. Sci. Technol. B **22**, 3475.
Stark, P. R. H., A. E. Halleck, and D. N. Larson, 2005, Methods **37**, 37.
Steele, J. M., C. E. Moran, A. Lee, C. M. Aguirre, and N. J. Halas, 2003, Phys. Rev. B **68**, 2051031.
Strelniker, Y. M., 2007, Phys. Rev. B **76**, 085409.
Suckling, J. R., A. P. Hibbins, M. J. Lockyear, T. W. Preist, J. R. Sambles, and C. R. Lawrence, 2004, Phys. Rev. Lett. **92**, 147401.
Suh, J. Y., E. U. Donev, R. Lopez, L. C. Feldman, and R. F. Haglund, 2006, Appl. Phys. Lett. **88**, 133115.
Sun, M., R.-J. Liu, Z.-Y. Li, B.-Y. Cheng, D.-Z. Zhang, H. F. Yang, and A. Z. Jin, 2006a, Chinese Physics **15**, 1591.
Sun, M., R.-J. Liu, Z.-Y. Li, B.-Y. Cheng, D.-Z. Zhang, H. F. Yang, and A. Z. Jin, 2007, Phys. Lett. A **365**, 510.
Sun, M., J. Tian, S. Z. Han, Z.-Y. Li, B.-Y. Cheng, D.-Z. Zhang, A. Z. Jin, and H. F. Yang, 2006b, J. Appl. Phys. **100**, 024320.
Sun, M., J. Tian, Z.-Y. Li, B.-Y. Cheng, D.-Z. Zhang, A. Z. Jin, and H. F. Yang, 2006c, Chin. Phys. Lett. **23**, 486.
Sun, Z., Y. Jung, and H. K. Kim, 2003, Appl. Phys. Lett. **83**, 3021.
Sutherland, R. L., 1996, *Handbook of Nonlinear Optics* (Marcel Dekker,Inc.).
Takakura, Y., 2001, Phys. Rev. Lett. **86**, 5601.
Tanaka, M., F. Miyamaru, M. Hangyo, T. Tanaka, M. Akazawa, and E. Sano, 2005, Opt. Lett. **30**, 1210.
Tang, D., L. Chen, and W. Ding, 2006, Appl. Phys. Lett. **89**, 131120.
Teeters-Kennedy, S., S. M. Williams, K. R. Rodriguez, K. Cilwa, D. Meleason, A. Sudnitsyn, F. Hrovat, and J. V. Coe, 2007, J. Phys. Chem. C **111**, 124.
Tetz, K. A., L. Pang, and Y. Fainman, 2006, Opt. Lett. **31**, 1528.
Thio, T., H. F. Ghaemi, H. J. Lezec, P. A. Wolff, and T. W. Ebbesen, 1999, J. Opt. Soc. Am. B **16**, 1743.
Thio, T., K. M. Pellerin, R. A. Linke, H. J. Lezec, and T. W. Ebbesen, 2001, Optics Letters **26**, 1972.
Thomas, D. A., and H. P. Hughes, 2004, Solid State Commun. **129**, 519.
Treacy, M. M. J., 1999, Appl. Phys. Lett. **75**, 606.
Treacy, M. M. J., 2002, Phys. Rev. B **66**, 1951051.
Ulrich, R., 1967, Infrared Phys. **7**, 37.
Ulrich, R., 1974, Microwave Res. Inst. Symp. Ser. **23**, 359.
Urzhumov, Y. A., D. Korobkin, B. Neuner, C. Zorman, and G. Shvets, 2007, J. Opt. A: Pure Appl. Opt. **9**, S322.
Veerman, J. A., M. F. Garcia-Parajo, L. Kuipers, and N. F. van Hulst, 1999, J. Microscopy-Oxford **194**, 477.
Wang, B., and G. P. Wang, 2006, Appl. Phys. Lett. **88**(013114).
Wang, C., C. Du, and X. Luo, 2006a, Phys. Rev. B **74**, 245403.
Wang, C., C. Du, Y. Lv, and X. Luo, 2006b, Opt. Express **14**, 5671.
Wannemacher, R., 2001, Opt. Commun. **195**, 107.
Wasserman, D., E. A. Shaner, and J. G. Cederberg, 2007, Appl. Phys. Lett. **90**, 191102.
Webb, K. J., and J. Li, 2006, Phys. Rev. B **73**, 033401.
Wei, X., X. Luo, X. Duong, and C. Du, 2007, Opt. Express **15**, 14177.
Wenger, J., D. Gerard, J. Dintinger, O. Mahboub, N. Bonod, E. Popov, T. W. Ebbesen, and H. Rignault, 2008, Opt. Express **16**, 3008.
Went, H. E., A. P. Hibbins, J. R. Sambles, C. R. Lawrence, and A. P. Crick, 2000, Appl. Phys. Lett. **77**, 2789.
Williams, S. M., and J. V. Coe, 2006, Plasmonics **1**, 87.

Williams, S. M., A. D. Stafford, K. R. Rodriguez, T. M. Rogers, and J. V. Coe, 2003, J. Phys. Chem. B **107**, 11871.
Williams, S. M., A. D. Stafford, T. M. Rogers, S. R. Bishop, and J. V. Coe, 2004, Appl. Phys. Lett. **85**, 1472.
Wurtz, G. A., R. Pollard, and A. V. Zayats, 2006, Phys. Rev. Lett. **97**, 057402.
Xie, Y., A. R. Zakharian, J. V. Moloney, and M. Mansuripur, 2005, Opt. Express **13**, 4485.
Xing, Q., S. Li, Z. Tian, D. Liang, N. Zhang, L. Lang, L. Chai, and Q. Wang, 2006, Appl. Phys. Lett. **89**, 041107.
Xu, T., X. Jiao, G. P. Zhang, and B. S., 2007, Opt. Express **15**, 13894.
Yang, F., and J. R. Sambles, 2002, Phys. Rev. Lett. **89**, 063901.
Ye, Y.-H., Z.-B. Wang, Y.-R. Cao, D. S. Yan, J.-Y. Zhang, X. Q. Lin, and T. J. Cui, 2007a, Appl. Phys. Lett. **91**, 251105.
Ye, Y.-H., Z.-B. Wang, D. S. Yan, and J.-Y. Zhang, 2007b, Opt. Lett. **32**, 3140.
Ye, Y.-H., and J. Y. Zhang, 2005, Opt. Lett. **30**, 1521.
Yin, L., V. K. Vlasko-Vlasov, A. Rydh, J. Pearson, U. Welp, S.-H. Chang, S. K. Gray, D. B. Brown, and C. W. Kimball, 2004, Appl. Phys. Lett. **85**, 467.
Yu, L. B., D. Z. Lin, Y. C. Chen, Y. C. Chang, K. T. Huang, J. W. Liaw, J. T. Yeh, J. M. Liu, C. S. Yeh, and C. K. Lee, 2005, Phys. Rev. B **71**, 041405(R).
Zayats, A. V., L. Salomon, and F. de Fornel, 2003, J. Microscopy **210**, 344.
Zenneck, J., 1907, Ann. Phys. **23**, 846.
Zhou, L., and G. A. Kriegsmann, 2007, J. Acoust. Soc. Am. **121**, 3288.
Zhou, R. L., X. S. Chen, S. W. Wang, W. Lu, Y. Zeng, H. B. Chen, H. J. Li, H. Xia, and L. L. Wang, 2008, Solid State Comm. **145**, 23.